# THE POLARIZATION AND MAGNETIC MOMENT OF THE CASCADE MINUS HYPERON

By REGINA ABBY RAMEIKA

A thesis submitted to

The Graduate School

of

Rutgers, The State University of New Jersey

in partial fulfillment of the requirements

for the degree of

Doctor of Philosophy

Graduate Program in Physics

Written under the direction of

Professor Thomas J. Devlin

and approved by

Joe H. Bifen

Paul A. Shapiro

Douglas H. Potter

Thomas J. Devlin

New Brunswick, New Jersey

December 1981

A781675

FERMILAB
LIBRARY

ABSTRACT OF THE THESIS

The Inclusive Polarization

and Magnetic Moment of the

$\Xi^-$ Hyperon

by

Regina Abby Rameika

Chairman : Thomas J. Devlin

The magnetic moment of the $\Xi^-$ hyperon has been measured to be $-0.716 \pm 0.040$ nuclear magnetons by observing the precession of the $\Xi^-$ polarization vector in a magnetic field. The $\Xi^-$'s were produced by 400 GeV protons at angles of $\pm$ 5 and $\pm$ 7.5 mr, and had momenta between 105 and 290 GeV/c. The charged particles from the $\Xi^- \rightarrow \Lambda \pi^-$ and $\Lambda \rightarrow p \pi^-$ decays were detected in a multiwire proportional chamber spectrometer. Results are based on 192,110 events. The measured $\Xi$ polarization is presented as a function of $\Xi^-$ momentum. The average polarization was $-0.093 \pm 0.007$. The helicity of the decay $\Lambda$'s was also measured, giving the value of $\alpha_\Lambda \alpha_\Xi = -0.303 \pm 0.004 \pm 0.004$.

ACKNOWLEDGEMENTS

I would like to thank my thesis advisor, Tom Devlin, for his advice and enthusiasim throughout the completion of this project.

I also want to thank all the members of the Rutgers-Michigan-Minnesota-Wisconsin collaboration who contributed to this project. I would particularly like to thank Bob Handler for writing the reconstruction program and Tim Cox for his instruction and suggestions in the early days of the analysis. Les Deck and Kam Biu Luk were constant sources of discussion and advice. Thanks also go to Lee Pondrom, Ken Heller and Andy Beretvas for many helpful suggestions.

Finally, I would like to thank my husband, Byron Lundberg, for his unending patience and support, particularly throughout the preparation of this document, and above all my parents for all the support and encouragement they have given me throughout my academic career.

TABLE OF CONTENTS


| | page |
|---|---|
| Abstract | ii |
| Acknowledgements | iii |
| Table of Contents | iv |
| List of Tables | vii |
| List of Figures | ix |
| 1. Introduction | 1 |
| 1.1 Experimental Background | 1 |
| 1.2 Magnetic Moments | 4 |
| 1.3 Charged Particle Precession | 8 |
| 2. The Experiment | 13 |
| 2.1 The Proton Beam | 13 |
| 2.2 The Charged Hyperon Collimator | 15 |
| 2.3 The Precession Magnet | 19 |
| 2.4 Sign Conventions and Coordinate System | 22 |
| 2.5 The Spectrometer | 23 |
| 2.6 The Trigger | 28 |
| 2.7 Data Acquisition | 30 |
| 2.8 Trigger Rates | 31 |
| 3. Event Reconstruction | 33 |
| 3.1 Pattern Recognition | 33 |
| 3.2 Event Identification | 36 |
| 3.3 The Monte Carlo | 52 |
| 3.3.1 Monte Carlo Event Generation | 52 |
| 3.3.2 Monte Carlo Event Reconstruction | 56 |

3.4 Background Studies 60

3.4.1 Monte Carlo Fool Events 62

3.4.2 Collimator Production 64

4. The Polarization Analysis 69

4.1 General Analysis of Asymmetries 69

4.2 Daughter Lambda Analysis 75

4.3 The Asymmetry Parameter 81

4.4 First Iteration Polarization Analysis 85

4.5 Polarization and Bias Fit 86

4.6 Second Iteration Analysis 87

4.7 Monte Carlo Analysis 90

4.8 Systematics in the Polarization Analysis 91

5. Results 95

5.1 The Inclusive Polarization 95

5.2 The Asymmetry Parameter 117

5.3 The Magnetic Moment 124

5.4 Error Propagation and Systematic Error 126

5.5 Magnetic Moment Fit 131

6. Implications 133

6.1 Inclusive Polarization 133

6.2 The $\Xi$ Asymmetry Parameters 137

6.3 Baryon Magnetic Moments 139

6.4 Summary 143

Appendix A : The Reconstruction Program 145

Appendix B : The Hybrid Monte Carlo Program 149

Appendix C : The Polarization Results for Sets 1 & 2 157

References 171

Vita 174

## LIST OF TABLES


| | | page |
|---|---|---|
| 1.1 | SU(3) x SU(2) baryon wave functions | 6 |
| 1.2 | Baryon magnetic moment relations | 6 |
| 1.3 | Theoretical and experimental magnetic moments | 7 |
| 1.4 | Theoretical and experimental values of g/2 | 7 |
| 2.1 | Summary of data tapes | 32 |
| 2.2 | Summary of raw trigger rates | 32 |
| 3.1 | Reconstruction quality codes | 35 |
| 3.2 | MC vs real event reconstruction efficiencies | 59 |
| 4.1 | $\langle\hat{\Lambda}\cdot\hat{n}\rangle$ as a function of momentum | 80 |
| 4.2 | Results of Master $\chi^2$ Fit | 88 |
| 4.3 | Monte Carlo biases | 93 |
| 5.1 | Momentum averaged polariztaions and biases for all data | 97 |
| 5.2 | x and z polarization vs momentum | 98 |
| 5.3 | x and z biases vs momentum | 99 |
| 5.4 | Parity violating y polarization and bias as a function of momentum | 100 |
| 5.5 | $\alpha_\Lambda\alpha_\Xi$ for all data, minimum cuts applied | 118 |
| 5.6 | $\alpha_\Lambda\alpha_\Xi$ for all data, final cuts applied | 118 |
| 5.7 | $\alpha_\Lambda\alpha_\Xi$ as a function of momentum, Sets 1&2 | 119 |
| 5.8 | $\alpha_\Lambda\alpha_\Xi$ as a function of momentum, Sets 3-5 | 120 |
| 5.9 | Precession angles at 6.6 and 5.1 T-m fields | 128 |
| 5.10 | G-factors and magnetic moments for ambiguous solutions | 128 |

5.11 $\chi^2$ fit to individual data sets 132

6.1 Theoretical predictions for baryon moments using refined models 141

C.1 x and z polarizations vs momentum (Sets 1&2) 158

C.2 x and z biases vs momentum (Sets 1 & 2) 159

C.3 y polarization and biases (Sets 1 & 2) 160

## LIST OF FIGURES


| | | page |
|---|---|---|
| 1.1 | Charged Particle Precession | 12 |
| 2.1 | The M2 beam delivery system | 16 |
| 2.2 | The hyperon production target and associated detectors | 16 |
| 2.3 | Plan and elevation views of the charged hyperon collimator | 18 |
| 2.4 | Field integral vs. precession magnet current | 20 |
| 2.5 | Field integral vs. the standard field | 21 |
| 2.6 | Plan view of the spectrometer | 25 |
| 2.7 | Elevation view of the spectrometer | 26 |
| 3.1 | Geometric $\chi^2$ distribution for real events | 37 |
| 3.2 | $p-\pi^-$ invariant mass distribution | 39 |
| 3.3 | Kinematic $\chi^2$ distribution for $p-\pi^-$ constrained to $\Lambda$ mass | 40 |
| 3.4 | $\Lambda-\pi^-$ invariant mass | 41 |
| 3.5 | $\Lambda-k^-$ invariant mass | 42 |
| 3.6 | $\Lambda-\pi^-$ invariant mass using fitted $\Lambda$ momentum | 44 |
| 3.7 | $\Xi^-$ z-vertex distribution for data and MC | 45 |
| 3.8 | $\Lambda$ z-vertex distribution for data and MC | 46 |
| 3.9 | $\Xi^-$ momentum distribution | 47 |
| 3.10 | Pion momentum distribution from $\Xi^- \rightarrow \Lambda\pi^-$ | 48 |
| 3.11 | $\Lambda$ momentum distribution | 49 |
| 3.12 | Proton momentum distribution | 50 |
| 3.13 | Pion momentum distribution from $\Lambda \rightarrow p\pi^-$ | 51 |

3.14 Schematic Diagram of the event selection process 53

3.15 Geometric acceptance of the spectrometer and collimator 55

3.16 Geometric $\chi^2$ distribution for MC events 57

3.17 Logarithmic distribution of $\Lambda-\pi^-$ invariant mass 61

3.18 $R^2$ distribution for all momentum 66

3.19 $R^2$ distribution as a function of momentum 67

4.1 $\theta_y$ distribution at target 72

4.2 x asymmetries for + and - production angles 76

4.3 y asymmetries for + and - production angles 77

4.4 z asymmetries for + and - production angles 78

4.5 Relationship between vectors in $\Xi^-$ and $\Lambda$ rest frames 82

4.6 cos $\theta$ distributions for $\alpha_\Lambda \alpha_{\Xi^-}$ 84

4.7 $\chi^2$ contributions to Master Fit 89

5.1 x polarization for 5 mrad, 6.6 T-m 101

5.2 z polarization for 5 mrad, 6.6 T-m 102

5.3 x bias for 5 mrad, 6.6 T-m 103

5.4 z bias for 5 mrad, 6.6 T-m 104

5.5 y bias for 5 mrad, 6.6 T-m 105

5.6 x polarization for 5 mrad, 5.1 T-m 106

5.7 z polarization for 5 mrad, 5.1 T-m 107

5.8 x bias for 5 mrad, 5.1 T-m 108

5.9 z bias for 5 mrad, 5.1 T-m 109

5.10 y bias for 5 mrad, 5.1 T-m 110

5.11 x polarization for 7.5 mrad, 5.1 T-m 111

5.12 z polarization for 7.5 mrad, 5.1 T-m 112

5.13 x bias for 7.5 mrad, 5.1 T-m 113

5.14 z bias for 7.5 mrad, 5.1 T-m 114

5.15 y bias for 7.5 mrad, 5.1 T-m 115

5.16 Polarization vs transverse momentum 116

5.17 $\alpha_\Lambda \alpha_\Xi$ vs momentum (5 mrad, 6.6 T-m field) 121

5.18 $\alpha_\Lambda \alpha_\Xi$ vs momentum (5 mrad, 5.1 T-m field) 122

5.19 $\alpha_\Lambda \alpha_\Xi$ vs momentum (7.5 mrad, 5.1 T-m field) 123

5.20 Four lowest order precession configurations 125

5.21 Precession angle vs. field integral for ambiguous soluttions 127

6.1 Inclusive polarization for $\Sigma^+$, $\Lambda$, $\Xi^0$, and $\Xi^-$ at 5 mrad production angle 134

6.2 Inclusive polarization for $\Sigma^-$, $\Lambda$, $\Xi^0$, and $\Xi^-$ at 7.5 mrad production angle 135

B.1 Distribution of $\chi^2$s for comparison of real and HMC distributions 153

C.1-C.10 Polarization and Biases for Sets 1 & 2. 161

# CHAPTER 1

# Introduction

## 1.1 Experimental Background

During the period November 1979 through January 1980 a group of physicists from Rutgers University, the University of Wisconsin, the University of Michigan and the University of Minnesota performed Experiment 620 at Fermilab. The purpose of this experiment was to look for inclusive polarization in the charged hyperons - $\Sigma^+$, $\Sigma^-$, $\Xi^-$, and $\Omega^-$, and if they were polarized, to measure their magnetic moments.

This thesis reports the results of an analysis of a sample of over 200,000 $\Xi^-$ hyperons observed in E620. The experimental method used was to produce polarized $\Xi^-$'s and pass them through a magnetic field which precessed the polarization vector through an angle proportional to the quantity (g/2 - 1), i.e. the anomalous part of the magnetic moment.

The historical motivation for doing this was a series of Fermilab experiments beginning with E8, a neutral hyperon survey experiment at 300 GeV, in which it was discovered that, in inclusive $\Lambda$ production from nuclear targets, the $\Lambda$'s were polarized on the order of 8%.[1] A subsequent experiment made use of this polarization to do a precise measurement of the $\Lambda$ magnetic moment.[2]

It has also been established that inclusive polarization occurs at 30 and 400 GeV and in p-p interactions at 30, 400, and 1500 GeV, i.e. it is not an artifact of nuclear structure.[3-5] A number of experiments have measured the polarization as functions of incident proton energy, kinematic variables, and target material. Phenomenological models have attempted to account for this polarization, and some conclude that all hyperons should be polarized.[6-8] Though prior to its discovery, the polarization of particles inclusively produced at high energy was expected to be zero,

phenomenologists now regard it as a general feature of hyperon production. This is supported by the neutral hyperon experiment which found that $\Xi^0$'s are polarized with a dependence on kinematical variables the same as $\Lambda$'s.[9] In the same experiment the inclusive polarization was also used to measure precisely the $\Xi^0$ magnetic moment.[10]

Since isotopic spin invariance is well satisfied by strong interactions, it was natural to expect the $\Xi^-$ to be polarized in the same manner as the $\Xi^0$. The results of the experiment reported here show that such an effect has indeed been observed and measured. The inclusive polarization has also been used to determine the magnetic moment.

Prior to this work the experimental value of the $\Xi^-$ magnetic moment was $-1.85\pm0.75$ (n.m.).[11] This number was the weighted average of two experiments, both of which measured the precession of polarized $\Xi$'s produced in the exclusive reaction $K^-p \rightarrow \Xi^- K^+$. In the first experiment the $\Xi^-$ polarization was very low giving an inconclusive result, $-0.1\pm2.1$.[12] In the second experiment the polarization was larger and the number of events higher. The result was $-2.1\pm0.8$.[13]

## 1.2 Magnetic Moments

For point-like, Dirac, particles the intrinsic magnetic moment, $\vec{\mu}$, is related to the spin, $\vec{S}$, by the relation

$$\vec{\mu}\,(\text{Dirac}) = (q/mc)\,\vec{S}$$

where c is the velocity of light and q and m are the particle's charge and mass. For $|\vec{S}| = 1/2\,\hbar$ this gives

$$|\vec{\mu}| = \hbar/2c\ (q/m)$$

This depends only on physical constants and the particle's charge to mass ratio. For real particles, i.e. baryons and leptons, the magnetic moment can be expressed analogously to Dirac moments by the introduction of a "g-factor" which is a measure of the deviation of the particle's actual moment from its Dirac moment.

$$\vec{\mu} = (g/2)(q/mc)\vec{S} \qquad (1.1)$$

A simple quark model, in which the baryons are composed of the three spin 1/2 particles - the up(u), down(d) and strange(s) quarks, does a surprisingly good job of predicting the baryon moments. It is assumed that a baryon moment is just the vector sum of the quark moments, which are defined as

$$\vec{\mu}_i = (q_i/m_i c)\ \vec{S}_i$$

$m_i$ is the mass of the quark, $q_i$ its charge and $\vec{S}_i$ the vector spin of the quark. The baryon moments can be calculated from

$$\mu_B = \langle a | \sum_i \mu_i | a \rangle$$

where $\langle a|$ is the particle's wave function. Simple quark model wave functions (SU(3)xSU(2)) are listed in Table 1.1. These wave functions are nonrelativistic and assume the orbital angular momentum of the quarks is zero. These lead to the relations for the baryon moments listed in Table 1.2. In an exact SU(3) symmetry all the quarks have the same mass, leading to the magnetic moment predictions listed in Table 1.3. The exact symmetry can be broken in a number of ways. One of the simplest is to use the hyperfine mass splitting formula and the measured hadron masses, to measure the mass ratio of the up and strange quark. Assuming $m_u = m_d$ and $m_u/m_s = 0.622$ the moments of the baryons in the 1/2(+) octet can be predicted and compared with experiment.[14,15] These predictions are also listed in Table 1.3. Table 1.4 lists the predictions and experimental values of g/2. Deviations from g/2 = 1 for charged and g/2 = 0 for neutral particles, indicates the existance of internal structure in the baryon.

When it is considered that no relativistic effects, configuration mixing or isospin violating effects have been taken into account, the agreement between theory and experiment is certainly acceptable. It has been suggested that this agreement can be attributed to these effects being absorbed in the definition of the quark mass. Their contribution to the magnetic moments, then, are not

| Baryon | SU(3) x SU(2) Wave Functions |
|---|---|
| p | $\sqrt{2/3}\, u\uparrow u\uparrow d\downarrow - \sqrt{1/3}\, (u\uparrow u\downarrow + u\downarrow u\uparrow) d\uparrow/\sqrt{2}$ |
| n | $\sqrt{2/3}\, d\uparrow d\uparrow u\downarrow - \sqrt{1/3}\, (d\uparrow d\downarrow + d\downarrow d\uparrow) u\uparrow/\sqrt{2}$ |
| $\Lambda$ | $(u\uparrow d\downarrow - u\downarrow d\downarrow) s\uparrow/\sqrt{2}$ |
| $\Sigma^+$ | $\sqrt{2/3}\, u\uparrow u\uparrow s\downarrow - \sqrt{1/3}\, (u\uparrow u\downarrow + u\downarrow u\uparrow) s\uparrow/\sqrt{2}$ |
| $\Sigma^0$ | $\sqrt{2/3}\, u\uparrow d\uparrow s\downarrow - \sqrt{1/3}\, (u\uparrow d\downarrow + u\downarrow d\uparrow) s\uparrow/\sqrt{2}$ |
| $\Sigma^-$ | $\sqrt{2/3}\, d\uparrow d\uparrow s\downarrow - \sqrt{1/3}\, (d\uparrow d\downarrow + d\downarrow d\uparrow) s\uparrow/\sqrt{2}$ |
| $\Xi^0$ | $\sqrt{2/3}\, s\uparrow s\uparrow u\downarrow - \sqrt{1/3}\, (s\uparrow s\downarrow + s\downarrow s\uparrow) u\uparrow/\sqrt{2}$ |
| $\Xi^-$ | $\sqrt{2/3}\, s\uparrow s\uparrow d\downarrow - \sqrt{1/3}\, (s\uparrow s\downarrow + s\downarrow s\uparrow) d\uparrow/\sqrt{2}$ |

Table 1.1 Baryon Wave Functions for 1/2(+) octet (permutations omitted)

$$\mu p = 4/3\ \mu u - 1/3\ \mu d$$

$$\mu n = 4/3\ \mu d - 1/3\ \mu u$$

$$\mu \Lambda = \mu s$$

$$\mu \Sigma^+ = 4/3\ \mu u - 1/3\ \mu s$$

$$\mu \Sigma^0 = 2/3\ (\mu u + \mu d) - 1/3\ \mu s$$

$$\mu \Sigma^- = 4/3\ \mu d - 1/3\ \mu s$$

$$\mu \Xi^0 = 4/3\ \mu s - 1/3\ \mu u$$

$$\mu \Xi^- = 4/3\ \mu s - 1/3\ \mu d$$

Table 1.2 Baryon Magnetic Moment Relations using simple quark wave functions

| Baryon | SU(3) x SU(2) exact | broken | Experimental |
|---|---|---|---|
| p | +2.79 | +2.79 | +2.793 |
| n | -1.86 | -1.91 | -1.913 |
| $\Lambda$ | -0.93 | -0.61 | -0.6138±0.0047 |
| $\Sigma^0$ | +0.93 | +0.79 | ---------- |
| $\Sigma^+$ | +2.79 | +2.74 | +2.33±0.14 |
| $\Sigma^-$ | -0.93 | -1.21 | -0.89±0.15 a) |
| $\Xi^0$ | -1.86 | -1.46 | -1.253±0.014 b) |
| $\Xi^-$ | -0.93 | -0.52 | -0.716±0.040 c) |

Table 1.3 Theoretical and Experimental Baryon Magnetic Moments (in nuclear magnetons) Data are from Ref. 11, except a), Ref. 16, b), Ref. 10, and c), this experiment

| Baryon | SU(3) x SU(2) exact | broken | Experimental |
|---|---|---|---|
| p | 2.79 | 2.79 | 2.793 |
| n | 1.86 | 1.91 | 1.913 |
| $\Lambda$ | 1.11 | 0.73 | 0.7298±0.0056 |
| $\Sigma^0$ | 1.12 | 1.00 | ---------- |
| $\Sigma^+$ | 3.54 | 3.47 | 2.95±0.18 |
| $\Sigma^-$ | 1.19 | 1.54 | 1.14±0.19 |
| $\Xi^0$ | 2.61 | 2.05 | 1.756±0.020 |
| $\Xi^-$ | 1.31 | 0.73 | 1.008±0.055 |

Table 1.4 Theoretical and Experimental values for g/2 using the data presented in Table 1.3

explicitly seen since the mass parameter, $m_i$, is determined from fitting the data rather than from first principles.[17]

However, these effects most surely exist. Since the present status of experimental magnetic moments is considerably better than when the first theoretical predictions were made, it is not unreasonable to attempt to incorporate these effects into the theories, some of which are discussed in Section 6.2.

## 1.3 Spin Precession in a Magnetic Field

In classical physics, a particle with charge q, mass m and orbital angular momentum $\vec{L}$, placed in an external magnetic field $\vec{B}$, experiences a torque which changes its angular momentum ( $\vec{\tau} = d\vec{L}/dt$) according to the equation of motion

$$d\vec{L}/dt = (q/2mc)\ \vec{L} \times \vec{B}$$

The quantity $(q/2mc)\vec{L}$ is defined to be the orbital magnetic moment $\vec{\mu}_L$ .

In quantum mechanics, intrinsic angular momentum, or spin, also interacts with an external field such that

$$d\vec{S}/dt = \vec{\mu} \times \vec{B} \qquad (1.2)$$

where $\vec{\mu}$ is the particle's intrinsic magnetic moment.

Using Eq. 1.1, Eq. 1.2 can be written

$$d\vec{S}/dt = -(g/2)(q/mc)\ \vec{B} \times \vec{S}$$

This says that the spin will precess with a frequency

$$\vec{\omega}_L = -(g/2)(q/mc)\ \vec{B}$$

This is called the Larmor precession frequency. It is important to note that this is a precession measured in the rest system of the particle, and B is the magnetic induction measured in that frame.

In order to measure the direction of the spin, a Lorentz boost must be made from the laboratory into the rest system. Because the particle is accelerating (due to the Lorentz force) the successive transformations into the rest frame are not collinear. It can be shown that the product of non-collinear Lorentz boosts is equivalent to a Lorentz boost plus a rotation. This manifests itself in a rotation of the rest system coordinates relative to the laboratory axes.

Thus the time rate of change of the spin, measured with respect to a set of axes fixed in the lab, will be related to the rate of change of the spin in the rest system (r.s.) by

$$d\vec{S}/dt(\text{lab}) = d\vec{S}/dt(\text{r.s.}) + \vec{\omega} \times \vec{S}$$

Because the acceleration is perpendicular to the particle velocity, $\vec{\omega}$ is the Thomas precession [18,19]

$$\vec{\omega}_T = \{\gamma/(\gamma + 1)\}(1/c^2)\ \vec{a} \times \vec{v}$$

where a and v are the particle acceleration and velocity. $\beta = |\vec{v}|/c$ and $\gamma = (1 - \beta^2)^{1/2}$. For $\vec{a} = q/\gamma mc\ \vec{v} \times \vec{B}$, and $\vec{v} \perp \vec{B}$,

$$\vec{\omega}_T = (\gamma + 1)/\gamma\ (q/mc)\ \vec{B}$$

Relating the proper time and magnetic induction in the rest frame, to the time and induction measured in the lab gives

$$d\vec{S}/dt(\text{lab}) = -(g/2)(q/mc)\ \vec{B} \times \vec{S} + \{\gamma + (1/\gamma)\}(q/mc)\ \vec{B} \times \vec{S}$$

For $\vec{B} \perp \vec{S}$, and $d|\vec{S}|/dt = (1/S)\ d\phi/dt$,

$$d\phi/dt(\text{lab}) = -q/mc\ (g/2 - 1 - 1/\gamma)\ B$$

where $\phi$ is the angle through which the spin rotates. Substituting $dt = dl/\beta c$, and integrating over the path length,

$$\phi\ (\text{lab}) = -q/\beta mc^2\ (g/2 - 1 - 1/\gamma) \int B \cdot dl$$

For the momentum range of the $\Xi$'s in this experiment (100-300 GeV) the contribution of the $1/\gamma$ term ranges from 1/2 to 1 degree. However, the momentum dependence of the precession angle can be eliminated by measuring the precession of the spin with respect to the momentum vector rather than the fixed laboratory axes. The momentum vector precesses through the angle

$$\phi\ (\text{momentum}) = -q/\beta\gamma mc^2 \int B \cdot dl$$

The net precession angle, measured with respect to the momentum, is then given by

$$\phi\ (\text{net}) = -q/\beta\ mc^2\ (g/2 - 1) \int B \cdot dl$$

For the $\Xi^-$, $q=-e$, $mc^2=1.321$ GeV/$c^2$, and $\beta = 1$. This gives

$$\phi\ (\text{measured}) = -13.01\ (g/2 - 1) \int B \cdot dl \qquad (1.3)$$

where $\phi$ is measured in degrees and $\int B\,dl$ in Tesla-meters.[20] A minus sign has been inserted to be consistent with the precession sense in the coordinate system defined in Section 2.4. If the spin rotates in the same sense as the momentum, but at a faster rate, the quantity $(g/2 - 1)$ will be greater than zero. Likewise, if the spin precesses less rapidly than the momentum, $(g/2 - 1)$ will be negative. Fig. 1.1 shows a qualitative description of the spin precession.

The magnetic moment is determined from the precession angle using Eq. 1.1 and the relation

$$\mu \text{ (nuclear magnetons)} = (q/e)(m_p/m_\Xi)(g/2)$$

where $m_p$ is the proton mass. For the $\Xi^-$

$$\mu \text{ (n.m.)} = -0.710\ (g/2) \qquad (1.4)$$

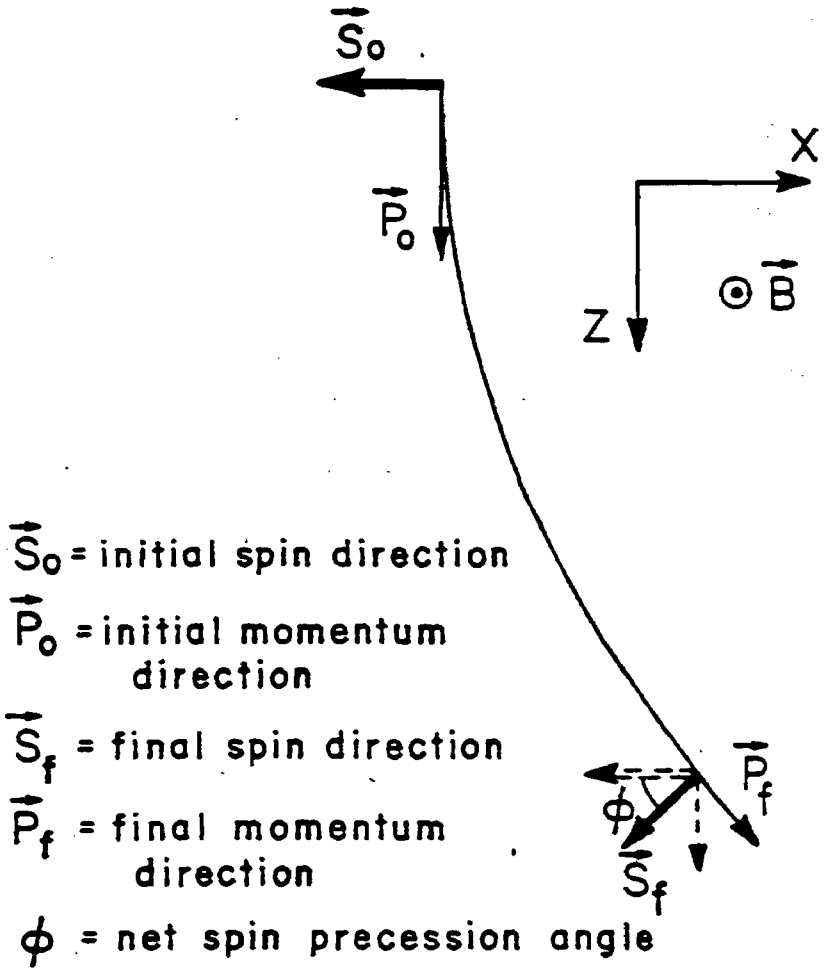


Figure 1.1 Charged particle precession in a magnetic field

# CHAPTER 2

## The Experiment

The experiment was performed in the Fermilab, M2 diffracted proton beam. The basic components of the apparatus were a beryllium target, a momentum selecting collimator, a spin precession field and a multiwire proportional chamber spectrometer.

### 2.1 The Proton Beam

The Fermilab proton synchrotron was operated at an energy of 400 GeV with proton intensities of approximately $2 \times 10^{13}$ protons per machine cycle. Protons were delivered to the experimental areas in one second "beam spills" with cycle

times ranging from 8 to 15 seconds. Protons extracted from the synchrotron were separated for delivery to three major experimental areas by means of electrostatic septa. Protons to the Meson area were incident on the Meson Central Target where three secondary beams were produced. Incident proton angles of 1.7 to 1 mrad produced a 400 GeV diffracted beam in the M2 line with intensities ranging from $2.5 \times 10^{7}$ to $2.5 \times 10^{8}$ protons per machine spill.

The protons were transported down the M2 line in two stages. Each stage consisted of a dipole and a set of quadrupoles. The first stage brought the beam to an intermediate horizontal and vertical focus 200 m from the Meson target. The second stage brought the beam to a focus at the hyperon production target, 450 m from the Meson target. This second focus was also a momentum focus. The beam intensity was controlled by sets of horizontal and vertical collimators at 107 m and 204 m respectively, as well as varying the incident proton angle. The incident direction of the proton beam on the hyperon target was controlled by a set of dipole magnets which deflected the beam in the vertical plane. The first was located at 335 m and produced a vertical displacement as large as 3.7 cm at 446 m. A second dipole restored the beam to the median plane at the production target. In this manner, vertical production angles as large as 10 mrad, both positive and negative could

be achieved. This ability to have both positive and negative production angles was a very important feature of this experiment. The M2 beam delivery system is illustrated in Fig. 2.1.

A SWIC (segmented wire ion chamber) was positioned just upstream of the second focus to monitor the the beam position and spot size. An argon-filled ion chamber one-half-meter upstream of the hyperon production target monitored the proton beam intensity. A set of three scintillation counters just upstream of the ion chamber monitored the quality of the proton focus and were used to calibrate the ion chamber. These were removed during the data taking. Their positions are illustrated in Fig. 2.2.

The hyperon production target was a 15-cm-long (1/2 interaction length), 0.635 cm diameter beryllium cylinder.

## 2.2 The Charged Hyperon Collimator

The production target was followed by a 5.3-m-long magnetic channel. The field was vertical, approximately uniform along the length of the channel, and could be operated at values up to 2.5 Tesla. The purpose of the

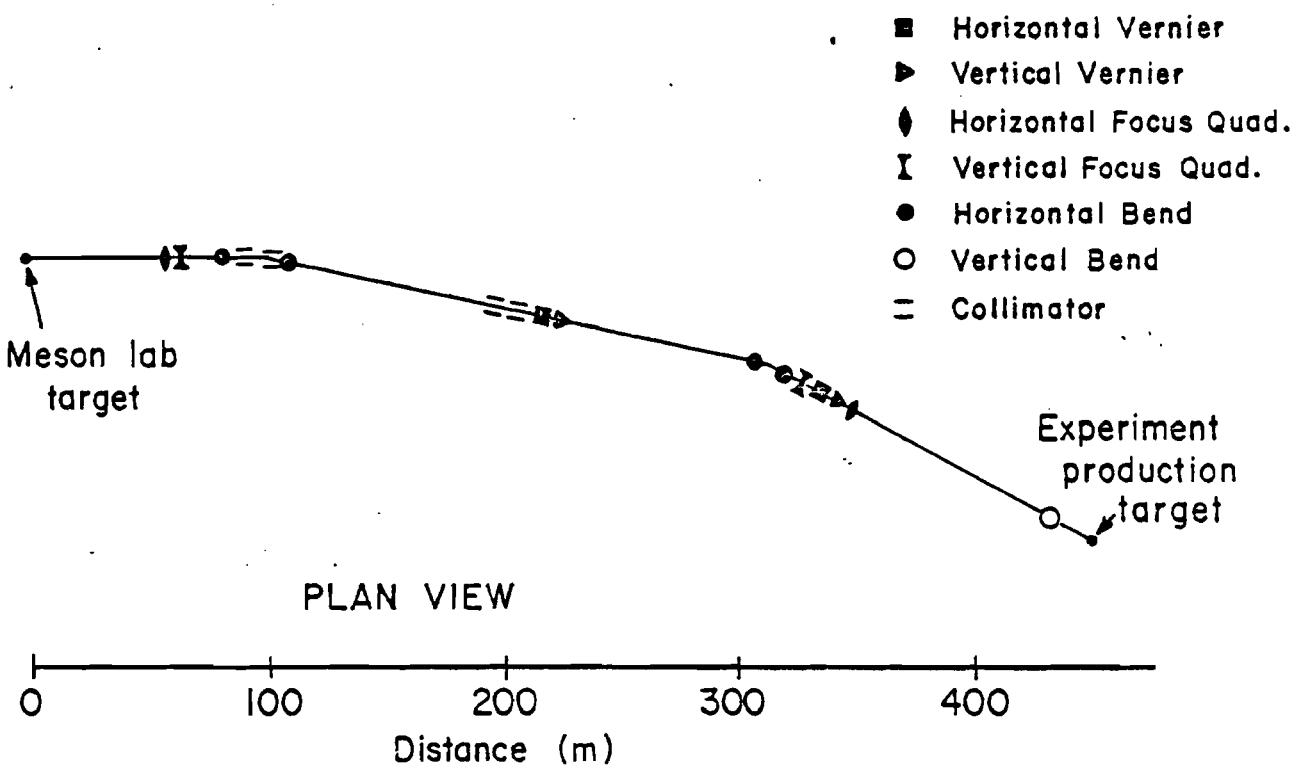


Figure 2.1 The M2 beam delivery system (not to scale).

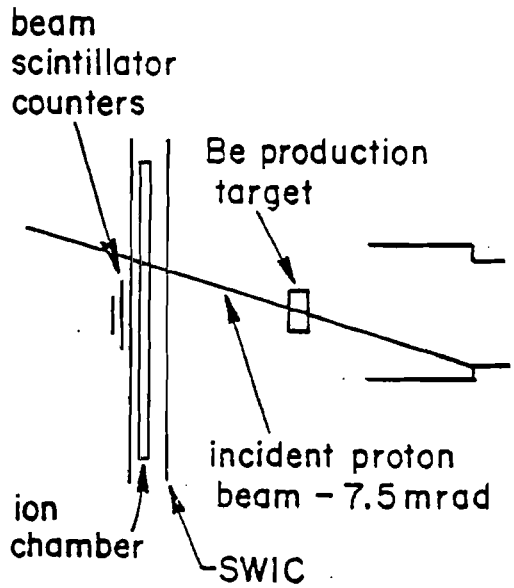


Figure 2.2 The hyperon production target and associated detectors. The horizontal scale has been greatly compressed for this drawing.

magnetic field was twofold. First it served as the precession field for the magnetic moment measurement. It also served to bend charged particles from the production target through a momentum-selecting collimator. The collimator consisted of nine blocks with apertures ranging from one-half to one inch in diameter. The fifth and ninth blocks had tungsten inserts with 4 mm and 10 mm apertures respectively. Thus the fifth block served as the defining aperture giving a solid angle acceptance of 1.4 microsteradians. Details of the collimator are illustrated in Fig. 2.3.

The radius of curvature of the collimator corresponded to a 10 mrad bend angle. When the magnet was operated at a nominal field integral of 6.6 Tesla-meters, which corresponds to giving the particle 2.0 GeV/c transverse momentum, the peak in the observed momentum spectrum transported through the channel was 180 GeV/c. This is lower than the expected 200 GeV/c central momentum of the channel because the production spectrum is a steeply falling function of momentum. The actual momentum acceptance of the channel ranged from 120 to 340 GeV/c, for a 6.6 Tesla-meter field. For a 5.1 T-m nominal field the mean momentum was approximately 20 GeV lower. Typically $\theta_x$ $(=p_x/p_z)$ at the target ranged from +5 mrad to -5 mrad and $\theta_y$ $(=p_y/p_z)$ from -2 to +2 mrad.

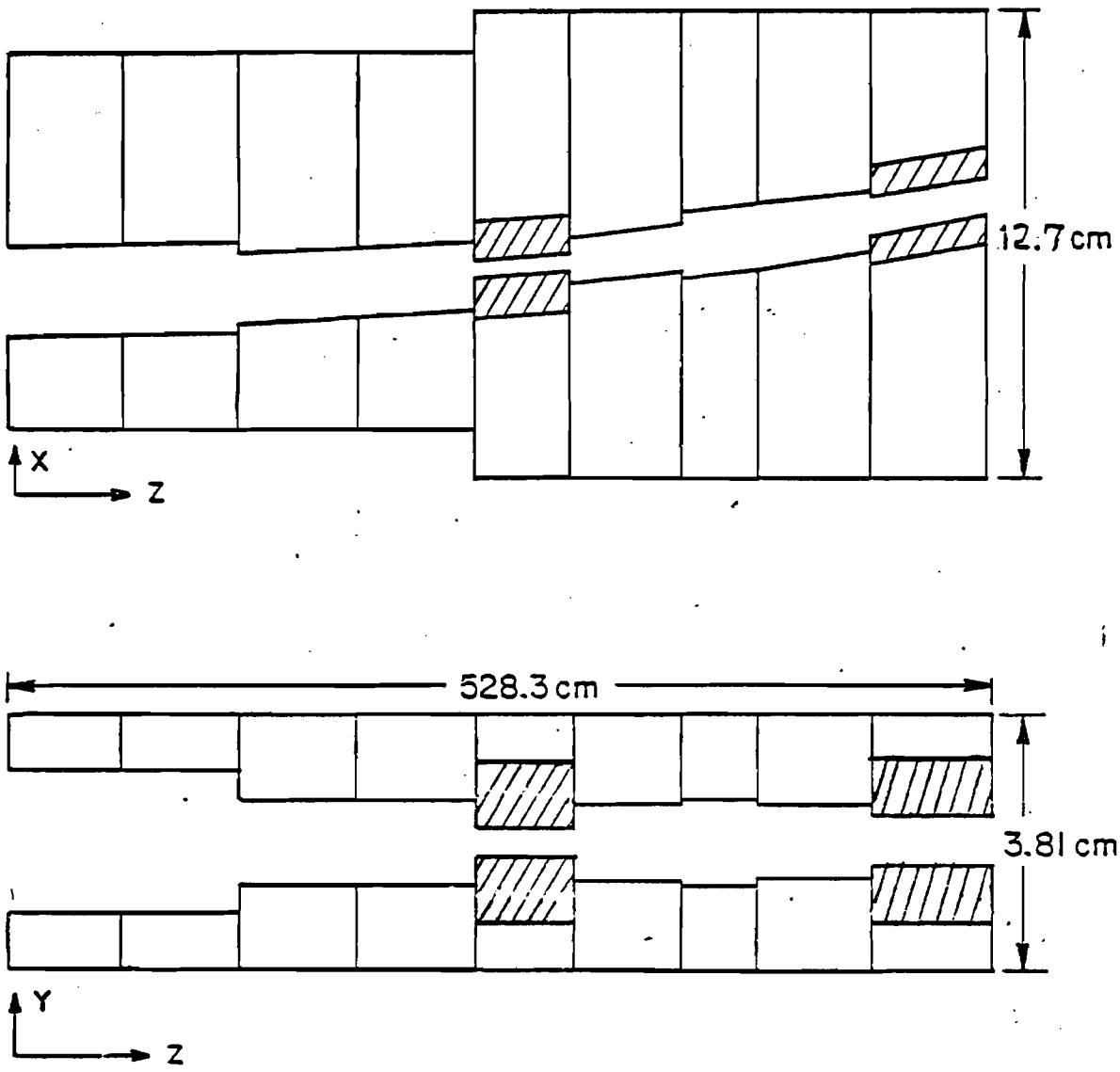


Figure 2.3 Plan and elevation views of the charged hyperon collimator. Note the difference in the longitudinal and transverse scales.

## 2.3 The Precession Magnet

Since the field integral in the precession magnet was directly involved in determining the magnetic moment, it was necessary that it be known accurately. Detailed measurements of the field in this magnet were made for the measurement of the $\Lambda$ magnetic moment.[21] The overall uncertainty in these measurements was less than 0.1%, and makes no significant contribution to the uncertainty in the magnetic moment. To a first approximation the field integral was determined from the current in the magnet and the excitation curve of Fig. 2.4. Secondly, a proton resonance probe was placed in a fixed position in the eighth collimator block. Observation of the proton resonance gave a standard field measurement from which the field integral was determined using Fig. 2.5. Thus for each data run the field integral was reproduced. The standard field was recorded for each data run, and run-to-run fluctuations were found to be less than 0.1%.

In the determination of the magnetic moment a 1.5%(+0.1%) correction was made to the field integral determined from the magnetic calibration data, due to a 40 cm difference in the target position in this experiment and the $\Lambda$ experiment. Thus the field length in this experiment was decreased. It was also noted that in the charged collimator

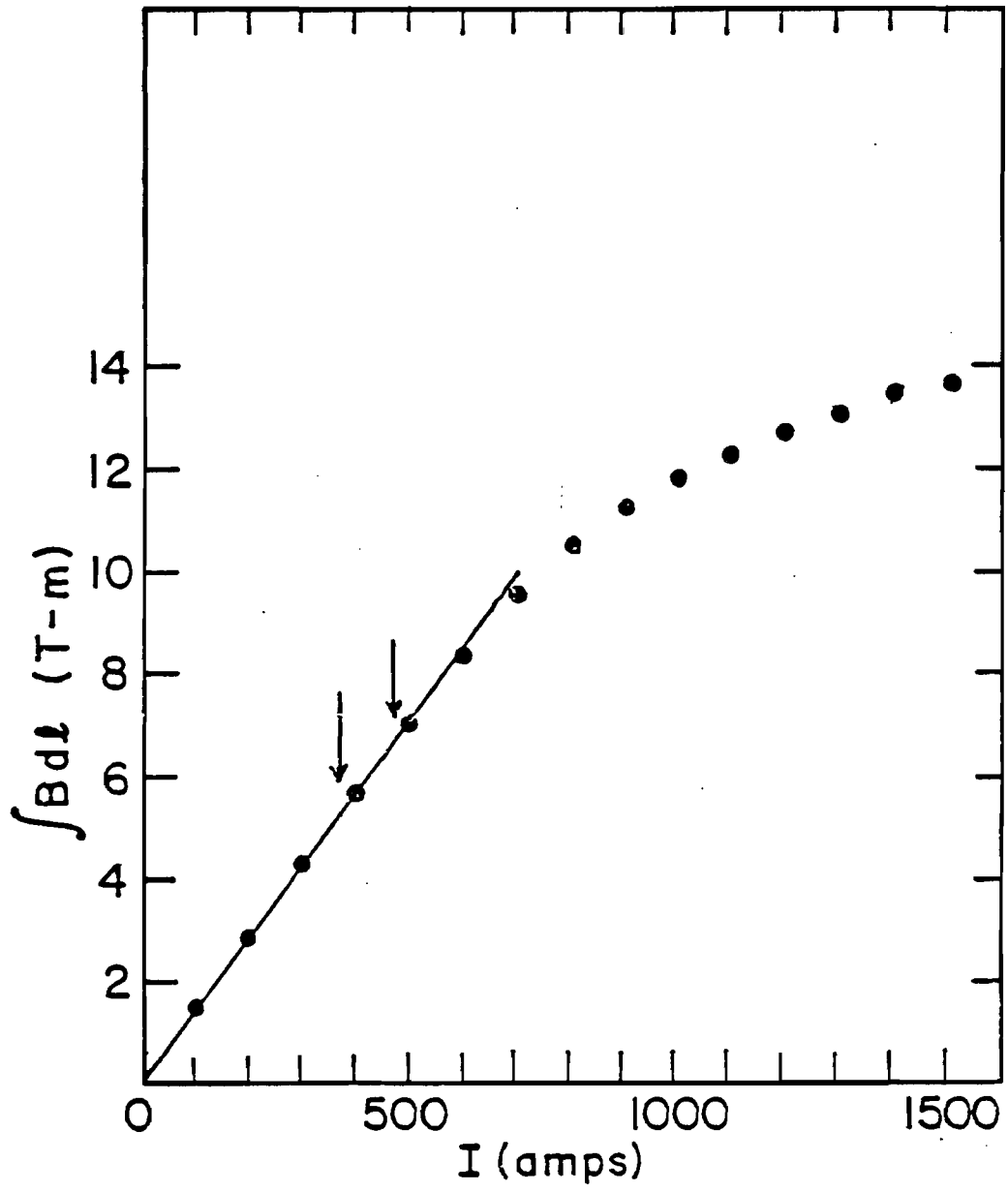


Figure 2.4 Field integral vs. precession magnet current. The arrows indicate the field integrals at which data were taken.

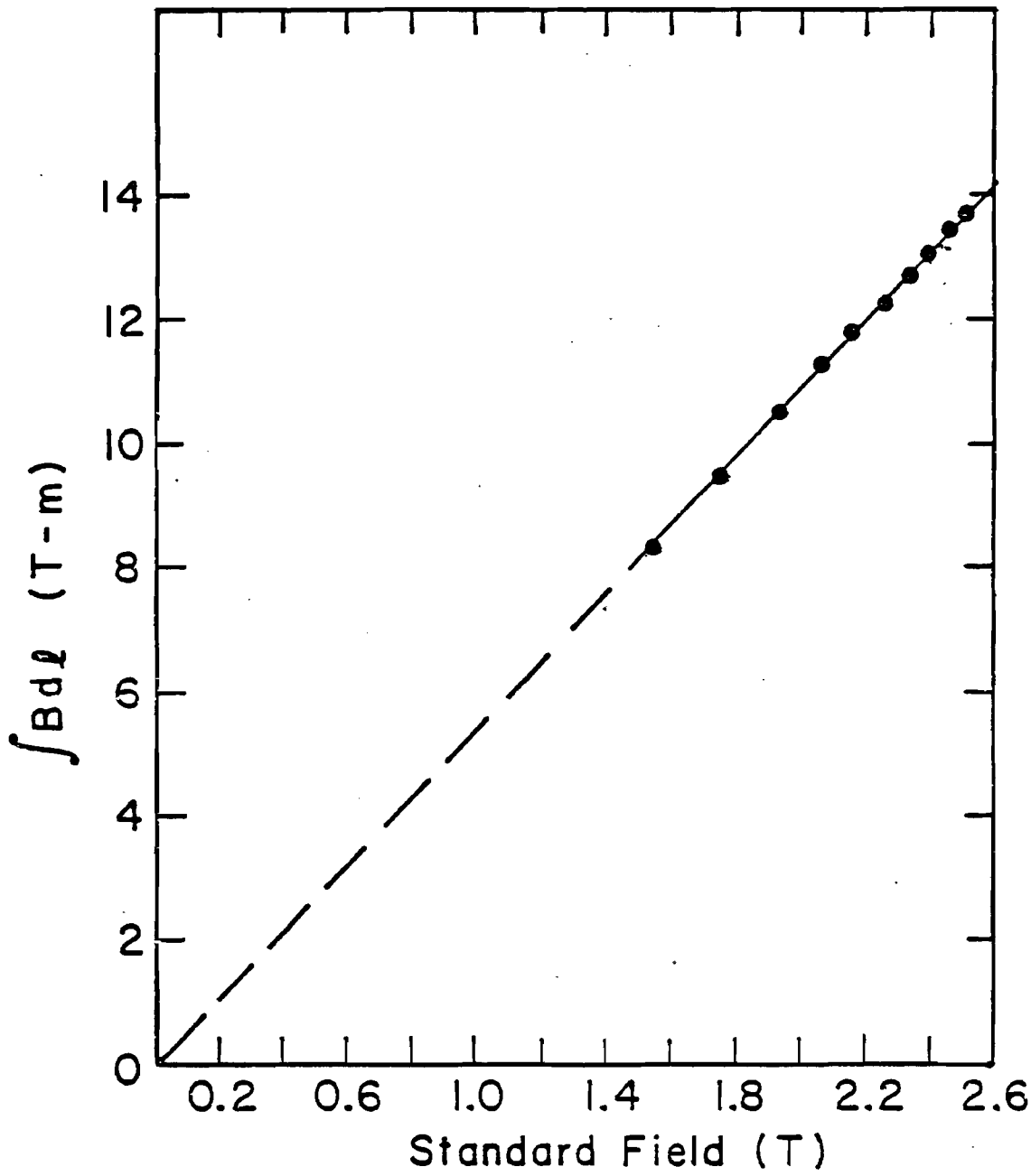


Figure 2.5 The field integral vs. the standard field.

the charged particles traveled off the central axis of the field. This affected the field integral determination by less than 0.2%. Thus, using the field calibrations described in Reference 21, correcting for the field length, and assuming a 0.2% uncertainty, the actual field integrals at which the magnet was operated were 6.60±0.01 T-m and 5.13±0.01 T-m.

## 2.4 Sign Conventions and Coordinate Systems

The spectrometer coordinate system was determined by the 400 GeV proton beam transmitted through the magnetic channel with the Be target out, the field tuned to a transverse bending power of 4.0 GeV/c, and the spectrometer analyzing magnet off. The centroid of this beam defined an axis through the wire chambers which was rotated 10 mrad counterclockwise from the original direction of the M2 proton beam, i.e. along the direction of the central channel momentum. This defined the +z axis of the coordinate system. The MWPC's were aligned perpendicular to this axis thus defining the x and y directions. Positive y was in the upward vertical direction. Positive x was then chosen to be consistent with a right-hand coordinate system. The origin of the spectrometer coordinate system was at the exit aperture of the collimator.

The coordinate system at the target was defined by the spectrometer coordinate system rotated clockwise by 10 mrad about the y axis, translated in x by -2.7 cm, and in z by -5.3 meters.

The direction of the field in the precession magnet was determined by the direction in which charged particles were bent. Negative particles traveling in the +z direction were deflected toward +x, hence the direction of the field was in the +y direction.

The sign of the production angle at the target was defined as positive when the cross product $\vec{p}_{in} \times \vec{p}_{out}$ pointed along +x, where $\vec{p}_{in}$ was the direction of the proton beam incident on the target, and $\vec{p}_{out}$ was the direction of the charged particles accepted into the collimator.

## 2.5 The Spectrometer

The detection apparatus was designed to be sensitive to the decay sequence $\Xi^- \to \Lambda\pi^-$, $\Lambda \to p\pi^-$. It consisted of scintillation counters S1,S2 and S3, eight multiwire proportional chambers (MWPC's) C1-C8, an 8.5-m-long, 40 cm diameter, evacuated decay volume and a superconducting

analyzing magnet (AVIS) with a maximum transverse bending power of 1 GeV/c. The spectrometer is shown in Figs. 2.6-2.7.

S1 was a 10-cm-diameter counter at the exit of the magnetic channel. S2 was a 10-cm x 30-cm halo counter with a 5-cm x 3.8-cm aperture. Chambers 1 and 2 were located between the two counters. This part of the spectrometer was designed to detect the charged track from the $\Xi^-$ or the $\pi^-$ from its decay. The evacuated decay region was located in the most probable region for the $\Lambda$ to decay. There was, however, no trigger requirement that it decay in this region. The decay volume was 8.5-m-long and 36-cm in diameter. It was followed by chambers 3, 4 and 5.

Downstream of these chambers was the 2.5-m-long analyzing magnet. This magnet was operated at current which gave a transverse bending power of 0.951 GeV/c. Positive particles were bent to the -x direction. The analyzing magnet served two purposes. First, the particle's momentum could be determined by reconstructing the tracks upstream and downstream of the magnet's bend center, thus determining a bend angle. The momentum was determined from the relationship $p = p_t/\theta$, where $p_t$ is the transverse bending power of the magnet. Secondly, separating positive and negative tracks downstream of this magnet creates a "v"

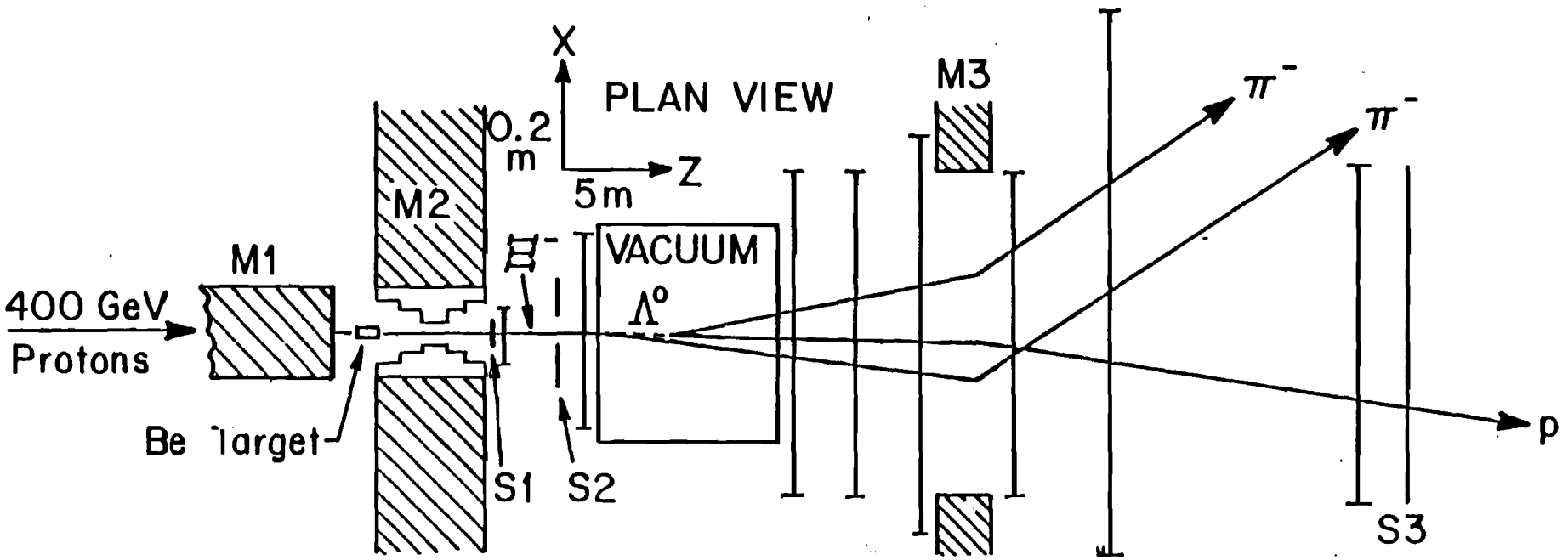


Figure 2.6 Plan view of the spectrometer with a typical event topology. Note that there is a 10 mrad rotation of the spectrometer which is not shown. The MWPC's are labeled in Figure 2.7.

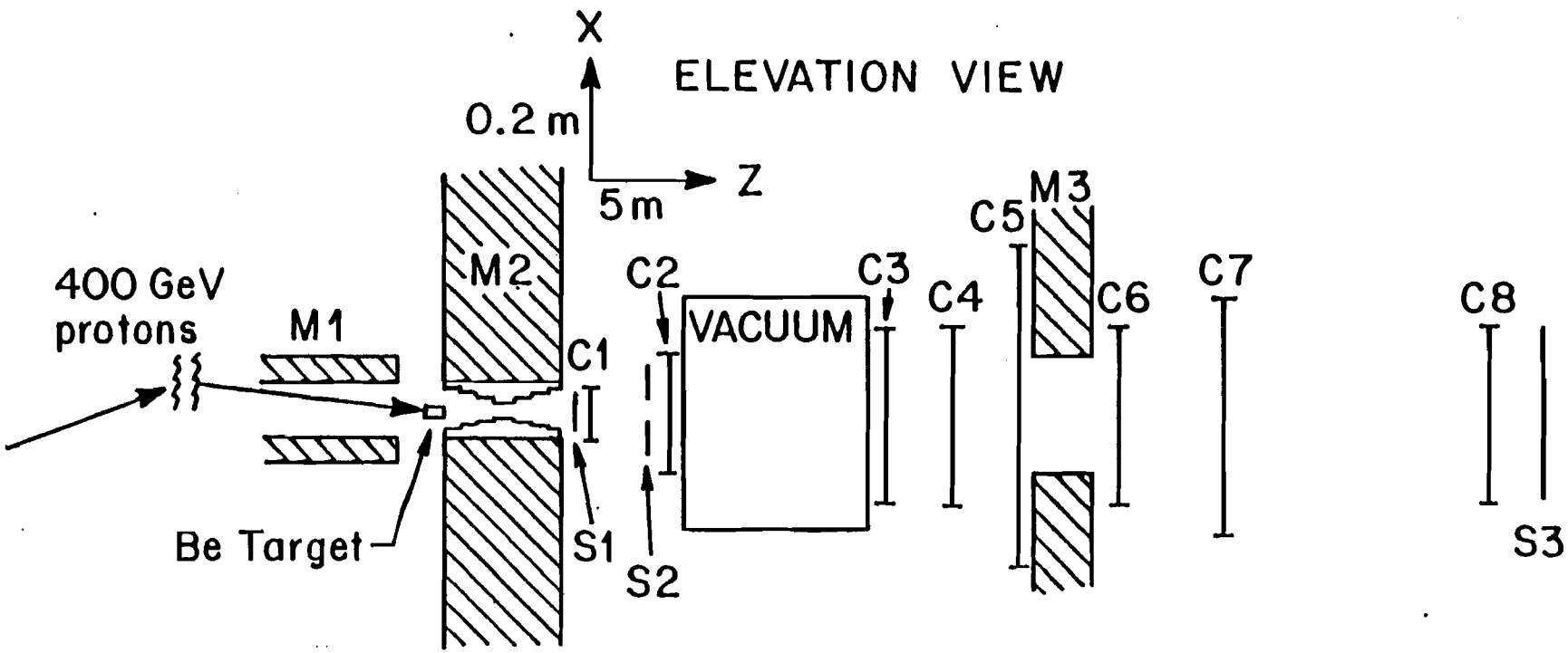


Figure 2.7 Elevation view of the spectrometer.

topology. This provided a very good trigger for $\Xi$'s. Since the beam coming out of the precession magnet contained only negative particles, the presence of a high-momentum positive particle was a good indication of a $\Lambda$ decay. Chambers 7 and 8 were divided into "positive" and "negative" segments, R and L. The "trigger boundary" in C7 was aligned such that all negative particles would hit the negative segment of the chamber. C8 was divided so that all positive particles would hit the positive segment of the chamber. This chamber also provided an additional hit on the proton track which was useful to maintain good momentum resolution for higher momentum particles.

S3 was a 20-cm x 60-cm counter located directly behind C8. It covered the active area of C8, in particular the region where the protons hit. This counter was used as the timing signal for the fast electronics.

The proportional chambers were of conventional design and are described in detail elsewhere.[22] C1 had 24 vertical x 32 horizontal wires. C2 had 128 v x 128 h wires. C3 and C8 had 256 v x 128 h wires. C4 had 128 x 128 wires rotated by 45 degrees with respect to the x-y plane of the coordinate system. C5 had 152 h x 256 v wires. C6 had 128 h x 316 v wires. C7 had 640 v x 192 h wires. The signal wire spacing was 2-mm in all chambers except for a third plane in C5 which

was rotated by 45 degrees, and had a spacing of 2.828-mm. The rotated planes were used for resolving ambiguities in the three track reconstruction.

Calibration constants used to transform wire hit information into spatial positions in the coordinate system were determined by the 400 GeV positive beam transmission described earlier.

The chambers were operated on a gas mixture of 99.9% argon, 0.1% freon and bubbled through methylal at 0° C. The operating voltages ranged from 3.1 to 3.5 kilovolts. Helium bags were placed in the spaces between the chambers downstream of the decay volume to reduce multiple scattering.

## 2.6 The Trigger

Both scintillation counter signals and signals from the chamber planes were used in the trigger. About 40-ns after a charged particle passed through the active area of a proportional chamber a prompt signal was generated. For selected chambers or chamber segments, these signals were sent to electronic trigger logic.

Data was taken with three different versions of the $\Xi^-$ trigger. The first set was taken with the trigger requiring charged particle hits in both segments of C7 and the right half of C8, i.e. the trigger was

$$\Xi^- = S1 \cdot C7L \cdot C7R \cdot C8R \cdot S3$$

Approximately 50,000 3-track events were reconstructed for this trigger. Approximately 30,000 events were reconstructed for the second trigger version

$$\Xi^- = S1 \cdot \overline{S2} \cdot C7L \cdot C8R \cdot S3$$

It was found that the C7R trigger requirement biased the sample towards events having higher momentum. It was also found that in both these sets the $\Xi^-$ yield was low because of background from charged particle interactions. The trigger was modified to be less restrictive as far as the proton distribution was concerned by removing the C7R reqirement. In addition the S2 halo counter and C3 were added to increase the yield of good events. The third and final version of the trigger was

$$\Xi^- = S1 . \overline{S2} \cdot C3 \cdot C7L \cdot C8R \cdot S3$$

The remainder of the data was taken with this trigger, yielding approximately 230,000 reconstructed events.

During all of the above running, an auxilliary trigger

$$\pi^- = S1 \cdot \overline{S2} \cdot S3$$

was prescaled by a factor of 512 and mixed with the trigger. (For the 5.13 T-m data the prescale factor was

changed to 1024.) This provided a sample of single tracks, mainly beam pions, for normalization and calibration. Since no chambers were required in the trigger it was used to monitor chamber efficiency.

## 2.7 Data Acquisition

The data acquisition hardware was a conventional CAMAC/PDP-11 system. If the trigger logic was satisfied a chamber read-out process was initiated. During the read-out process, which typically took 0.5 msec, a gate prevented further triggers. Once the event information had been delivered to the computer (via CAMAC), data-taking was resumed. During a beam spill the wire-hit information was stored in the computer memory and transient disk file, and copied on magnetic tape at the end of the beam spill. At this time a set of 24 CAMAC scalers were also recorded. Between 100 and 300 triggers per spill, depending on the incident proton intensity were recorded.

Data were taken under a variety of running conditions. For the field integral of 6.60 T-m data were taken at +5 and -5 mrad. At the 5.13 T-m field, the data were taken at +7.5 and -7.5 mrad as well as +5 and -5 mrad. Table 2.1 shows the number of data tapes taken for each running condition.

## 2.8 Trigger Rates

In order to determine the quality of the triggers written to tape, the raw wire hits were output in picture format for one hundred triggers, including the prescaled pions, written midway through the tape. This was done for one run in each of the categories listed in Table 2.1. The results of these observations are listed in Table 2.2.

The majority of the triggers, which were single negative tracks, were $\pi^-$'s from the Be target, and a small percentage were $\Sigma^-$'s. It was presumed that the single positive tracks resulted from scatters in the downstream end of the collimator. Straight track events generally satisfied the trigger because of accompanying accidental hits. The triggers which were labeled "other three-track" were predominantly $\Xi^-$'s with many extra hits, or where one of the $\pi^-$'s did not get through the analyzing magnet.

| Data Set | Trigger | $\int B \cdot dl$ | Production Angle +5.0 | -5.0 | +7.5 | -7.5 |
|---|---|---|---|---|---|---|
| 1 | $S1 \cdot S3 \cdot C7L \cdot C7R \cdot C8R$ | 6.60 T-m | 8 | 8 | | |
| 2 | $S1 \cdot \overline{S2} \cdot S3 \cdot C7L \cdot C8R$ | 6.60 T-m | 5 | 7 | | |
| 3 | $S1 \cdot \overline{S2} \cdot S3 \cdot C4 \cdot C7L \cdot C8R$ | 6.60 T-m | 15 | 16 | | |
| 4 | $S1 \cdot \overline{S2} \cdot S3 \cdot C4 \cdot C7L \cdot C8R$ | 5.13 T-m | 6 | 6 | | |
| 5 | $S1 \cdot \overline{S2} \cdot S3 \cdot C4 \cdot C7L \cdot C8R$ | 5.13 T-m | | | 4 | 4 |

Table 2.1 Summary of Data Tapes
(typically 80,00 raw triggers/tape)

| Trigger \ Set | 1 | 2 | 3 | 4 | 5 |
|---|---|---|---|---|---|
| single negative + accidental(s) | 12 | 29 | 45 | 56 | 44 |
| single negative (prescaled) | 4 | 9 | 8 | 4 | 7 |
| unrecognizable | 63 | 33 | 19 | 6 | 10 |
| positive track | 7 | 14 | 15 | 15 | 14 |
| two tracks | 8 | 6 | 4 | 2 | 6 |
| good 3-track | 5 | 11 | 4 | 9 | 11 |
| 3-track late vertex | 0 | 6 | 2 | 4 | 4 |
| other 3-track | 1 | 2 | 1 | 4 | 4 |

Table 2.2 Summary of Raw Trigger Rates
(occurences per 100 triggers)

# CHAPTER 3

# Event Reconstruction

## 3.1 Pattern Recognition

Events were reconstructed from the MWPC data using a pattern-recognition, track-finding routine which searched for events having a three-track, two-vertex topology. One of the tracks was required to be a high-momentum positively-charged track, while the other two were of lower momentum and negatively charged. The momentum and charge were determined from the bend angle in the analyzing magnet.

Raw wire information was read from the raw data tapes and decoded. The hits were then sorted and converted to x

and y coordinates by using the calibration constants discussed in Section 2.5. The wire hits for each event were then studied and classified according to the quality codes listed in Table 3.1. (The event selection procedure is shown schematically at the end of Sec. 3.2.)

Categories 2,3,4 and 5 were determined solely on the basis of the number of wires hit. Approximately 64% of the triggers were in this group. Of these 2-3% were three track events in which one or both of the decays occured after C4 and thus lacked enough information to continue with the reconstruction. The remaining triggers were then searched for three tracks in the y view. Events in categories 6 and 12 were eliminated from the sample at this point.

Track fitting involved selecting the hits which had the best fits to straight lines. From the y tracks, hits in C4 and the diagonal plane of C5 could be correlated with hits in the x plane, and tracks in x could be fit. The x tracks had to be constructed separately upstream and downstream of the magnet. The upstream tracks were matched with the downstream tracks by their intersection at the magnet bend center. Events in which x tracks could not be properly found were put into categories 7, 8 and 9.

For the remaining events, 6% of the triggers,

| | |
|---|---|
| 1 | Three track event,only one hit in the x view after AVIS |
| 2 | Three of the four planes of chambers 3 and 4 have less than two hits |
| 3 | Four of the six downstream y planes have 4 or more hits |
| 4 | Four of the six downstream y planes have less than two hits |
| 5 | Less than two of the y planes of chambers 3, 5, 6 and 7 have two or three hits |
| 6 | Cannot find more than two points on one of the y plane tracks |
| 7 | Three tracks in y view but cannot find them in x |
| 8 | Three tracks befor Avis, but only two tracks after |
| 9 | The stiff track bends the same way as one of the soft tracks |
| 10 | Bad chi-square in geometrical fit |
| 11 | Geometrical chi-square greater than 80 |
| 12 | Two track event in y view |
| 0 | Good three track topology |

Table 3.1 Reconstruction Quality Codes

preliminary vertices were then calculated by fitting the tracks to the $\Xi \rightarrow \Lambda\ \pi^-$, and $\Lambda \rightarrow p\ \pi^-$ topologies. If the $\Lambda$ vertex was found to be upstream of the $\Xi$ vertex the negative tracks were interchanged and the vertices recalculated.

Using the reconstructed slopes and chamber hits as well as the vertex information an overall geometric $\chi^2$ for the event was calculated. Events with a $\chi^2$ greater than 80 (for approximately 18 degrees of freedom) were cut from the sample. These events, less than 1% of all the triggers and 10% of those which were fit, were put in categories 10 and 11. The remaining events were identified as good three track events. The events were then checked to be sure the $\Lambda$ vertex was indeed downstream of the $\Xi$ vertex. If this was not the case the event was eliminated from the sample. This occurred in about 7% of the $\chi^2 < 80$ events. The geometric $\chi^2$ distribution is shown in Fig. 3.1. Details of the geometric fit are described in Appendix A.

## 3.2 Event Identification

Using the reconstructed slopes for the proton and pion identified as the $\Lambda$ decay product, the momentum of these two

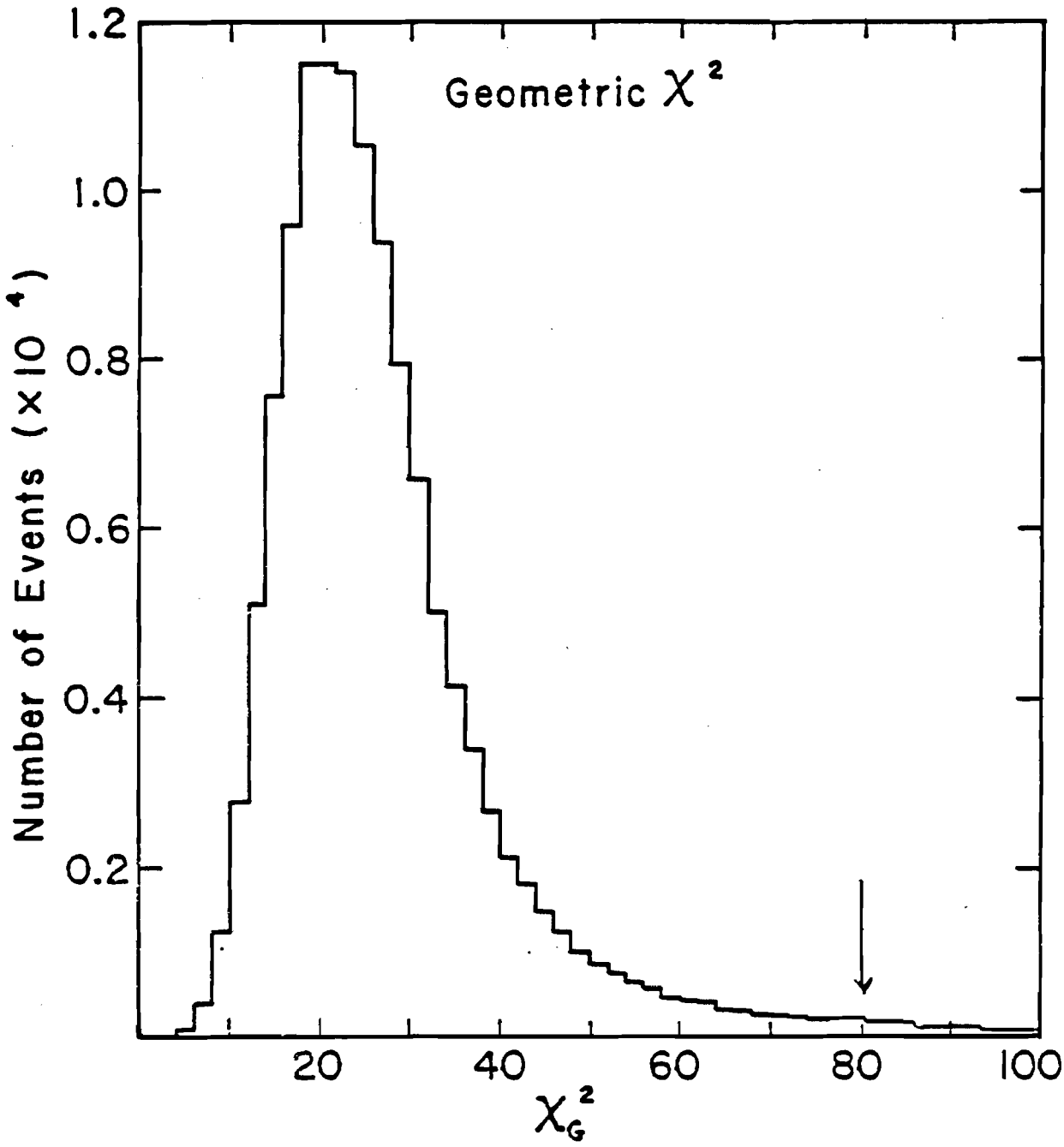


Figure 3.1 Geometric $\chi^2$ distribution for three track events with vertex separation greater than zero. The arrow indicates where the data was cut.

particles was determined. From the momenta and opening angle the momentum and invariant mass of the $\Lambda$ was calculated. This is shown in Fig. 3.2. The momentum as well as the proton and pion momentum vectors were then adjusted by constraining the event to fit the $\Lambda$ mass. The $\chi^2$ distribution for this additional constraint is shown in Fig. 3.3. This "kinematic" $\chi^2$ was required to be less than 20. The cut at 20 was made based on a comparison with a Monte Carlo distribution. This fit is also discussed in Appendix A.

Using the momentum of the second negative track, and the $\Lambda$ momentum before being adjusted by the kinematic fit, the $\Xi^-$ invariant mass was constructed. This distribution is shown in Fig. 3.4. The $\Xi^-$ mass was required to lie between 1.306 and 1.338 GeV/$c^2$ . Events not within this range were tested under the hypothesis that the second negative track was a kaon, and a $\Lambda$-$K^-$invariant mass was calculated. If this mass was between 1.65 and 1.70 GeV/$c^2$ the event was flagged as an $\Omega^-$ candidate. The mass plot for this region after all event selection criteria were applied (except a $\Xi^-$ mass cut) is shown in Fig. 3.5.

In addition to these requirements the $\Xi^-$ momentum vector was projected back to the production target, and each event was required to point within $R^2$ = 40-mm$^2$ of the target

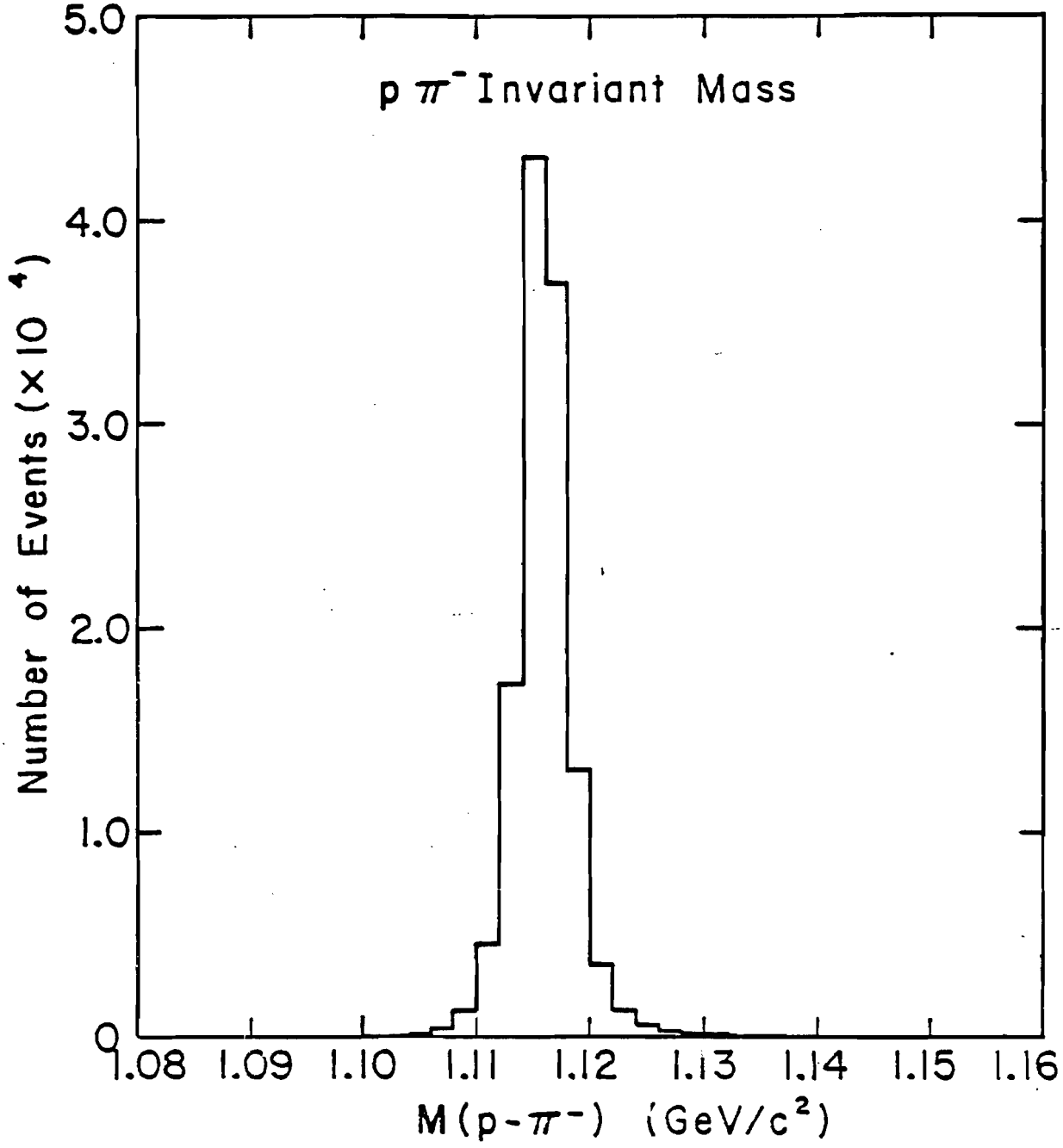


Figure 3.2 p-$\pi^-$ invariant mass distribution for events with geometric less than 80 and vertex separation greater than zero. No kinematic constraints been required.

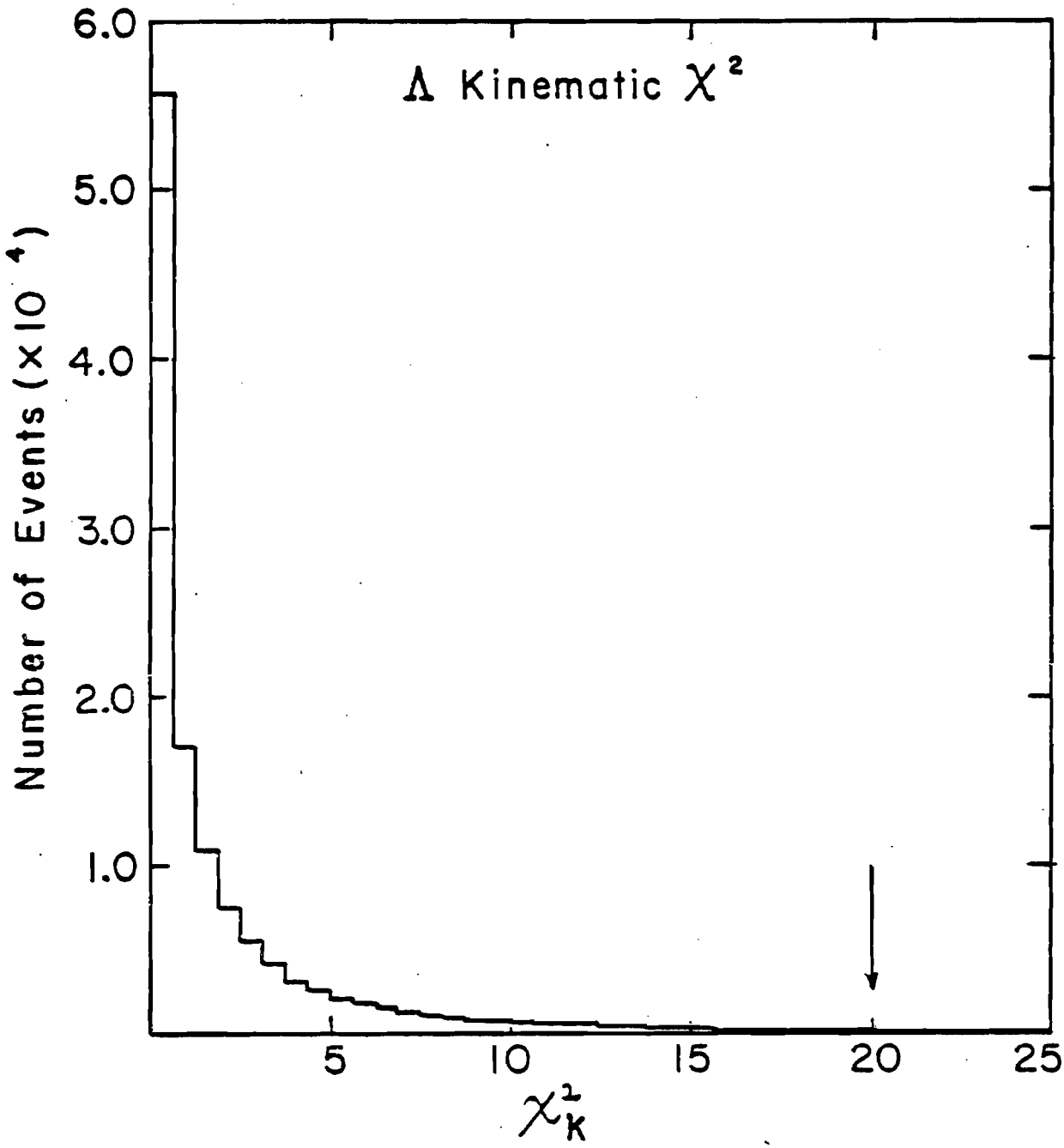


Figure 3.3 Kinematic $\chi^2$ distribution for p-$\pi^-$ constrained to fit the $\Lambda$ mass. The arrow indicates where the data was cut.

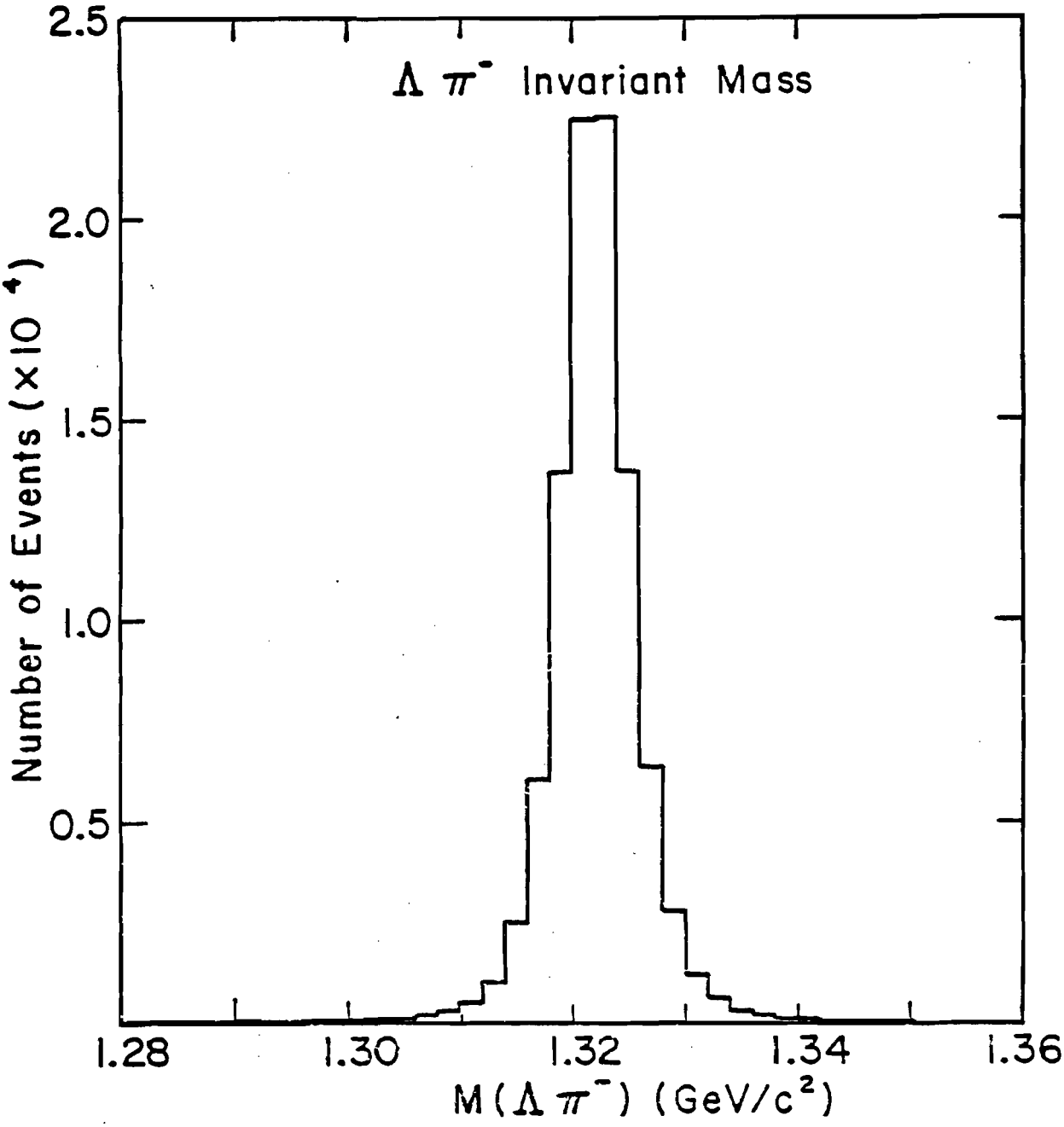


Figure 3.4 $\Lambda$-$\pi^-$ invariant mass for events having a kinematic $\chi^2$ less than 20.

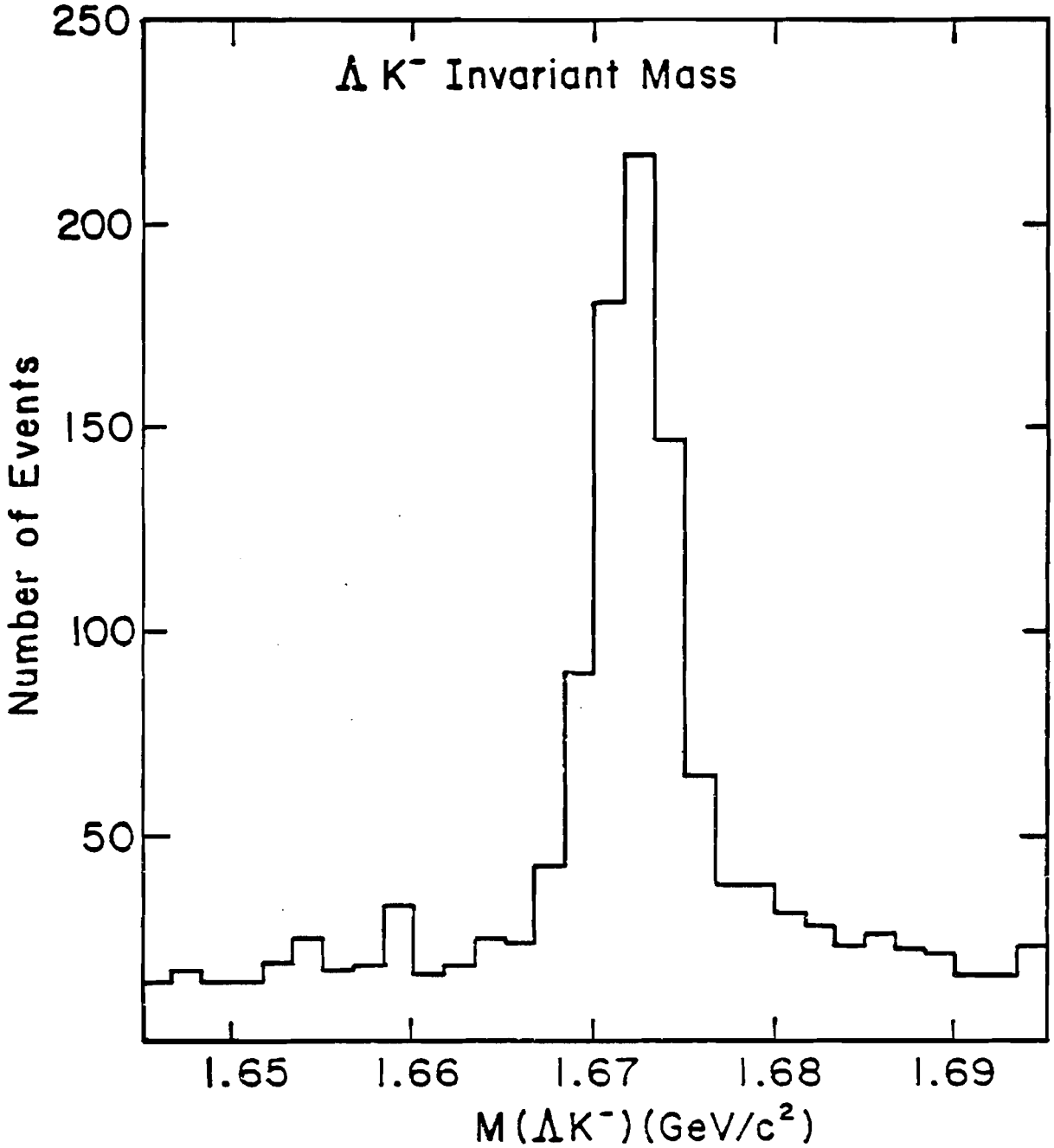


Figure 3.5 $\Lambda$-$K^-$ invariant mass distribution for events passing all cuts except the mass cut.

center. ($R^2$ is the square of the distance between the production target center and the $\Xi^-$ momentum vector extrapolated back through the curved channel to the target plane.) This cut was made to eliminate $\Xi^-$'s from sources other than the production target. This is discussed in more detail in Section 3.4. For the same reason, events with momentum below 105 GeV/c were eliminated from the 5.13 T-m data. A similar cut was made at 125 GeV/c in the 6.60 T-m data. High momentum cuts were made at 290, 270 and 250 GeV/c for the 6.6 T-m, 5.1 T-m (5 mrad) and 5.1 T-m (7.5 mrad) data respectively.

It was also found from Monte Carlo studies and the effect on the $\Omega^-$ candidates that requiring the primary vertex to be greater than zero helped to eliminate background events. This vertex cut was also made to insure that all the $\Xi^-$ events passed through the full length of the precession field.

The $\Xi^-$ invariant mass, calculated using the fitted $\Lambda$ momentum, for events passing all cuts is shown in Fig. 3.6. Vertex and momentum distributions for the $\Xi^-$ events passing all the cuts are shown in Figs. 3.7-3.13. The vertex distributions are compared with the Monte Carlo events described in the following section. (Note that all the distributions shown are for Data Set 3 - 5 mrad, 6.60 T-m

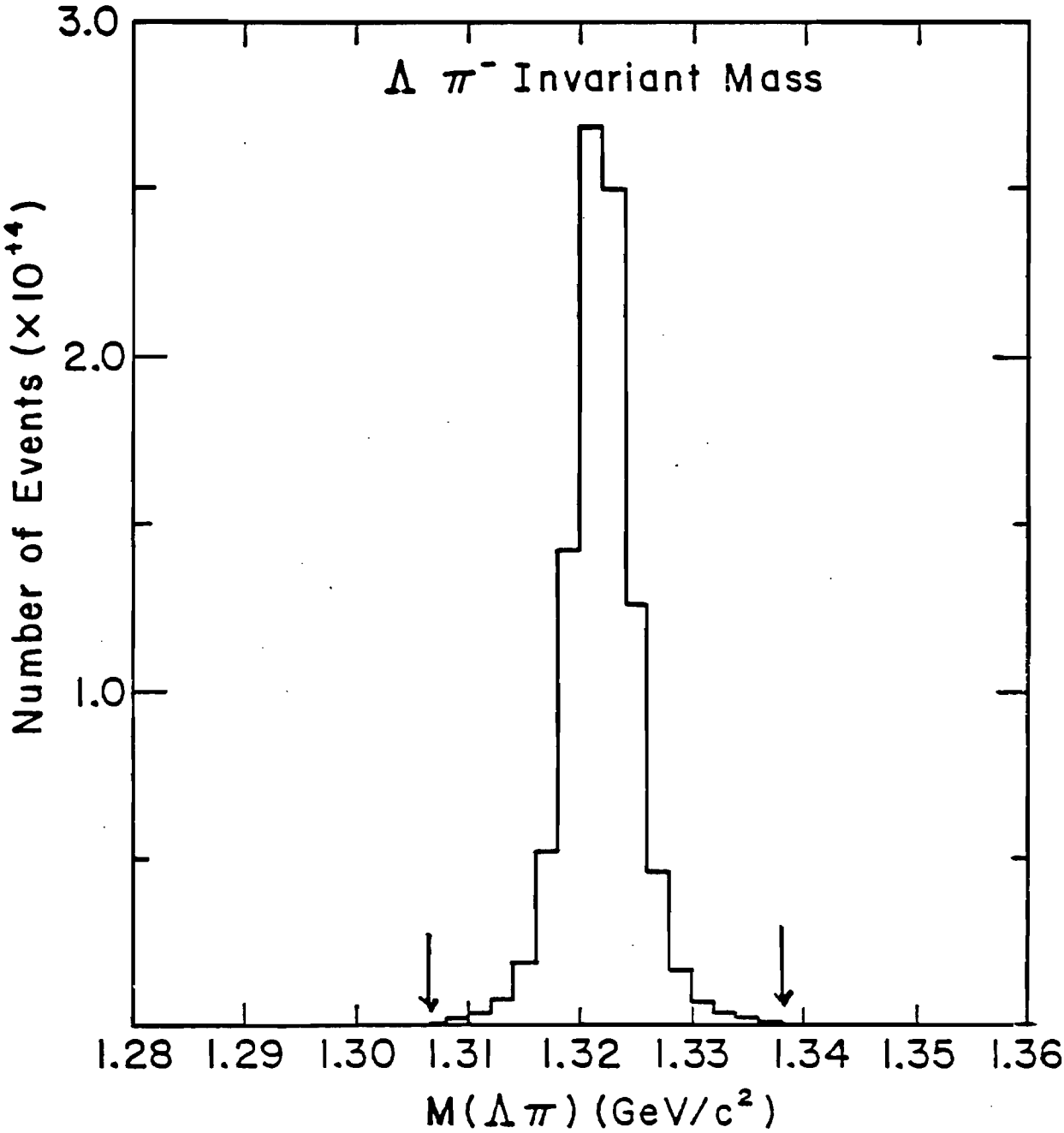


Figure 3.6 $\Lambda$-$\pi^-$ invariant mass distribution using the fitted $\Lambda$ momentum, for events passing all cuts. The mass has been required to be between 1.306 and 1.338 GeV/$c^2$. This cut is indicated by the arrows.

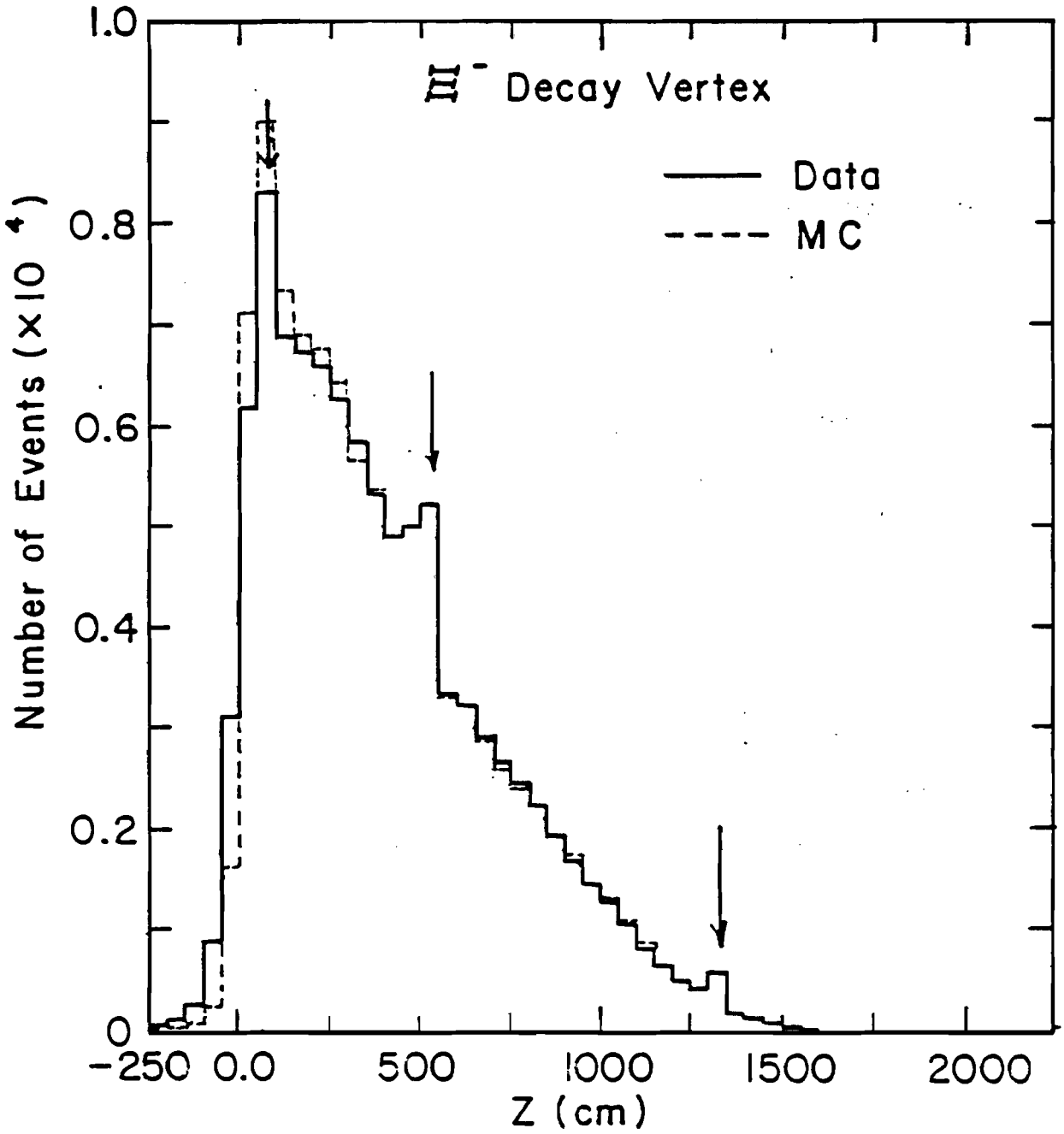


Figure 3.7 $\Xi^-$ z-vertex distribution for events passing all cuts except the vertex cut, which was made at zero. The arrows show the positions of chambers 1,2 and 3, where the reconstruction program has a tendency to fix decay verticies A Monte Carlo distribution is also plotted for comparison.

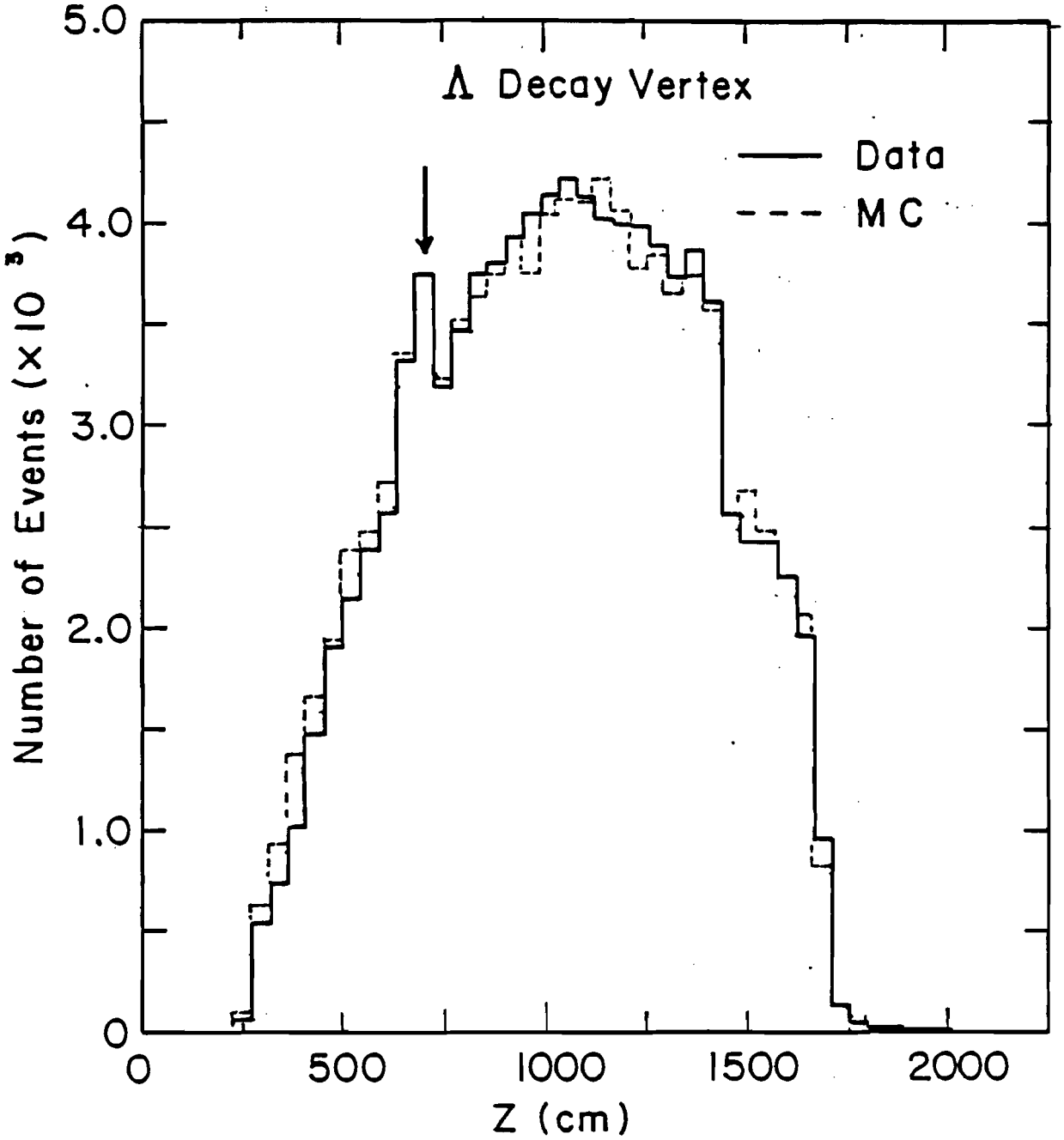


Figure 3.8 Λ z vertex distribution for events passing all cuts. The position of C2 is indicated by the arrow. A MC distribution is shown for comparison.

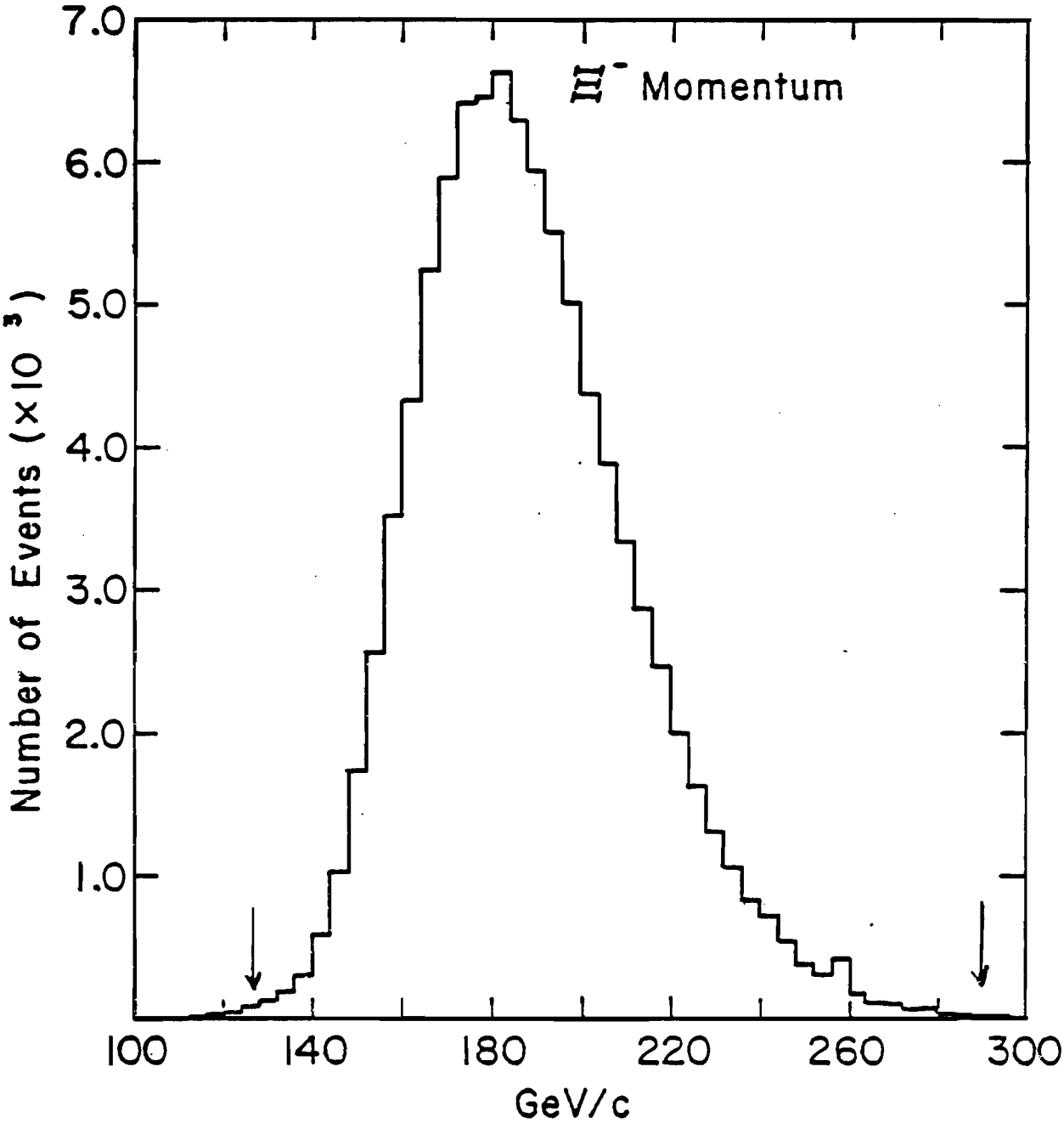


Figure 3.9 $\Xi^-$ momentum distribution for 5 mrad, 6.6 T-m field. The arrows indicate where this sample was cut.

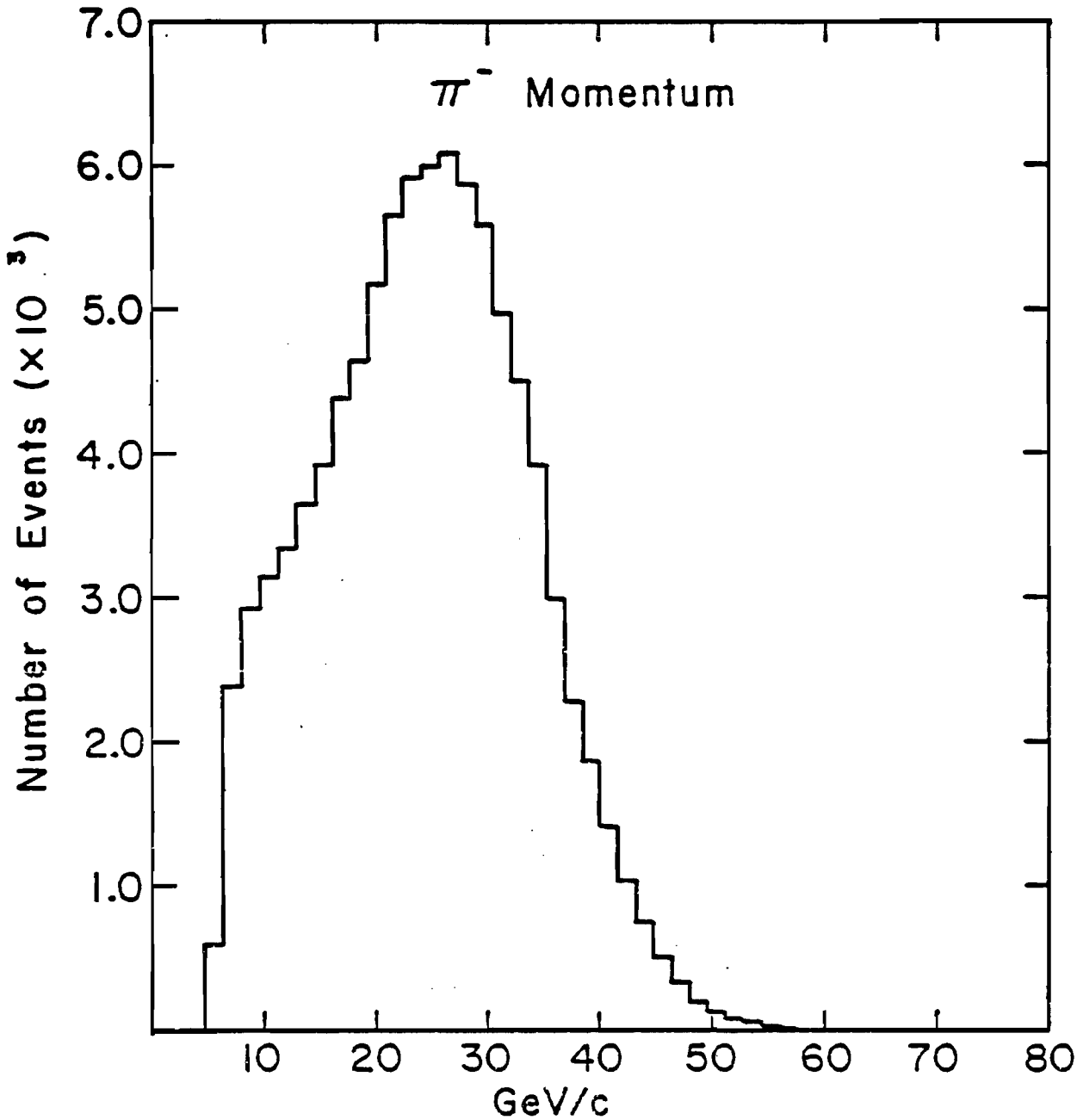


Figure 3.10 Momentum distribution of pions from the $\Xi^- \to \Lambda\pi^-$ decay.

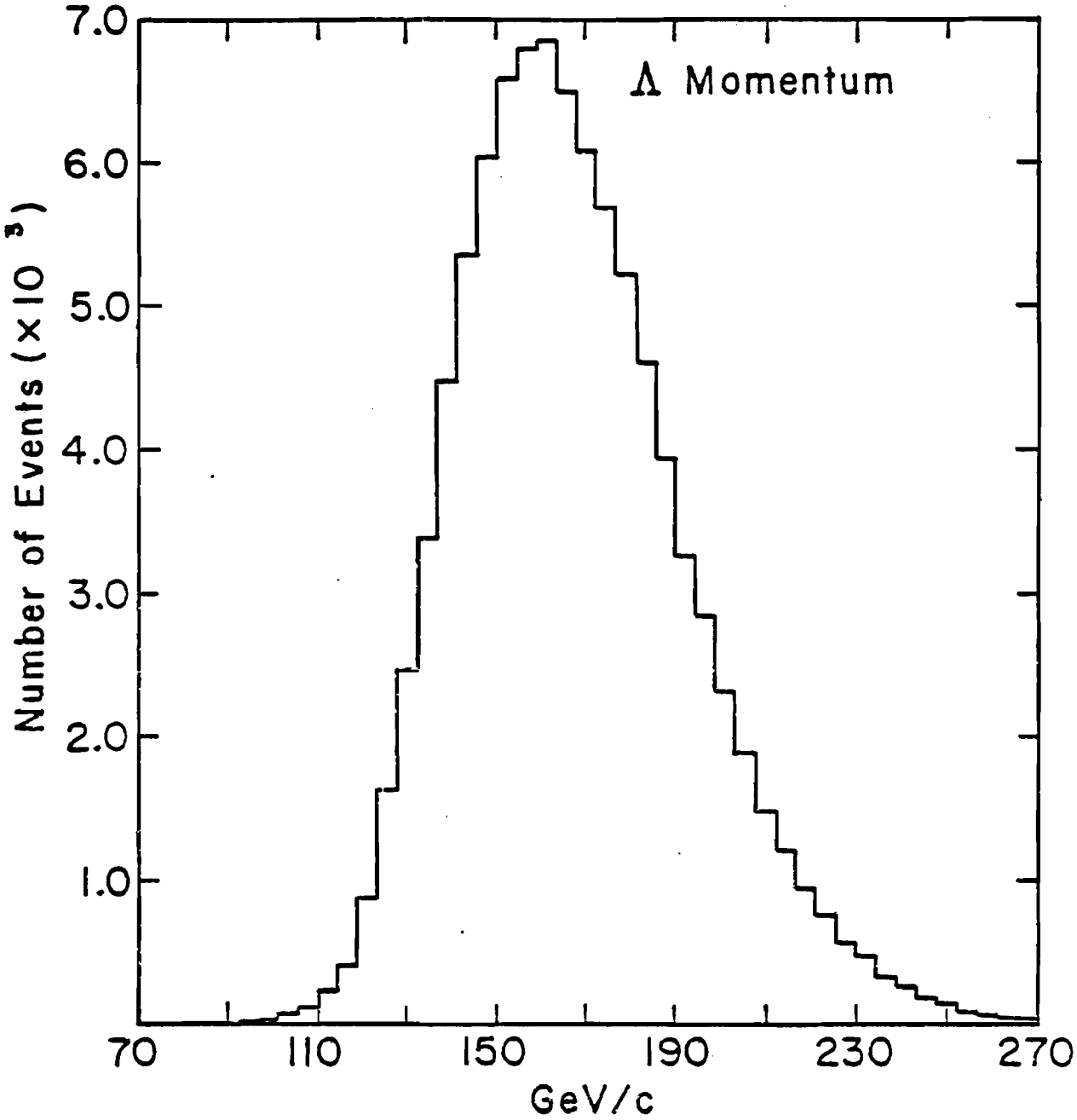


Figure 3.11 Momentum distribution of $\Lambda$'s from the $\Xi^- \to \Lambda \pi^-$ decay.

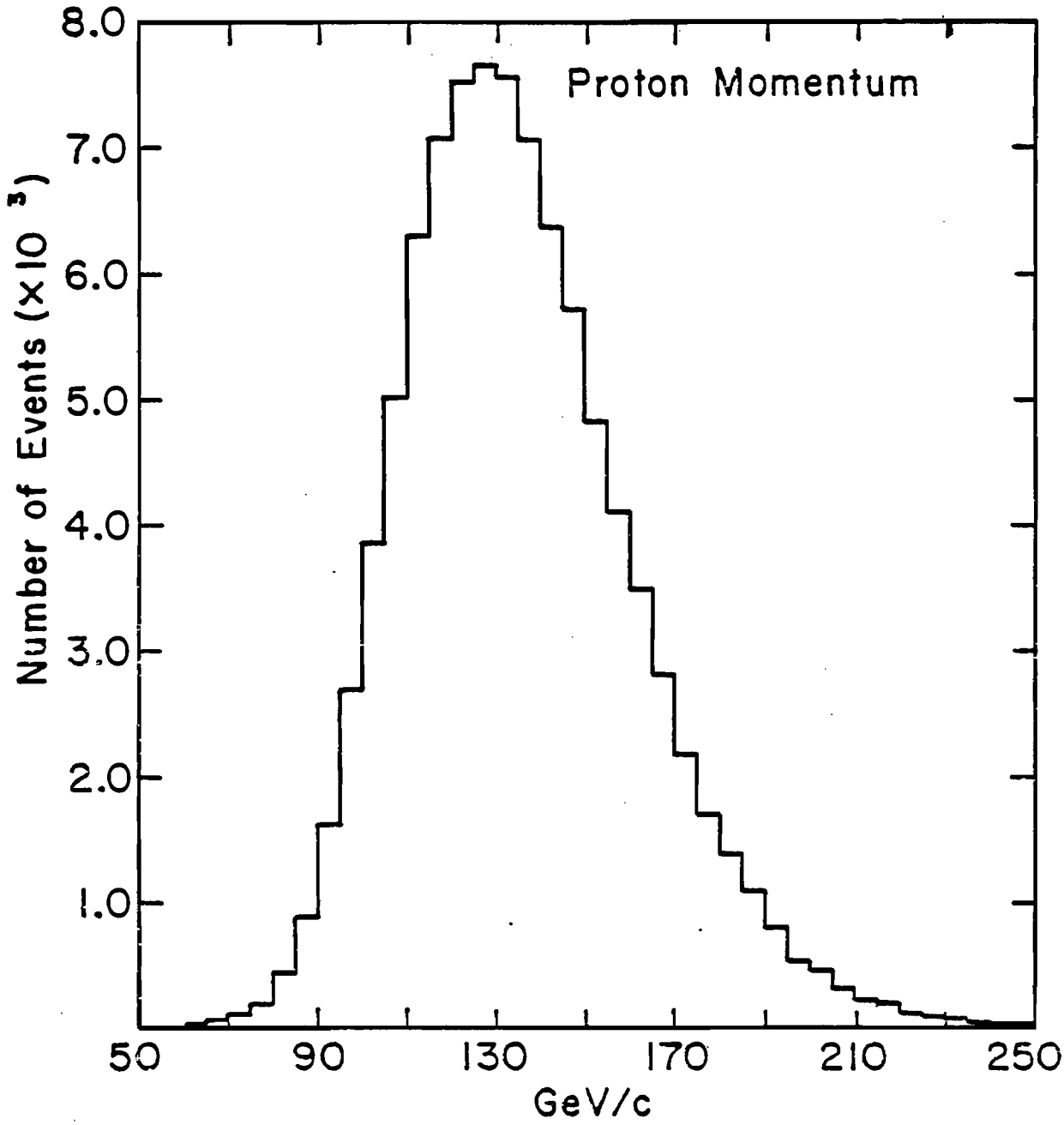


Figure 3.12 Momentum distribution of protons from the $\Lambda \rightarrow p\,\pi^-$ decay.

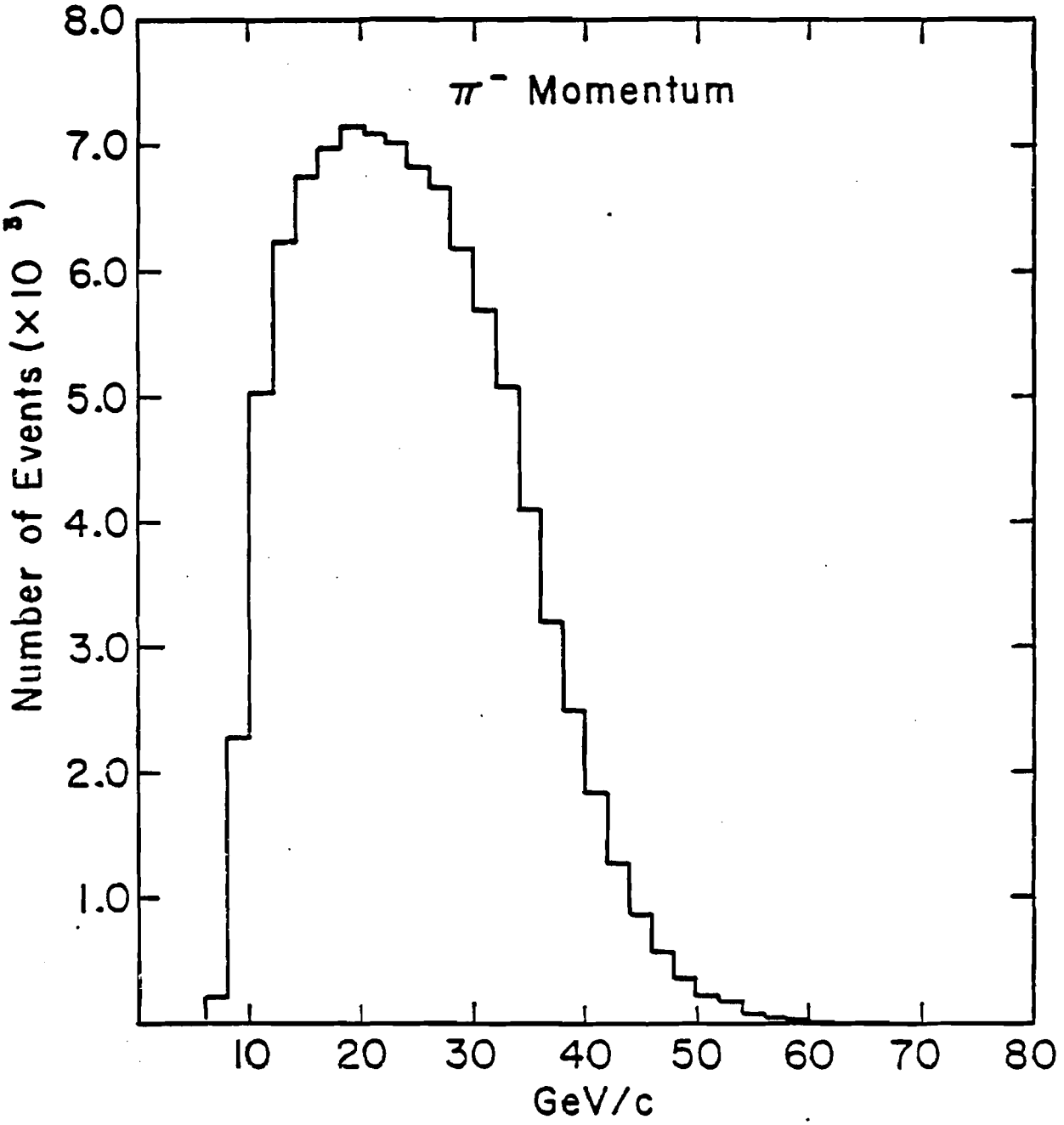


Figure 3.13 Momentum distribution of pions from the $\Lambda \rightarrow p\pi^-$ decay.

field.) Fig. 3.14 shows a schematic diagram of the event selection process.

## 3.3 The Monte Carlo Program

In order to determine the efficiency and resolution of the reconstruction procedure, a Monte Carlo (MC) program was used. The MC was also used to determine the sample purity as well as to study the apparatus acceptance as a function of event parameters such as momentum, vertex position and angular distribution.

### 3.3.1 Monte Carlo Event Generation

Events were generated from random points gaussianly distributed in a disc "target", 6 in diameter. The total momentum of the was allowed to range between 120 and 340 GeV/c. The shape of the momentum distribution was chosen to match the momentum spectrum of the real events. The initial direction of the particle was chosen at random, and the subsequent trajectory tested for acceptance through the collimator.

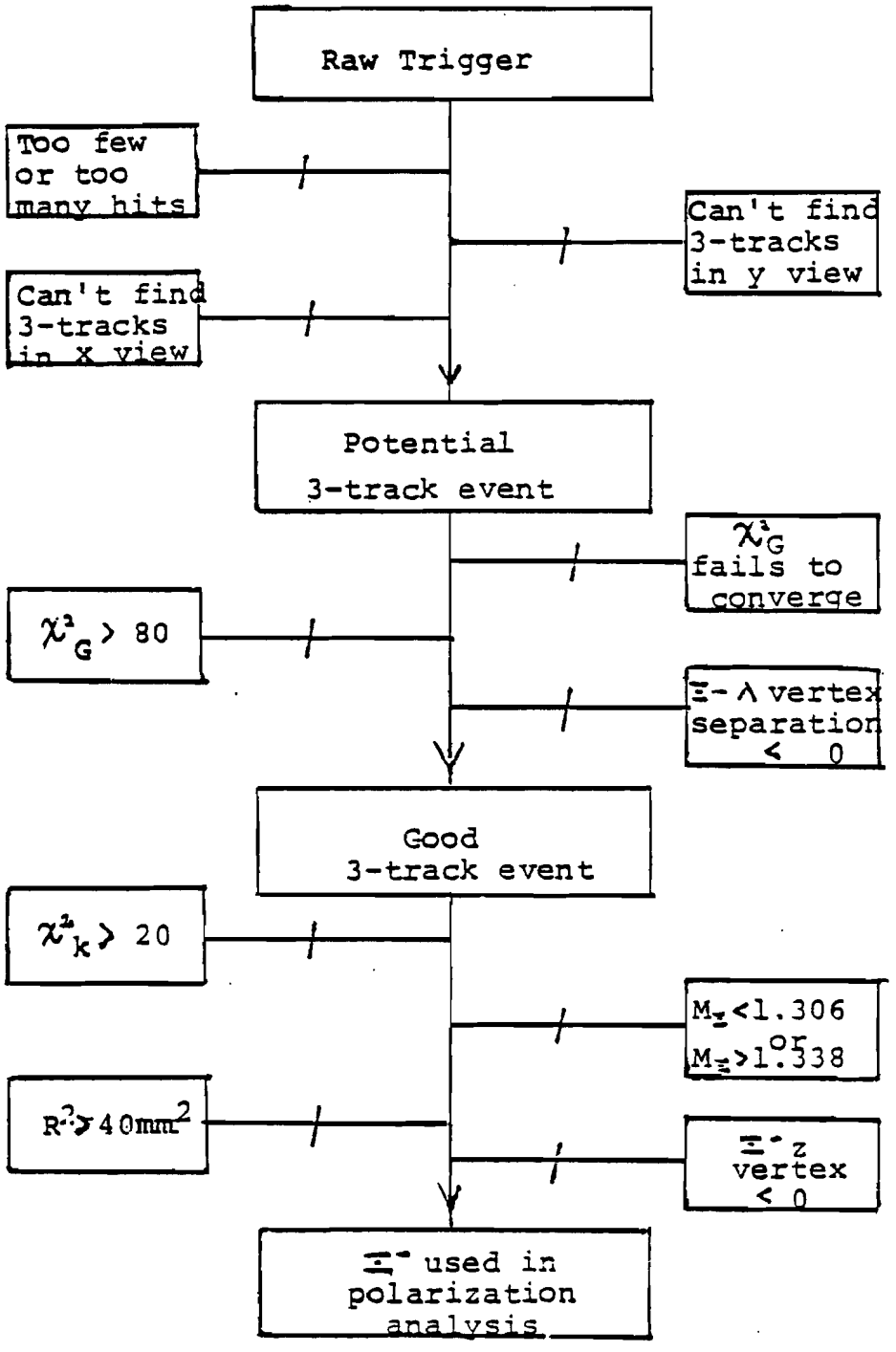


Figure 3.14 Schematic Diagram of the event selection process.

Events which were accepted into the spectrometer were allowed to decay at a position L in the spectrometer according to an exponential decay law, $\exp(-L/c\tau)$. Except when it was desired to study the effects of $\Xi^-$ decay in the channel, L was required to be greater than zero. Events were required to pass through all the spectrometer apertures, and strike all detectors required for the event trigger. The geometric acceptance of the collimator and spectrometer as a function of momentum is shown in Fig. 3.15.

For each event wire hits were calculated for all the charged particles. This included producing two adjacent hits if the particle passed through a central region between two wires. It also included reproducing the chamber efficiencies observed in the data and allowing the $\pi^-$'s to decay and adjusting the wire hits accordingly. The wire hits were passed to the reconstruction program in the same manner as the real event information. Events were generated with both isotropic and polarized decay distributions. Both the generated and reconstructed parameters such as momenta and vertices for 200,000 MC events, both polarized and isotropic, were written to magnetic tape so that these could be analyzed in the same manner as the real events. These results are discussed in Section 4.8.

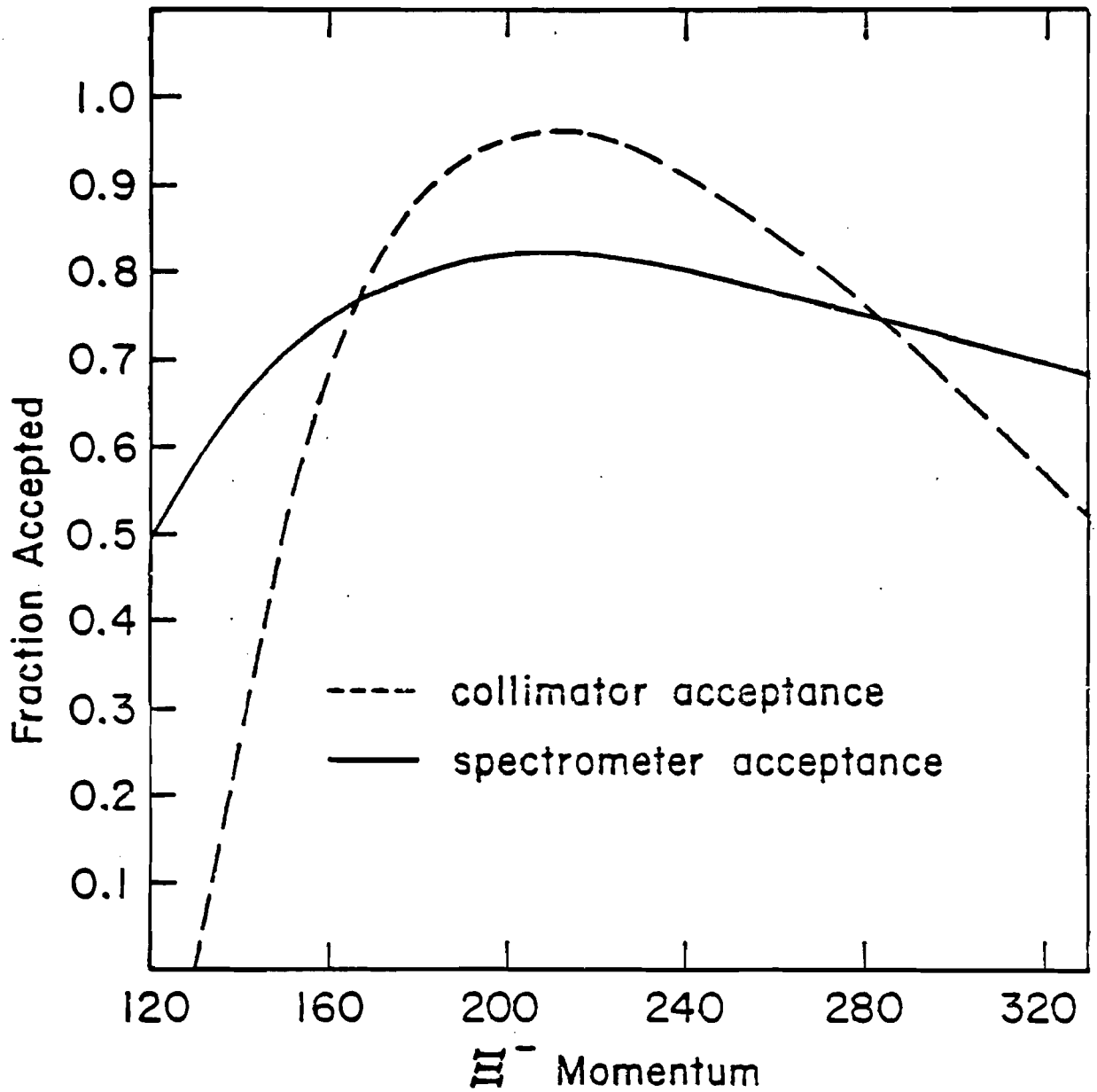


Figure 3.15 Geometric acceptance of the spectrometer and collimator. The collimator acceptance is shown for a 6.6 T-m field integral.

### 3.3.2 Monte Carlo Event Reconstruction

The reconstruction efficiency for MC events having a $\Lambda$ vertex upstream of C3 was 90%. The major property of MC events which failed to reconstruct was a narrow opening angle between two or more of the tracks. This most often resulted in insufficient wire information causing the event to fail early in the reconstruction program. This occurred for 4% of the events. 1.5% of the events identified as three-track events failed to converge in the geometric fitting program or had a geometric $\chi^2$ greater than 80. 4.5% of the remaining events failed to have a kinematic $\chi^2$ less than 20.

Two percent of the events had a reconstructed $\Xi^-$ vertex less than zero. This happened when the upstream hits were close together and track identification was difficult.

More than 98% of all the surviving MC events pointed back to within 40-mm$^2$ of the center of the production target. The $\chi^2$ distribution for the MC events is shown in Fig. 3.16. The momentum resolution for the $\Xi^-$ and $\Lambda$ was between 3 and 4%. The $\sigma$ for the $\Lambda$ and $\Xi^-$ masses were 1.99 and 2.37 MeV/c$^2$ respectively, compared with 2.14 and 3.19 for real data.

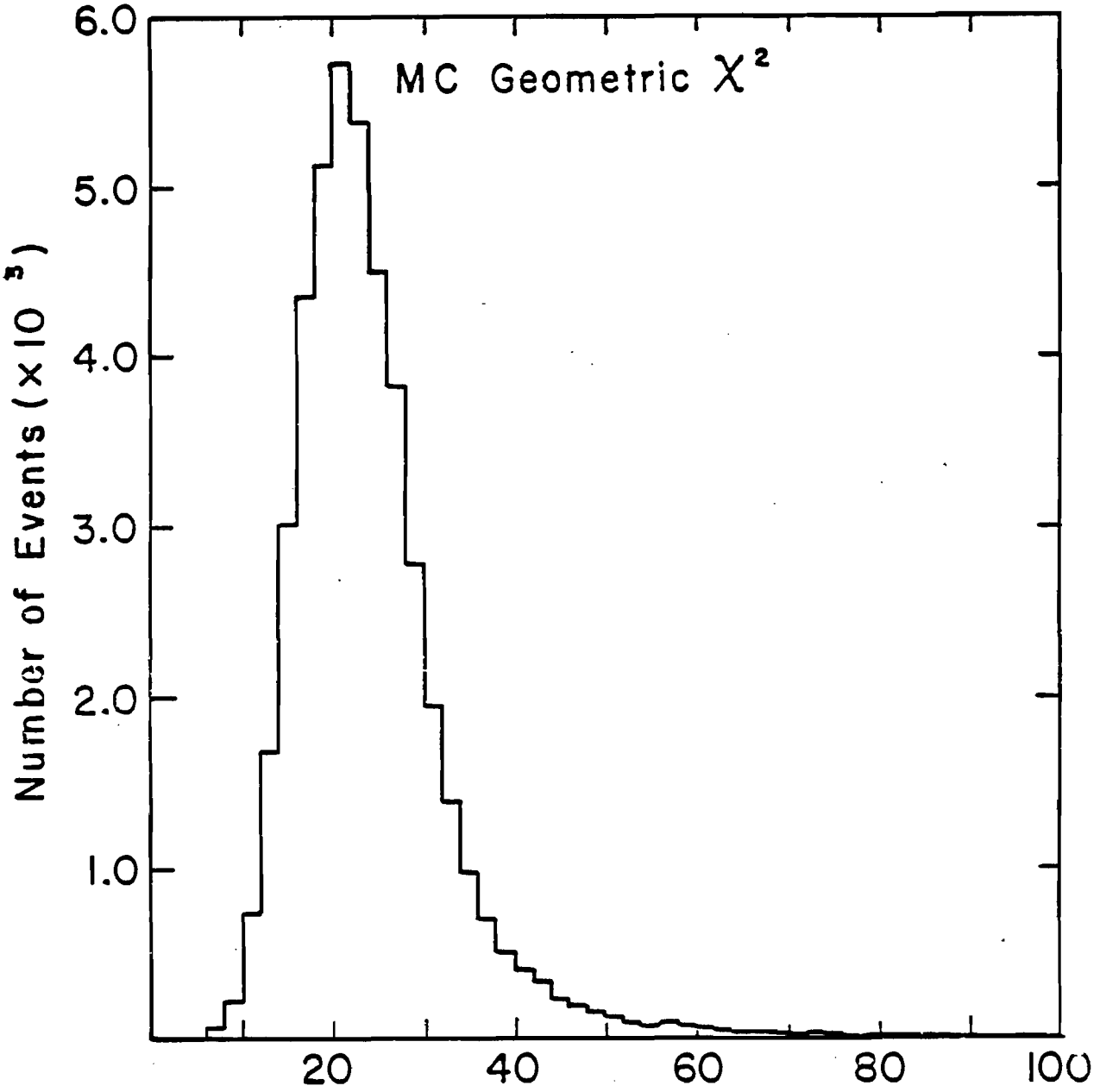


Figure 3.16 Geometric $\chi^2$ distribution for reconstructed Monte Carlo events.

It should be noted that the MC $\chi^2$ distribution peaks in the same place as the real event distribution, though it is narrower in the region $30 < \chi^2 < 60$. This difference, and the better mass resolution in the MC than the data, is attributed to the combined result of a number of effects which have not been included in the Monte Carlo. Examples of these effects are multiple scattering from chamber windows and other material in the beam, the existance of a small quadrupole component in the analyzing magnet, and run to run fluctuations in the field in the analyzing magnet. (The affect of the quadrupole field on the real events was studied and found to have no effect on the pattern recognition process. Since the geometrical reconstruction process was well constrained by the event topology, the largest affect of the nonuniformity of the field was to increase the component of the geometrical $\chi^2$ coming from the y-view, particularly for lower momentum particles. This effect was further diminished by the fact that the quadrupole field decreased in the direction of +x, the direction in which the lower momentum negative particles were deflected.) [16]

A comparison of the fraction of events failing the event selection criteria for real and MC events is shown in Table 3.2. When the selection criteria listed in the most left-hand column of the table are applied to the data, the fraction of events failing the requirement listed across the

| Selection Criteria | $Z_\Xi < 0$ | $\chi^2_k > 20$ | $\lvert\Delta M\rvert_\Xi > 0.016$ | $R^2 > 40\ mm^2$ |
|---|---|---|---|---|
| I. geometric $\chi^2 < 80$ | 0.0860 | 0.1086 | 0.1281 | 0.1563 |
| II. vertex separation $> 0$ | 0.0206 | 0.0498 | 0.0146 | 0.0181 |
| I. II. and | | 0.1015 | 0.0843 | 0.1542 |
| III. $Z_\Xi > 0$ | | 0.0491 | 0.0143 | 0.0182 |
| I. II. and | 0.0868 | | 0.0840 | 0.1285 |
| IV. $\chi^2_k < 20$ | 0.0199 | | 0.0063 | 0.0165 |
| I. II. and | 0.0468 | 0.0635 | | 0.1239 |
| V. $\lvert\Delta M\rvert < 0.016$ | 0.0205 | 0.0420 | | 0.0159 |
| I. II. and | 0.0856 | 0.0793 | 0.0946 | |
| VI. $R^2 < 40\ mm^2$ | 0.0210 | 0.0483 | 0.0124 | |
| all cuts except | 0.0488 | | | |
| $\Xi z$ vertex cut | 0.0208 | | | |
| all cuts except | | 0.0550 | | |
| $\chi^2_k$ cut | | 0.0406 | | |
| all cuts except | | | 0.0330 | |
| $\Xi$ mass cut | | | 0.0045 | |
| all cuts except | | | | 0.1179 |
| $R^2$ cut | | | | 0.0148 |

Table 3.2 Real vs Monte Carlo Reconstruction Efficiencies
(lower number in each set is Monte Carlo)

top are given. For example, when the sample is required to pass criteria I and II, 10% of the real events and 5% of the MC events have a kinematic $\chi^2$ greater than 20. However, when all criteria are applied to the events, except the kinematic $\chi^2$ cut, only 5.5% of the real events still have a $\chi^2_k > 20$, compared with 4.1% of the MC events.

## 3.4 Background Studies

It was clear from the distribution of masses, vertices and particle momenta that, before any restrictive cuts were made on the data, the sample was relatively pure. The simple fact that the trigger required the presence of a positive particle, along with the selectivity of the reconstruction program, strongly biased the event selection to $\Xi^-$'s.

An estimate of the background was made by looking at the $\Lambda$-$\pi^-$ invariant mass after all cuts except the $\Xi^-$ mass cut had been made. This was done by using the logarithmic mass plot shown in Fig. 3.17, and interpolating the wings of the distribution under the peak. This constituted 0.7% of the events. When this same procedure was performed on the MC events the result was 0.2%. The MC number is an estimate of the $\Xi^-$'s in the final sample which may have been

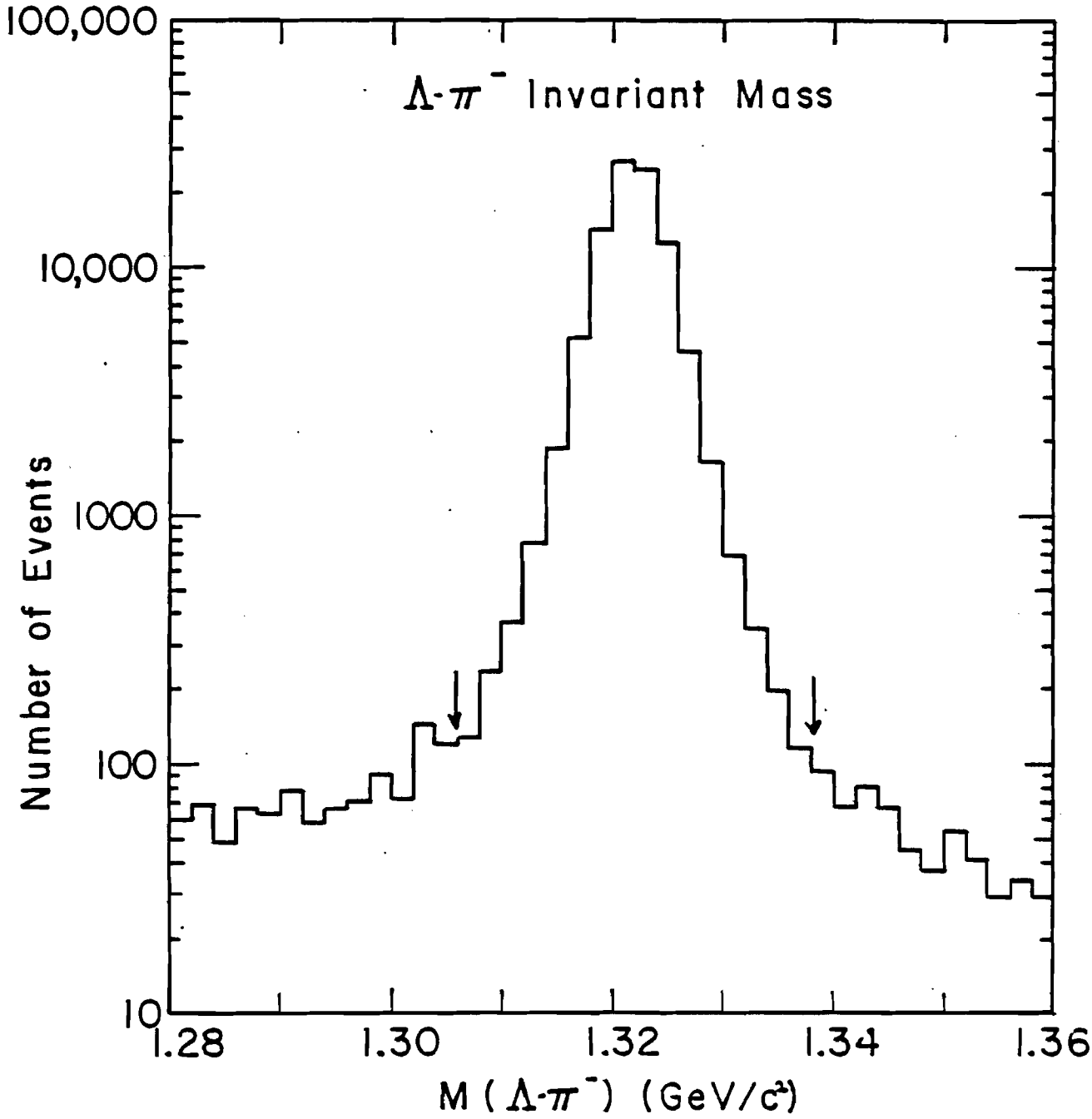


Figure 3.17 Logarithmic distribution of $\Lambda$-$\pi^-$ invariant mass distribution. The arrows indicate where the final cut was made. The background interpolation predicted less than a 1% background under this peak.

reconstructed incorrectly. Possible mechanisms for the background, which appears to be, at most 0.5%, are described below.

### 3.4.1 Monte Carlo Fool Events

Using the Monte Carlo program several types of "fool" events were generated to determine how well the event selection criteria eliminated non-$\Xi^-$ events. The first step in this procedure was to generate random three track events. This was done by combining the proton from one MC event with a $\pi^-$ from each of the next two events generated. This new "event" was then tested to see if it satisfied the trigger requirement. If it did, the wire hits were passed to the reconstruction program. This type of event attempted to simulate a "junk" trigger, i.e. a charged particle interaction from scattering in chamber windows etc. These tracks were far from random since the particles used were protons and pions from $\Xi^-$ decays. Thus, this test was more likely to simulate a $\Xi^-$ trigger than truly random interactions. It was found that only 20% of these events had geometric $\chi^2$ 's less than 100. After all cuts were imposed on these triggers less than 0.3% remained. From studying pictures of raw triggers, random three track triggers were

estimated to occur less than 1% of the time. This would result in less than a 0.003% background in the final sample.

Events were also generated in which the $\Lambda$ from a $\Xi^-$ decay was combined with either a $\Sigma^-$ track and its decay pion, or a $\pi^-$ from the target, since these were the major components of the negative charged beam. This was intended to simulate events in which the $\Xi^-$ decayed near the downstream end of the collimator and the was lost but the $\Lambda$ decayed in the spectrometer. From the MC study this could occur for 22% of the $\Xi^-$'s decaying between the defining collimator and the exit aperture. Twenty nine percent of the $\Sigma - \Lambda$ events had geometric $\chi^2$'s less than 100. Two percent survived all cuts. A calculation based on a charged particle rate of $3 \times 10^5$ particles/sec, and gate width of 120 nsec shows that the probability for these type triggers occuring was less than 4%. It was concluded therefore that they would contribute at most a 0.02% background in the final sample.

For the $\pi - \Lambda$ triggers it was found, as it should be, that the reconstruction program was unable to find a $\Xi^-$ vertex in the spectrometer. None of these events, of 10,000 analyzed, remained after the z vertex cut at zero had been made, contributing less than 0.01% to a background.

A background known to exist in the data was $\Omega^-$ events.

These events pass all the event selection criteria except possibly the $\Xi^-$ mass cut. After all cuts, including the mass cut, 4.5% of $\Omega$ MC events remain. An independent analysis of the $\Omega^-$ candidates, from this experiment, results in a sample of 2000 events for 200,000 $\Xi^-$ events.[23] Thus the $\Omega$'s were a background of 0.05%, clearly the largest accountable source of non-$\Xi^-$ background.

All of these sources account for at most 0.1% non-$\Xi^-$ background. That this is approximately a factor of five less than that calculated from the mass distribution is attributed to the Monte Carlo subtraction of 0.02% being an underestimate of the true width of the distribution for real $\Xi^-$'s.

### 3.4.2 Collimator Production

Twelve percent of the $\Xi^-$ events failed to lie within 6.6 mm of the center of the production target. These events, which pass all other selection criteria, indicate a source (or sources) of $\Xi^-$'s other than the production target. A logarithmic plot of the $R^2$ distribution for the 5 mrad, 6.6 T-m data for all momenta is shown in Fig. 3.18. This data was then plotted as a function of momentum. This is shown in

Fig. 3.19. It is clear that essentially none of the events below 120 GeV come from the target. This is not surprising since the channel acceptance (shown in Fig. 3.15) for events below 120 GeV/c (at 6.60 T-m) is zero. Using the events below 120 GeV to determine the shape of the $R^2$ distribution for non-target events, the percentage of events within the $R^2$ cut of 40 $mm^2$, that come from a source other than the target was estimated to be less than 1%.

Events with $R^2$ greater than 1 cm were examined to see if their source could be found. This was done by projecting the $\Xi^-$ momentum vector back to various z positions, both in the collimator and upstream of the target. The events were found to point back (well within resolution) to the defining aperture. Upstream of the target they were diffusely distributed. They were found to have a high concentration about midway between the production target and the defining collimator. This region was examined separately for the positive and negative production angles. It was found that the positive data was concentrated on the lower portion of the collimator while negative production angle data was concentrated on the upper portion. These sources were where the proton beam struck the collimator. These events, mostly $\Xi$'s, were eliminated from the sample by the $R^2$ cut as well as the appropriate low momentum cut. The fraction of the collimator-produced events that remain in the sample have the

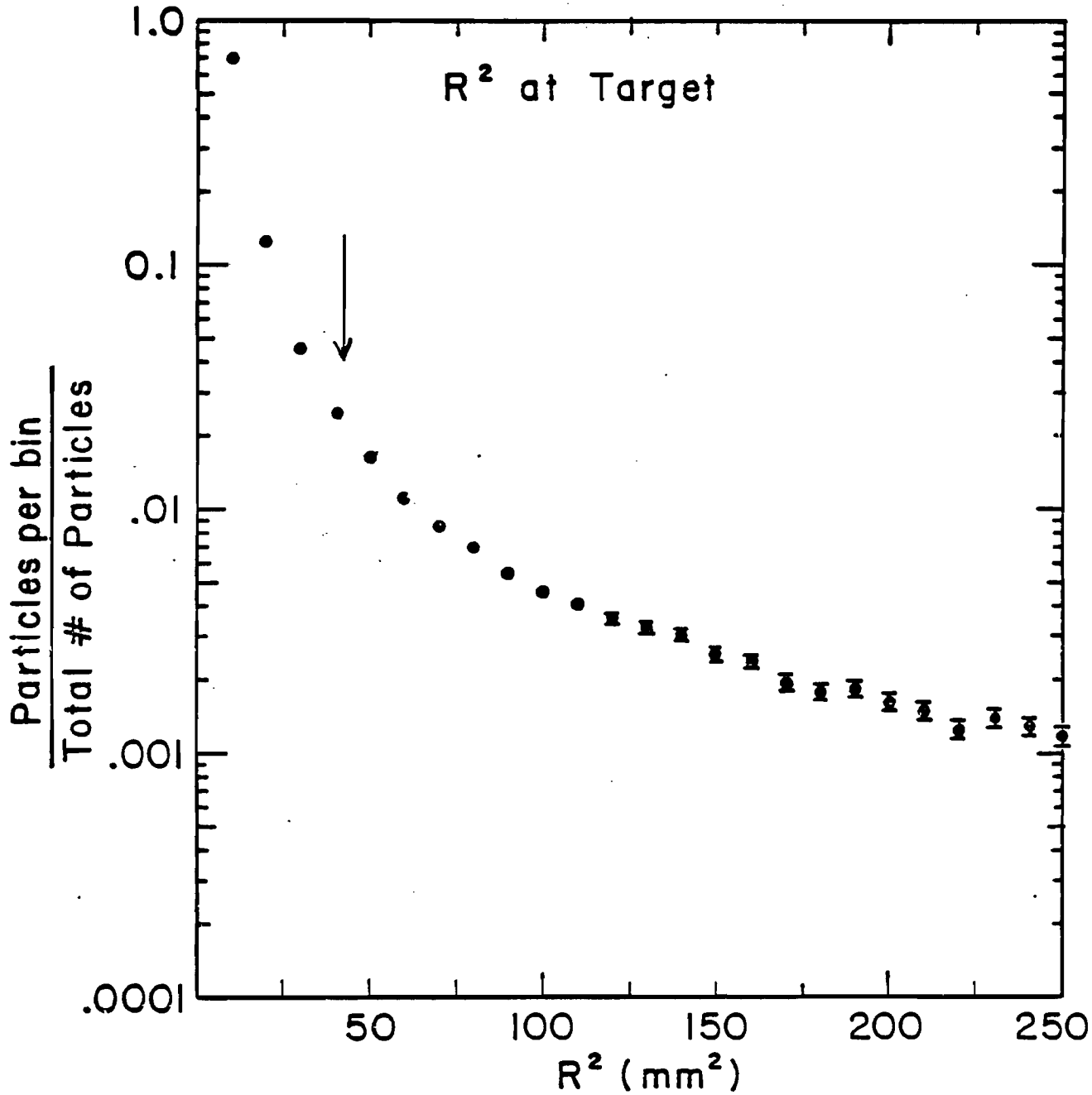


Figure 3.18 $R^2$ distribution for 5 mr $\Xi$'s (all momenta). The arrow indicates where the data was cut.

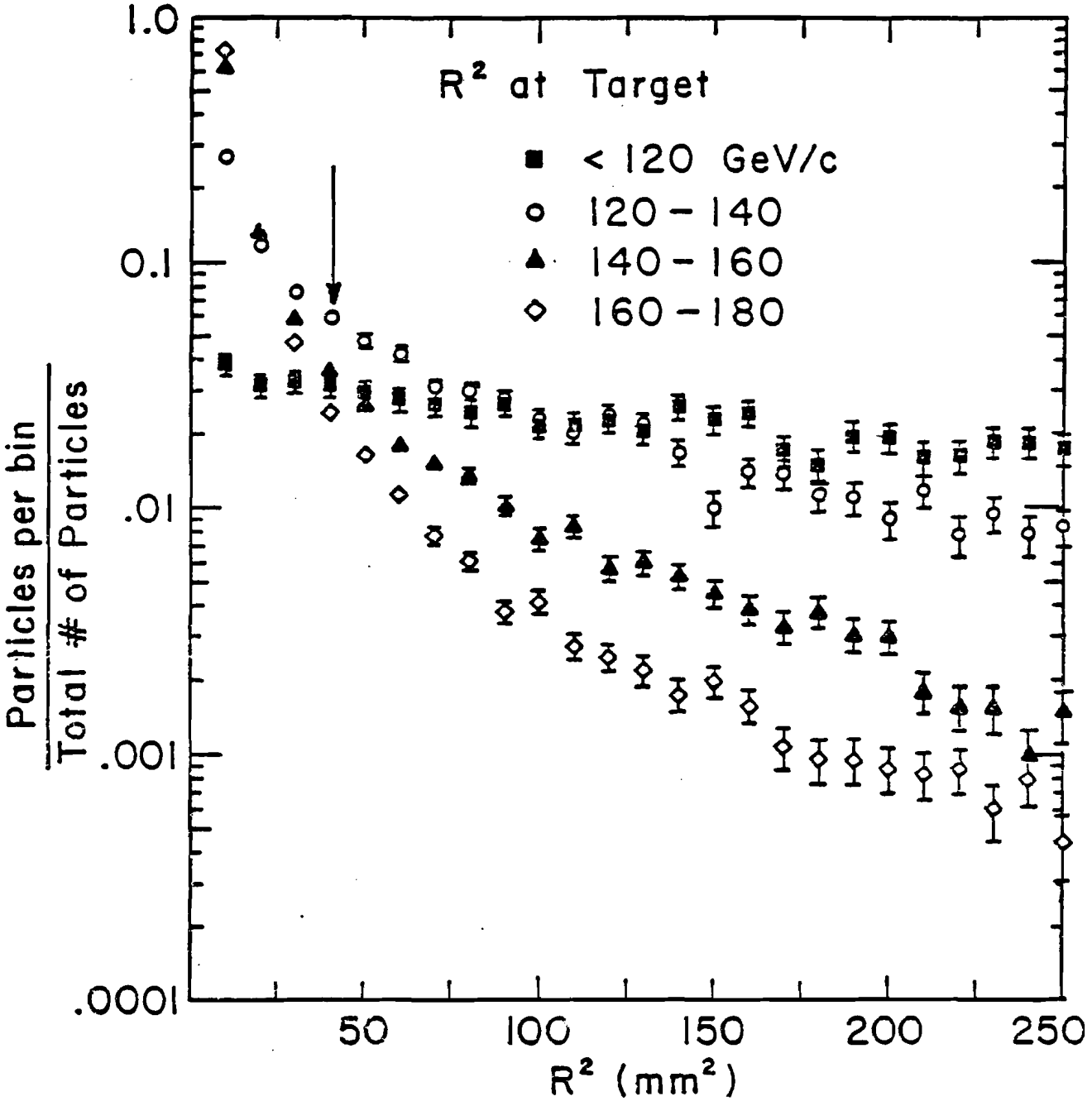


Figure 3.19 $R^2$ distributions as a function of momentum. The arrow indicates where the data was cut.

feature that their spin only precessed through approximately 75% of the field. The affect of this on the final answer is negligible, since it makes less than a 1% difference in the precession angle.

# CHAPTER 4

## The Polarization Analysis

### 4.1 General Analysis of Asymmetries

In the two body decay of unpolarized or spinless particles the angular distribution of the daughter particles is isotropic. However, both the $\Xi^-$ and $\Lambda$ are spin 1/2 baryons which decay into a spin 1/2 baryon and spin 0 meson. In this type of weak, parity-violating decay, an asymmetry in the angular distribution of the daughter baryons is observed. In particular,

$$dn/d\Omega = 1/4\ \pi\ (1 + \alpha\ \vec{P} \cdot \hat{p}) \qquad (4.1)$$

where $\hat{p}$ is a unit vector along the daughter baryon momentum direction in the parent rest frame. $\vec{P}$ is the parent

polarization and $\alpha$ is the inherent asymmetry in the decay. For decay angles $\theta$ and $\phi$ measured in polar coordinates with respect to the polarization vector, the decay is isotropic in $\phi$ and linear in $\cos\theta$.

Components of the parent polarization along each of the spatial axis x,y, and z, defined in the parent rest system, and parallel to the spectrometer axes, can be measured. This is done by looking at the projection of the daughter momentum vector along a particular axis. The angular distribution in $\cos\theta$ can be written in component form

$$dn/d(\cos\theta_i) = 1/2\ (1 + \alpha P_i \cos\theta_i) \qquad (4.2)$$

$\cos\theta_i = p_i/|\vec{p}|$, $|\vec{p}|$ = the magnitude of the momentum of the daughter baryon. This equation includes the assumption that each component of polarization is independent. This is exactly true only if the acceptance in $\phi$ is uniform. In this experiment this assumption has been made. For perfect acceptance in $\cos\theta$, Eq. 4.2 is a straight line with slope $\alpha P_i/2$. Thus, if $\alpha$ is known, $P_i$ can be determined.

Since the acceptance in $\cos\theta$ is not perfect, the measured asymmetry is Eq. 4.2 modified by an acceptance function $\varepsilon$

$$dn/d(\cos\theta) = \varepsilon/2\ (1 + \alpha P \cos\theta)$$

The direction of the polarization at production is constrained by parity to be either parallel or anti-parallel to

$$\hat{n} = \vec{p}_{in} \times \vec{p}_{out} / |\vec{p}_{in} \times \vec{p}_{out}|$$

i.e. normal to the production plane. By reversing the incident angle of the proton beam the direction of the initial polarization is reversed. This procedure changes the sign of the polarization but not its magnitude. For the two production angles, the asymmetries can be written

$$A_+ = \varepsilon(\cos\theta)(1 + \alpha P \cos\theta)$$

and

$$A_- = \varepsilon(\cos\theta)(1 - \alpha P \cos\theta)$$

where $\varepsilon(\cos\theta)$ is the acceptance function. If the acceptance is the same for both angles, a plot of the ratio

$$R = (A_+ - A_-) / (A_+ + A_-)$$

versus $\cos\theta$ has a slope which measures $\alpha P/2$. However, if the acceptance is not the same, this is not valid, and a direct measure of $\varepsilon_+$ and $\varepsilon_-$ is necessary.

An example of how the acceptance changes with production angle is seen in the $\theta y$ disribution of the $\Xi^-$ beam. ($\theta y$ is the angle with respect to the z axis in the y-z plane.) It is found that the centroids of this beam differ by approximately 1 mrad at the production target, as can be seen in Fig. 4.1. This propagates to a separation of nearly 4 cm at the most downstream chamber. Though this difference

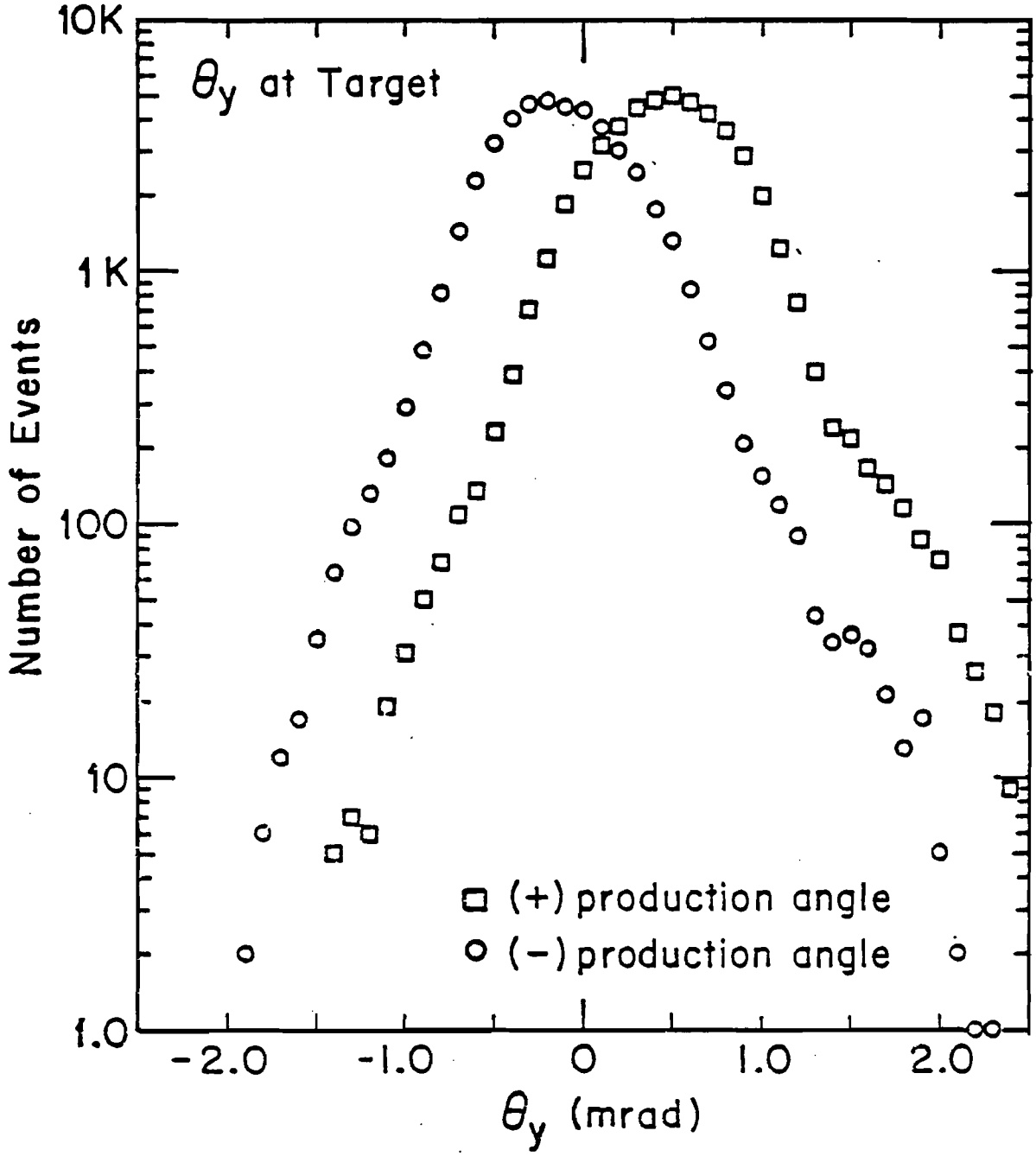


Figure 4.1 $\theta_y$ distribution for positive and negative production angles. $\theta y = py/pz$.

seems small, it implies that the two beams probe different parts of the apparatus, particularly at the limiting aperture, the 20 cm dimension of the analyzing magnet. The consequence of this is that, independent of any polarization, the two production angles will have different angular distributions due to the different acceptance.

To avoid this problem, the polarization analysis in this experiment was done using a hybrid Monte Carlo technique which determined $\varepsilon(\cos\theta)$ for each of the production angles, and also determined the asymmetry in the data due to the polarization.[24] This was done by generating MC events from the phase space of the real events. MC events were generated with the same parameters as the real events except $\cos\theta$, which was chosen randomly between -1 and +1. The MC event was required to be accepted by a software model of the apparatus. Those hybrid MC events, which passed all acceptance cuts, essentially mapped the $\cos\theta$ acceptance of the apparatus. The $\cos\theta$ distribution of these events was compared with the $\cos\theta$ distribution of the real events. Each HMC events was then weighted by a factor

$$W_{ij} = \frac{1 + A\cos\theta_{ij}}{1 + A\cos\theta_i}$$

where j is the index of the Monte Carlo event and i is the index of the real event from which the MC event was

generated. The asymmetry A, is varied to get the best agreement between the distribution of the real and HMC events. Details of this procedure are described in Appendix B.

In addition to the acceptance, unknown inefficiencies in a piece of apparatus, or parameters which are not well measured introduce systematic errors into a polarization measurement. These effects are called the "bias" in the measurement. Since the method of analysis used in this experiment provides an independent measurement of the total asymmetry at each production angle, what is measured includes the real polarization, P, as well as this bias.

However, since biases are a function of the detection apparatus they do not change sign when the production angle is reversed. Thus

$$A_+ = P_+ + B_+$$

and for the negative angle

$$A_- = P_- + B_-$$

Assuming $P_+ = -P_-$, and $B_+ = B_-$, subtracting the two asymmetries measures the physical polarization, while adding them gives a direct measure of the biases. In a polarization experiment one endeavors to maximize the ratio of "signal to noise" by minimizing the biases.

For each data set analyzed the x, y and z asymmetries were obtained for both the positive and negative production angle data. Figs. 4.2-4.4 show the measured asymmetries for + and - 5 mrad (6.6 T-m) as a function of momentum. The sign reversal of the polarization is apparent in the x asymmetry. Note that these asymmetries are those obtained before final kinematic constraints were required on the $\Xi$'s.

## 4.2 Daughter Lambda Analysis

Daughter $\Lambda$'s from $\Xi$'s are polarized according to the expression :

$$\vec{P}_{\Lambda} = \frac{(\alpha_{\Xi} + \hat{\Lambda}\cdot\vec{P}_{\Xi}) - \beta_{\Xi}(\hat{\Lambda}x\vec{P}_{\Xi}) - \gamma_{\Xi}\hat{\Lambda}x\,(\hat{\Lambda}x\vec{P}_{\Xi})}{1 + \alpha_{\Xi}\hat{\Lambda}\cdot\vec{P}_{\Xi}} \qquad (4.3)$$

where $\vec{P}_{\Lambda}$ and $\vec{P}_{\Xi}$ are the $\Lambda$ and $\Xi$ polarization vectors. $\hat{\Lambda}$ is the unit vector of the $\Lambda$ momentum direction, measured in the $\Xi$ rest frame. $\alpha$ , $\beta$ and $\gamma$ are the decay parameters which relate the real and imaginary part of the final state wave function for the decay products. They satisfy the relation

$$\alpha^2 + \beta^2 + \gamma^2 = 1$$

Thus the $\Xi$ polarization depends on both the decay asymmetry of the $\Xi$ and the polarization of the $\Xi$. While this expression is quite formidable it can be simplified. Assuming time reversal invariance ( $\beta = 0$) and rearranging the cross product, the expression can also be written

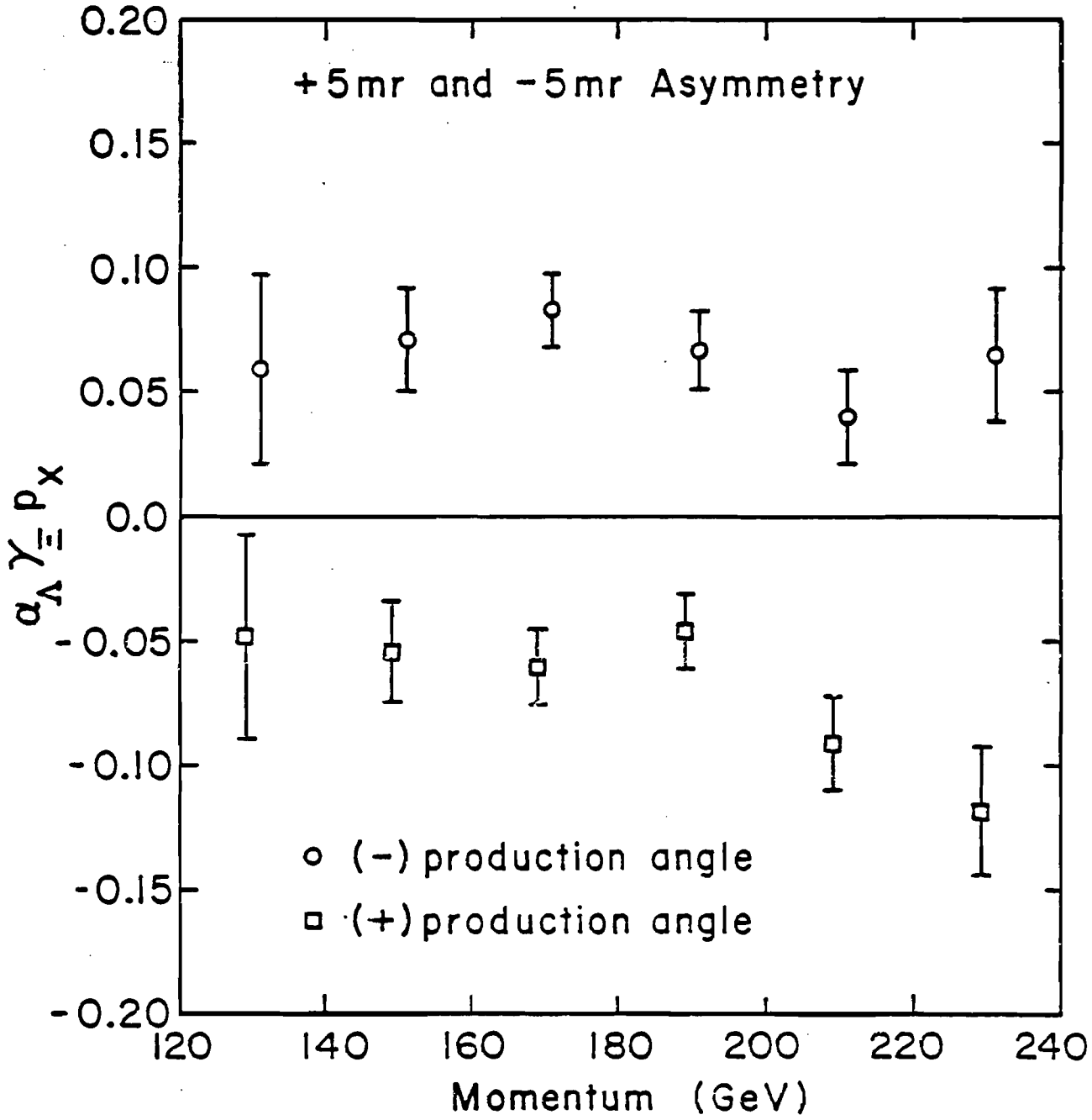


Figure 4.2 Measured x asymmetries for both positive and and negative production angles. No kinematic cuts have been applied to the sample.

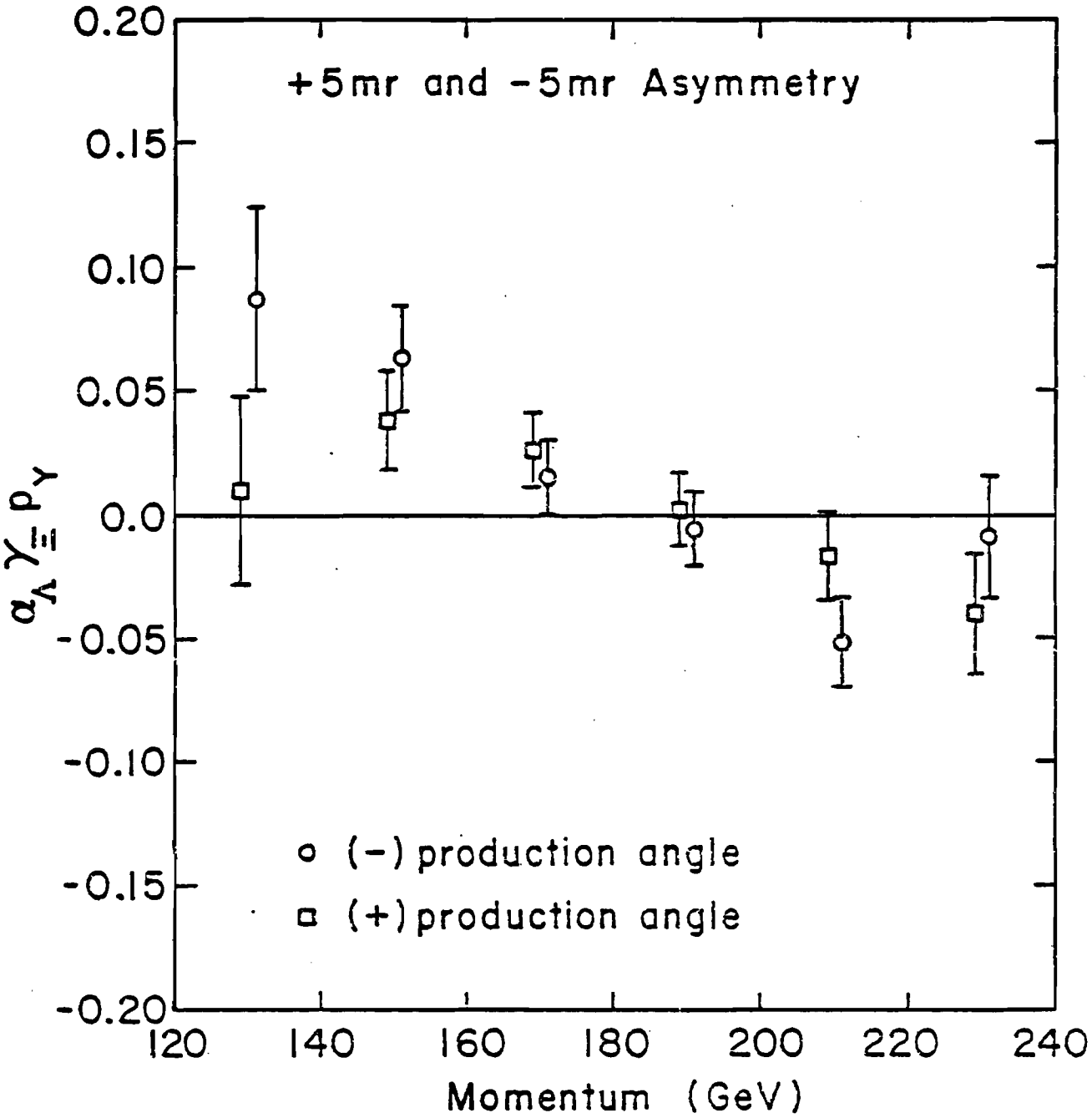


Figure 4.3 Measured y asymmetries for both positive and and negative production angles. No kinematic cuts have been applied to the sample.

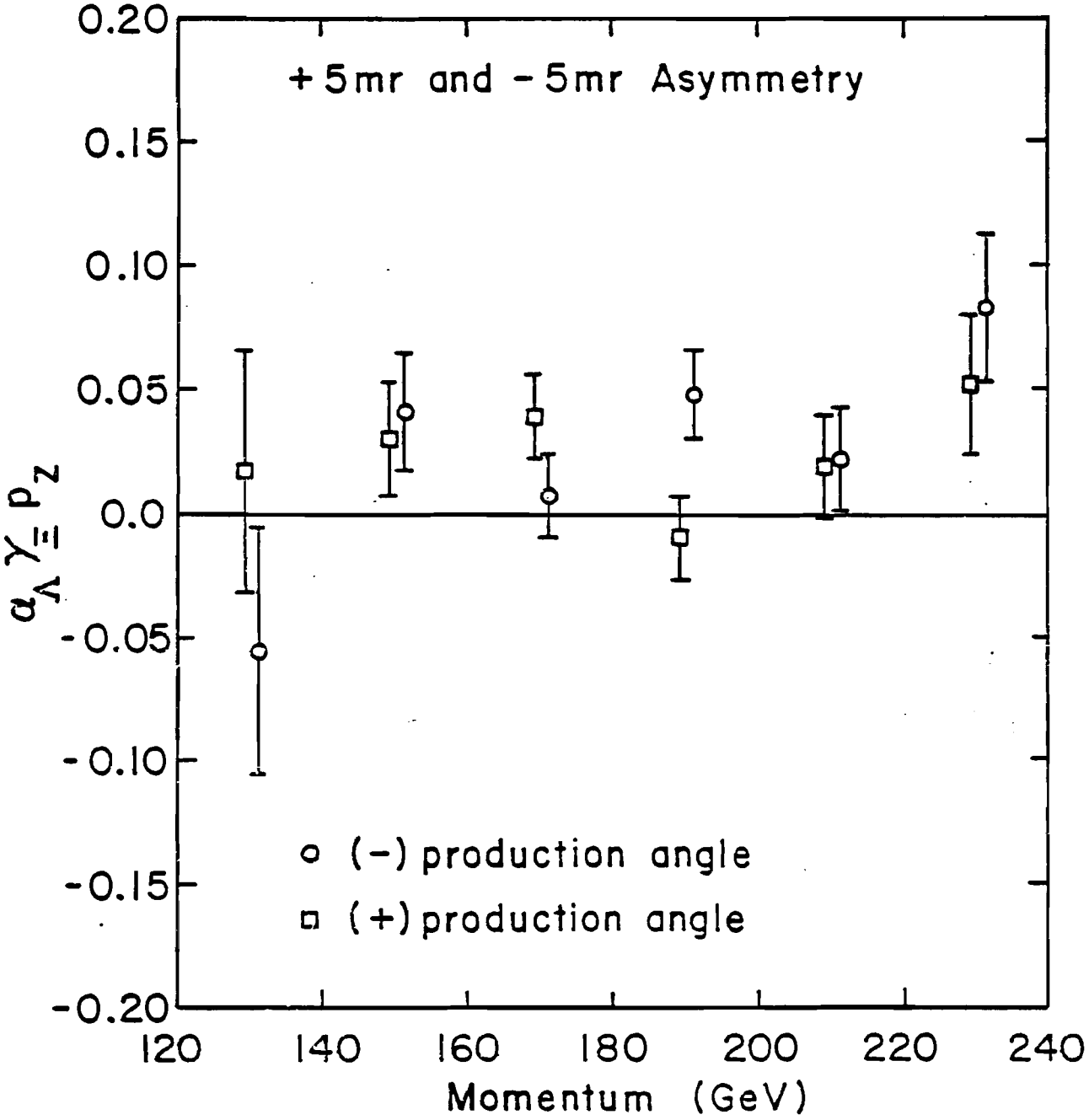


Figure 4.4 Measured z asymmetries for both positive and and negative production angles. No kinematic cuts have been applied to the sample.

$$\vec{P}_\Lambda = \frac{\alpha_\Xi \hat{\Lambda} + \{(1-\gamma_\Xi)\hat{\Lambda}\cdot\vec{P}_\Xi\}\hat{\Lambda} + \gamma_\Xi \vec{P}_\Xi}{1 + \alpha_\Xi \Lambda \cdot \vec{P}_\Xi} \tag{4.4}$$

While $\vec{P}_\Xi$ is event independent, $\hat{\Lambda}$ is not, but can be calculated for each event. If the spectrometer acceptance for $\Lambda$'s were 100%, the $\hat{\Lambda}$ terms would average to zero. In practice, the average values of $\hat{\Lambda} \cdot \hat{x}$ and $\hat{\Lambda} \cdot \hat{y}$ are small. The average value of $\hat{\Lambda} \cdot \hat{z}$ is larger. In general, it is a function of momentum but independent of production angle. The average values of the $\Lambda$ projection along the x, y and z axes are shown quantitatively in Table 4.1.

Using these average values and considering that $\alpha_\Xi \cong 0.47$, $\gamma_\Xi \cong 0.88$, and the measured asymmetries for $\vec{P}_\Xi \cong 0.10$, the contributions of the second terms in both the numerator and the denominator are small (~0.002 and 0.009) compared to the dominant terms $\gamma_\Xi \vec{P}_\Xi$ and 1. The term $\alpha_\Xi \hat{\Lambda}$ can be considered a contibution to the overall bias, and if not included in the calculation will subtract from the polarization measurment. However, it was retained and calculated in the present analysis. Thus to a good approximation Equation 4 4 can be reduced to

$$\vec{P}_\Lambda = \alpha \hat{\Lambda} + \gamma_\Xi \vec{P}_\Xi \tag{4.5}$$

There is one peculiarity about Equations 4.3-4.5 which

| Momentum (GeV/c) | $\langle\hat{\Lambda}\cdot\hat{x}\rangle$ | $\langle\hat{\Lambda}\cdot\hat{y}\rangle$ | $\langle\hat{\Lambda}\cdot\hat{z}\rangle$ |
|---|---|---|---|
| | Positive Production Angle | | |
| 135 | +0.112 | -0.003 | -0.270 |
| 152 | +0.062 | +0.019 | -0.216 |
| 170 | +0.026 | +0.017 | -0.145 |
| 189 | +0.015 | +0.010 | -0.140 |
| 209 | -0.005 | +0.021 | -0.061 |
| 229 | +0.014 | +0.022 | -0.054 |
| 256 | +0.007 | +0.011 | -0.035 |
| | Negative Production Angle | | |
| 135 | +0.040 | -0.026 | -0.284 |
| 152 | +0.045 | -0.029 | -0.217 |
| 170 | +0.002 | -0.041 | -0.154 |
| 189 | -0.009 | -0.036 | -0.103 |
| 209 | -0.009 | -0.043 | -0.075 |
| 229 | -0.035 | -0.036 | -0.066 |
| 256 | -0.047 | -0.043 | -0.027 |

Table 4.1 Average values of $\hat{\Lambda}\cdot\hat{x}$, $\hat{\Lambda}\cdot\hat{y}$ and $\hat{\Lambda}\cdot\hat{z}$ as a function of momentum for both positive and negative production angle.

should be noted. A polarization vector, like spin, only has a simple three-vector interpretation when measured in the rest system of the particle. Thus the left hand sides of these equations are measured in the $\Lambda$ rest frame, while quantities on the right hand sides are in the $\Xi$ rest frame. The relationship of these vectors is illustrated in Fig. 4.5.

In order to be relativistically correct, the proton direction in the $\Lambda$ rest frame should be obtained by transforming the proton from the laboratory to the $\Xi$ rest frame and then to the $\Lambda$ rest frame. This was the procedure followed in the analysis, although the difference between this procedure and a direct Lorentz transformation from the laboratory to the $\Lambda$ rest frame is at most a few degrees.

## 4.3 The Alpha Parameter

Using Equation 4.3, $\alpha_\Xi$ can be measured. For an unpolarized sample of cascades

$$\vec{P}_\Lambda = \alpha_\Xi \hat{\Lambda}$$

This says that the daughter $\Lambda$'s are polarized along the $\Lambda$ momentum direction with a magnitude $\alpha_\Xi$. The angular distribution of protons is given by

$$dn/d(\cos\theta) = 1/2\ (1 + \alpha_\Lambda \alpha_\Xi \cos\theta) \qquad (4.6)$$

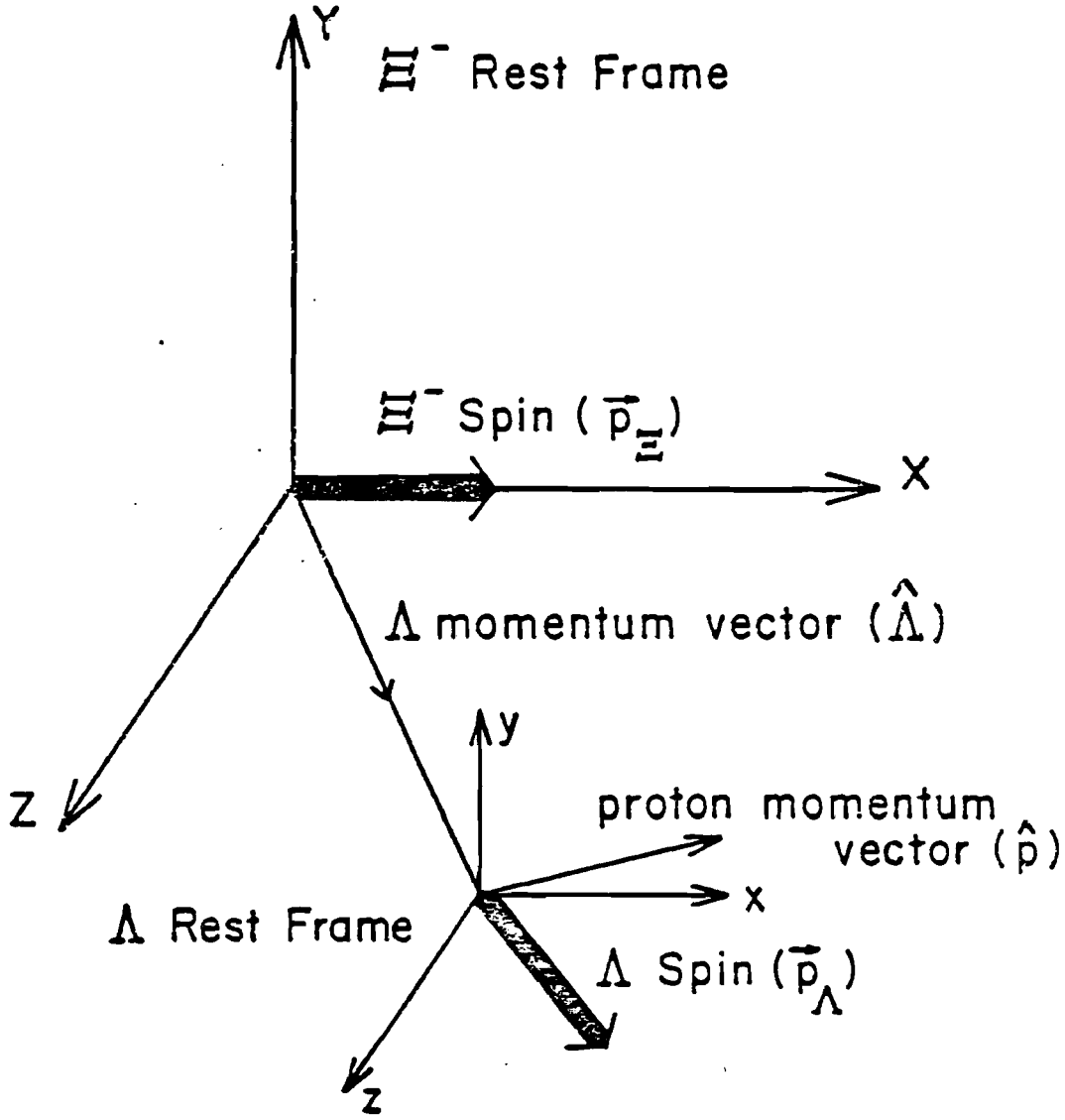


Figure 4.5 Relationship between vectors in the $\Xi^-$ and $\Lambda$ rest frames.

where cos 0 is the angle between $\vec{P}_\Lambda$ and the proton direction in the $\Lambda$ rest frame. Thus a measurement of the proton asymmetry gives a direct measure of the quantity $\alpha_\Lambda\alpha_\Xi$. $\alpha_\Xi$ is extracted by using the measured value of $\alpha_\Lambda$. Perfect $\Lambda$ acceptance implies that the value of $\alpha_\Lambda\alpha_\Xi$ can be measured directly from the slope of the cos $\theta$ distribution given by Eq. 4.6. To correct for the acceptance, the data was analyzed using the hybrid MC method. The weight for the hybrid MC events was given by

$$W_{ij} = (1 + \alpha_\Lambda\alpha_\Xi \cos\theta_{ij}) / (1 + \alpha_\Lambda\alpha_\Xi \cos\theta_i)$$

Comparisons of cos $\theta$ distributions for real events and hybrid MC events, before and after the MC events are weighted by the determined asymmetry are shown in Figs. 4.6.

In practice the measurement is not so straightforward. In this experiment, an unpolarized sample of $\Xi^-$'s was obtained by combining equal amounts of data taken at opposite production angles. Unlike in the polarization analysis, the bias cancellation does not apply. Instead a bias in the sample appears as a false $\Lambda$ asymmetry. Thus the observed $\Lambda$ polarization can be written

$$\vec{P}_\Lambda(\text{observed}) = \vec{P}_\Lambda(\text{true}) + \vec{B}_\Lambda$$

Now

$$\alpha_\Lambda \vec{P}_\Lambda\cdot\hat{\Lambda}(\text{observed}) = \alpha_\Lambda\alpha_\Xi \ (\text{true}) + \alpha_\Lambda\vec{B}_\Lambda\cdot\hat{\Lambda}$$

and $\alpha_\Lambda \vec{B}_\Lambda\cdot\hat{\Lambda}$ should be subtracted from the observed asymmetry of the proton distribution in order to determine $\alpha_\Lambda\alpha_\Xi$. The

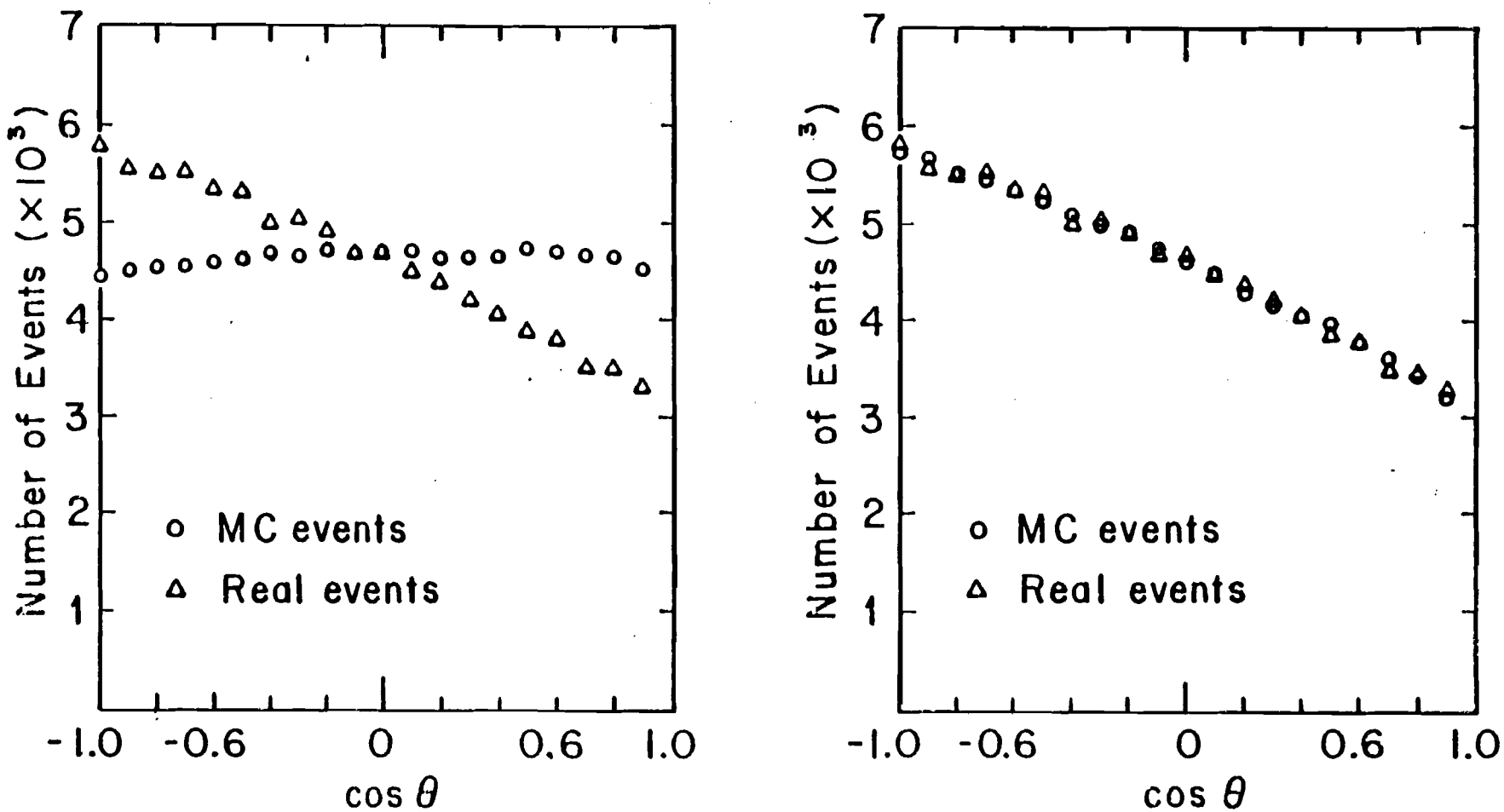


Figure 4.6 Cos θ comparisons for real and hybrid MC events. θ is the angle between the Λ direction, $\hat{\Lambda}$, (= $-\hat{\Xi}$) and the proton direction, $\hat{p}$, measured in the Λ rest frame. The MC events on the left were generated with $\alpha_\Lambda \alpha_\Xi = 0$. On the right they have been weighted by the asymmetry $\alpha_\Lambda \alpha_\Xi = -0.303$. The $\chi^2$ agreement for this distribution is 1.017/df.

magnitude of this correction depends on the size of $B_\Lambda$, which is determined from the polarization analysis using Eq. 4.5. The application of this correction is discussed in Sec. 4.6.

## 4.4 First Iteration Polarization Analysis

Using a first value of $\alpha_\Lambda \alpha_\Xi$ obtained by the simple combination of + and - data, and Eq. 4.6, Eq. 4.5 was used to measure the $\Xi$ polarization for each of the production angles. The polarization was measured along a set of x, y and z axes parallel to the lab axes, for which the z axis was along the direction of the nominal channel momentum.

The weight factor for the hybrid Monte Carlo events was given by

$$W = \frac{1 + (\alpha_\Lambda \alpha_\Xi \hat{\Lambda}\cdot\hat{n} + \hat{A}_\pm \cdot \hat{n}) \cos\theta_{ij}}{1 + (\alpha_\Lambda \alpha_\Xi \hat{\Lambda}\cdot\hat{n} + \hat{A}_\pm \cdot \hat{n}) \cos\theta_i}$$

This was expanded as a power series in $A_\pm$, where $A_\pm$ was the asymmetry measured at each of the production angles. Since the total asymmetry was the sum of the polarization plus the bias, $\alpha_\Lambda \gamma_\Xi \vec{P}_\Xi$ was obtained by subtraction of the positive and negative asymmetries. The sum of the two asymmetries gave a measure of the bias term $\alpha_\Lambda \vec{B}_\Lambda$.

## 4.5 Polarization and Bias Fit

Since the biases were functions only of momentum, they could be determined from the entire data sample and then used to correct $\alpha_\Lambda \alpha_\Xi$. This was done by minimizing a $\chi^2$ function in which all the measured asymmetries and corresponding uncertainties for each data set were the input parameters. The data were constrained to have a precession angle, $\phi_j$, in the magnetic field, which was a function of the field integral; a polarization magnitude, $P_o$, which was a function only of production angle and momentum; and biases, $Bx_i$ and $Bz_i$, which were functions only of momentum.

$$\chi^2 = \sum_{ijk} \frac{(A_{xijk} - B_{xi} \pm P_{oi} \cos\phi_j)^2}{\sigma_{xijk}^2} + \frac{(A_{zijk} - B_{zi} \pm P_{oi} \sin\phi_j)^2}{\sigma_{zijk}^2}$$

where i runs over seven momentum bins, j over two field integrals and k over production angle + and -. The polarization $P_{oi}$, changes sign with production angle. The upper sign in the $\chi^2$ refers to the + production angle. $Ax_{ijk}$, $Az_{ijk}$, $\sigma_{xijk}$, and $\sigma_{zijk}$ are the data points and errors which are input. The two precession angles, $\phi_j$ are related to a single parameter of the fit, g/2 - 1, through Eq. 1.3. This procedure gives a direct measure of the magnetic moment which is consistant with all running conditions of the

experiment. The results of this fit are given in Table 4.2. Using the results of the fit, the contibution to the $\chi^2$ for each of the data points was determined. The distribution of these $\chi^2$'s are shown in Fig.4.7.

## 4.6 Second Iteration Analysis

Using the biases and the polarizations obtained from the $\chi^2$ fit, Equation 4.3 was used to obtain a better measurement of $\alpha_\Lambda\alpha_\Xi$ . The expression used was

$$\vec{P}_\Lambda\cdot\hat{\Lambda} = \frac{(\alpha_\Xi + \hat{\Lambda}\cdot\vec{P}_\Xi)}{1 + \alpha_\Xi\hat{\Lambda}\cdot\vec{P}_\Xi} + \vec{B}_\Lambda\cdot\hat{\Lambda}$$

Since the biases and the $\Lambda$ acceptance were momentum dependent, the correction term to $\alpha_\Lambda\alpha_\Xi$ was also momentum dependent. However, overall, the correction was small and generally less than the statistical error. The results of both the first and second iteration fits are given in Sec. 5.2.

Using the second iteration value of $\alpha_\Lambda\alpha_\Xi$ and polarization components determined from the fit, the polarization analysis was also studied using

$$\vec{P}_\Lambda = \frac{\alpha_\Xi\Lambda + \gamma_\Xi\vec{P}_\Xi + (\vec{P}_\Xi)_\perp\cdot\Lambda(1-\gamma_\Xi)}{1 + \alpha_\Xi(\vec{P}_\Xi)_\perp\cdot\hat{\Lambda}}$$

| Momentum | $p_t$ | $x_f$ | Po (5 mrad) |
|---|---|---|---|
| 115 | 0.58 | 0.29 | -0.130±0.095 |
| 133 | 0.67 | 0.33 | -0.027±0.031 |
| 151 | 0.76 | 0.38 | -0.058±0.018 |
| 170 | 0.85 | 0.43 | -0.102±0.014 |
| 189 | 0.95 | 0.48 | -0.097±0.015 |
| 209 | 1.05 | 0.52 | -0.107±0.018 |
| 242 | 1.21 | 0.61 | -0.128±0.020 |

| Momentum | $p_t$ | $x_f$ | Po (7.5 mrad) |
|---|---|---|---|
| 115 | 0.86 | 0.29 | -0.047±0.078 |
| 131 | 0.98 | 0.33 | -0.075±0.034 |
| 150 | 1.13 | 0.38 | -0.112±0.029 |
| 169 | 1.27 | 0.42 | -0.091±0.034 |
| 189 | 1.42 | 0.47 | -0.132±0.049 |
| 209 | 1.55 | 0.52 | -0.098±0.075 |
| 231 | 1.73 | 0.58 | -0.127±0.128 |

| Momentum | x-bias | z-bias |
|---|---|---|
| 115 | +0.039±0.038 | -0.015±0.059 |
| 133 | +0.020±0.014 | -0.035±0.018 |
| 151 | +0.027±0.009 | +0.004±0.010 |
| 170 | +0.019±0.008 | +0.017±0.009 |
| 189 | +0.017±0.009 | +0.022±0.009 |
| 209 | +0.012±0.011 | +0.058±0.012 |
| 239 | -0.008±0.012 | +0.085±0.013 |

$g/2 - 1 = -0.003 \pm 0.055$

$\chi^2 = 105.3$

$\chi^2/df = 1.02$

Table 4.2 Results of Master $\chi^2$ Fit
Polarization is shown as a function of transverse momentum, $p_t$, and Feynman x.

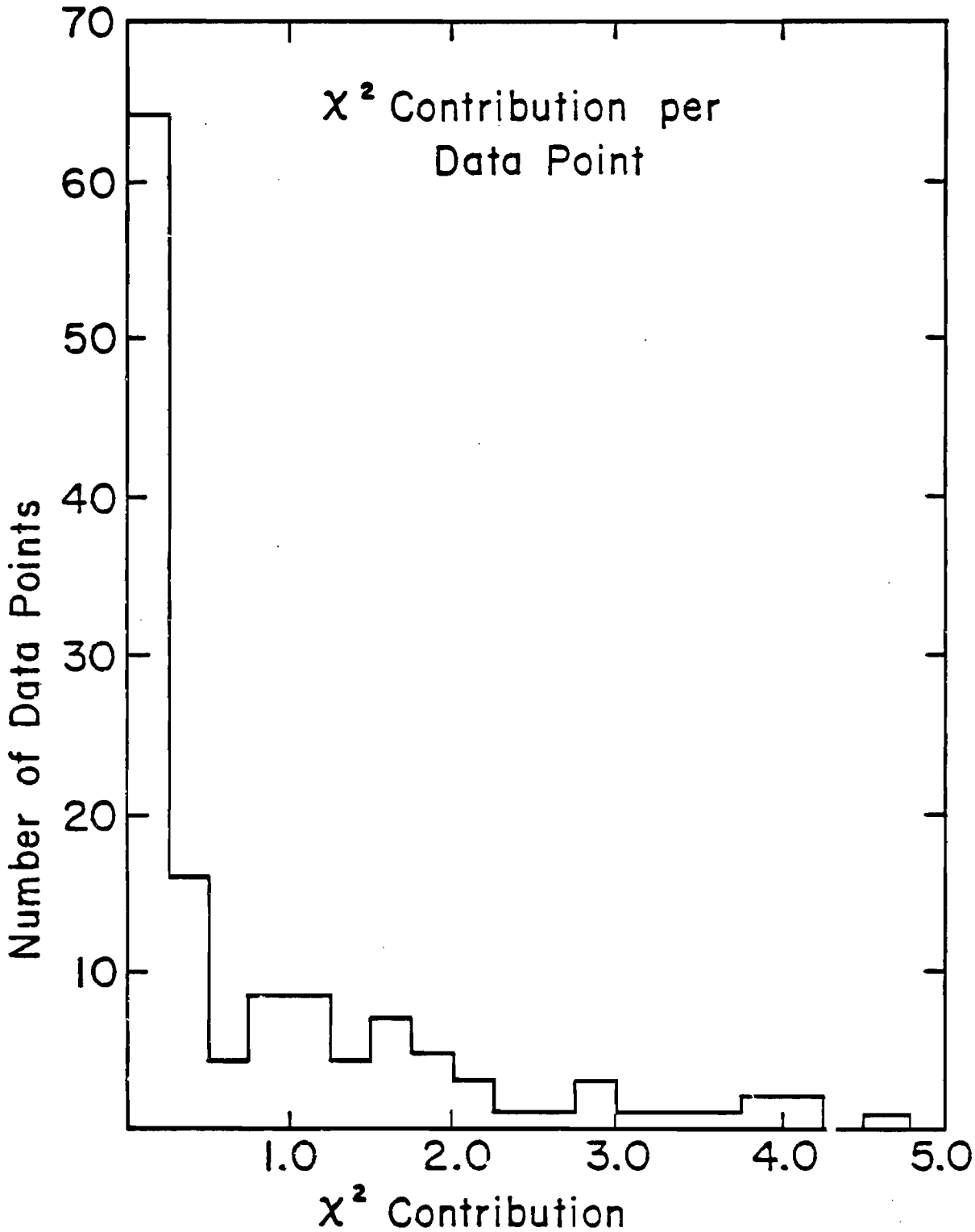


Figure 4.7 $\chi^2$ contibution for each data point to the master $\chi^2$ fit.

to verify the approximation Eq.4.5, where $(P_{\Xi})_1$ is the first iteration value. The change in the asymmetries in all cases was less than $0.3\sigma$. The polarization asymmetries given in Chapter 5 are those determined from Eq. 4.5.

## 4.7 Monte Carlo Analysis

In addition to using a Monte Carlo to study the apparatus acceptance and reconstruction efficieny it was also used to determine the dependability of the analysis programs. This study was done in several stages. First, unpolarized, isotropic events were generated and passed to the polarization analysis program. All measured asymmetries for these events were expected to be zero. This was indeed the case. The procedure was repeated for Monte Carlo events generated with asymmetry parameters $\alpha_{\Lambda}$ = 0.642 and $\alpha_{\Xi}$ = -0.46. Monte Carlo events from this sample which were reconstructed and passed all reconstruction cuts were then analyzed. Here it was found that the asymmetry measured by the $\alpha_{\Xi}$ analysis program differed from the input asymmetry by $-0.010\pm0.005$. This deviation was a measure of the bias introduced by the reconstruction program.

It was found that the biases in the Monte Carlo closely

matched the biases observed in the data. After detailed study of both the Monte Carlo and the data it was concluded that the data was relatively free of apparatus or trigger induced biases. The Monte Carlo $\alpha_{\Xi}$ analysis was iterated using the Monte Carlo measured reconstruction biases. After this procedure the measured asymmetry differed from the input asymmetry by less than $-0.003 \pm 0.005$. A sample of the MC biases is given in Table 4.3.

## 4.8 Systematic Errors in the Asymmetry Analysis

To insure that the results did not include signals due to the systematic effect of the cuts imposed on the data the results were also studied as a funtion of the various cuts. This was done in two ways. First, the results were looked at as a function of individual cuts. That is, the sample was only required to have satisfied the minimum criteria for a good event, $\chi^2 < 80$ and a vertex separation greater than zero. The momentum averaged signals were then examined as a function of the kinematic $\chi^2$ cut, $\Xi$ mass cut, z vertex cut and $R^2$ cut.

Secondly, the data were required to pass all the desired cuts except one and this one cut was varied to see if any correlation between cuts and signals could be observed.

The results of these studies showed that the polarization signal varied by less than 0.6 $\sigma$ over the range in which the cuts were varied while the biases were seen to increase as certain cuts were tightened. This was to be expected, since requirements on the kinematic $\chi^2$ and mass preferentially eliminate events from particular regions of the cos $\theta$ distribution. For example,for a data sample in which all cuts were required, including the kinematic $\chi^2$ cut at 20, the x polarization was $-0.0598 \pm 0.0062$. Tightening the cut to $\chi^2$ less than 8 changed the polarization signal to $-0.0611 \pm 0.0062$. The x bias, however, increased from $+0.0124+0.0062$ to $+0.0374 \pm 0.0063$. In z the signal changed from $+0.0042 \pm 0.0069$ to $-0.0003 \pm 0.0070$. The bias changed from $+0.0395 \pm 0.0069$ to $+0.0321 \pm 0.0070$. There was no change in the y asymmetry.

| Momentum | Bx | By | Bz |
|---|---|---|---|
| 127 | +0.062±0.030 | -0.001±0.030 | -0.024±0.037 |
| 152 | +0.000±0.021 | -0.042±0.021 | +0.026±0.023 |
| 171 | +0.003±0.015 | +0.005±0.014 | +0.026±0.016 |
| 190 | -0.007±0.013 | -0.003±0.013 | +0.033±0.014 |
| 209 | -0.007±0.015 | +0.015±0.014 | +0.065±0.015 |
| 229 | -0.031±0.019 | -0.012±0.018 | +0.046±0.019 |
| 256 | -0.006±0.025 | +0.029±0.023 | +0.110±0.027 |

Table 4.3 Monte Carlo Reconstruction Biases

# CHAPTER 5

# Results

## 5.1 Inclusive Polarization

The measured asymmetries for all sets of positive and negative production angles were combined in the manner described in Section 4.2. The momentum averaged signals and biases for the five data sets described in Section 2.7 are listed in Table 5.1.

For Sets 3-5 the polarizations and biases are plotted as functions of momentum in Figs. 5.1-5.15, and listed in Tables 5.2-5.4. The plots and figures for Sets 1&2 are given in Appendix C.

Since the initial polarization was constrained to point along the x direction and then precess, it was expected that the final polarization vector would lie in the x-z plane. The results reported here show no y polarization as expected. However the z component of the polarization is also consistent with zero. In x the signal is consistantly around $-0.06 \pm .01$

The magnitude of the polarization determined from the $\chi^2$ fit described in Section 4.5 is shown as a function of transverse momentum for both 5 and 7.5 mrad production angle in Fig. 5.16. It has been observedin both the $\Lambda$ and the $\Sigma^0$ hyperons that the polarization is a function of both transverse momentum ($p_t$ = momentum x production angle) and Feynman x, (x = momentum/400) since for a fixed $p_t$ the larger production angle has a smaller x.[4,9] In the data the low statistics on the 7.5 mrad data make it difficult to come to the same conclusion though there is a slight trend towards this effect.

Momentum Averaged Polarizations and Biases

| Set | n | Polarization | Bias |
|---|---|---|---|
| 1 | x | -0.0548±0.0160 | +0.0136±0.0160 |
| | y | -0.0073±0.0135 | -0.0144±0.0135 |
| | z | +0.0049±0.0158 | +0.0330±0.0158 |
| 2 | x | -0.0608±0.0112 | +0.0138±0.0112 |
| | y | +0.0075±0.0106 | -0.0250±0.0106 |
| | z | -0.0166±0.0122 | +0.0328±0.0122 |
| 3 | x | -0.0598±0.0062 | +0.0124±0.0062 |
| | y | -0.0011±0.0059 | +0.0104±0.0059 |
| | z | +0.0043±0.0069 | +0.0408±0.0069 |
| 4 | x | -0.0461±0.0084 | +0.0184±0.0084 |
| | y | -0.0028±0.0082 | -0.0326±0.0082 |
| | z | +0.0011±0.0095 | +0.0192±0.0095 |
| 5 | x | -0.0624±0.0100 | +0.0192±0.0100 |
| | y | +0.0048±0.0100 | -0.0009±0.0100 |
| | z | +0.0103±0.0116 | -0.0199±0.0116 |

Table 5.1 Momentum averaged signals and biases for the five data sets analyzed. These sets correspond to the sets listed in Table 2.1.

| P Bin | P | Pz | Px |
|---|---|---|---|
| 110-140 | 133 | +0.0856±0.0515 | -0.0517±0.0421 |
| 140-160 | 152 | -0.0123±0.0192 | -0.0510±0.0167 |
| 160-180 | 170 | +0.0211±0.0130 | -0.0657±0.0119 |
| 180-200 | 190 | -0.0153±0.0132 | -0.0497±0.0121 |
| 200-220 | 209 | +0.0200±0.0163 | -0.0637±0.0150 |
| 220-240 | 229 | -0.0120±0.0227 | -0.0859±0.0209 |
| 240-290 | 256 | +0.0050±0.0295 | -0.0667±0.0263 |

Polarization for 6.6 T-m field, 5.0 mr production angle

| | | | |
|---|---|---|---|
| 105-120 | 115 | +0.0571±0.0736 | -0.0770±0.0598 |
| 120-140 | 132 | +0.0173±0.0263 | -0.0125±0.0210 |
| 140-160 | 150 | +0.0129±0.0180 | -0.0141±0.0160 |
| 160-180 | 170 | -0.0036±0.0181 | -0.0547±0.0167 |
| 180-200 | 189 | -0.0180±0.0224 | -0.0856±0.0210 |
| 200-220 | 209 | +0.0071±0.0323 | -0.0982±0.0293 |
| 220-270 | 228 | -0.0340±0.0397 | -0.0351±0.0368 |

Polarization for 5.1 T-m field, 5.0 mr production angle

| | | | |
|---|---|---|---|
| 105-120 | 115 | +0.0385±0.0705 | -0.0304±0.0487 |
| 120-140 | 131 | +0.0281±0.0265 | -0.0461±0.0206 |
| 140-160 | 150 | +0.0246±0.0201 | -0.0685±0.0179 |
| 160-180 | 170 | +0.0031±0.0224 | -0.0559±0.0209 |
| 180-200 | 189 | -0.0256±0.0329 | -0.0796±0.0303 |
| 200-220 | 208 | -0.0242±0.0555 | -0.0599±0.0469 |
| 220-250 | 231 | -0.0547±0.0799 | -0.0774±0.0838 |

Polarization for 5.1 T-m field, 7.5 mr production angle

Table 5.2 Polarization results vs. momentum for the three running conditions (The 6.6 T-m, 5 mrad is only Set 3.)

| P Bin | P | Bz | Bx |
|---|---|---|---|
| 115-140 | 133 | -0.0053±0.0515 | +0.0027±0.0421 |
| 140-160 | 152 | +0.0447±0.0192 | +0.0191±0.0167 |
| 160-180 | 170 | +0.0262±0.0130 | +0.0261±0.0119 |
| 180-200 | 190 | +0.0296±0.0132 | +0.0302±0.0121 |
| 200-220 | 209 | +0.0365±0.0163 | -0.0013±0.0150 |
| 220-240 | 229 | +0.0863±0.0227 | -0.0036±0.0209 |
| 240-290 | 256 | +0.1130±0.0295 | -0.0705±0.0263 |

Biases for 6.6 T-m field, 5.0 mr production angle

| | | | |
|---|---|---|---|
| 105-120 | 115 | +0.0566±0.0736 | +0.0397±0.0598 |
| 120-140 | 132 | -0.0077±0.0263 | +0.0142±0.0210 |
| 140-160 | 150 | +0.0050±0.0180 | +0.0272±0.0160 |
| 160-180 | 170 | +0.0236±0.0181 | +0.0133±0.0167 |
| 180-200 | 189 | +0.0129±0.0224 | +0.0063±0.0210 |
| 200-220 | 209 | +0.0659±0.0323 | +0.0172±0.0293 |
| 220-270 | 236 | +0.0545±0.0397 | +0.0571±0.0368 |

Biases for 5.1 T-m field, 5.0 mr production angle

| | | | |
|---|---|---|---|
| 100-120 | 115 | -0.0809±0.0705 | +0.0360±0.0487 |
| 120-140 | 131 | -0.0806±0.0265 | +0.0332±0.0206 |
| 140-160 | 150 | -0.0197±0.0201 | +0.0104±0.0179 |
| 160-180 | 170 | -0.0267±0.0224 | +0.0262±0.0209 |
| 180-200 | 189 | +0.0071±0.0329 | -0.0128±0.0303 |
| 200-220 | 208 | +0.1377±0.0555 | -0.0003±0.0469 |
| 220-250 | 231 | +0.0299±0.0799 | +0.1082±0.0838 |

Biases for 5.1 T-m field, 7.5 mr production angle

Table 5.3 x and z biases as functions of momentum

| P Bin | P | "Py" | By |
|---|---|---|---|
| 125-140 | 135 | -0.0538±0.0428 | +0.1235±0.0428 |
| 140-160 | 152 | -0.0143±0.0167 | +0.0471±0.0167 |
| 160-180 | 170 | +0.0070±0.0117 | +0.0309±0.0117 |
| 180-200 | 190 | -0.0026±0.0114 | -0.0007±0.0114 |
| 200-220 | 209 | +0.0203±0.0141 | -0.0267±0.0141 |
| 220-240 | 229 | -0.0137±0.0190 | -0.0210±0.0190 |
| 240-290 | 256 | -0.0294±0.0241 | +0.0118±0.0241 |

Y asymmetries for 6.6 T-m field, 5.0 mr production angle

| | | | |
|---|---|---|---|
| 105-120 | 115 | -0.0686±0.0564 | +0.0142±0.0564 |
| 120-140 | 132 | -0.0155±0.0218 | -0.0118±0.0218 |
| 140-160 | 150 | -0.0072±0.0160 | -0.0279±0.0160 |
| 160-180 | 170 | +0.0103±0.0162 | -0.0473±0.0162 |
| 180-200 | 189 | -0.0002±0.0198 | -0.0204±0.0198 |
| 200-220 | 209 | +0.0055±0.0266 | -0.0100±0.0266 |
| 220-270 | 236 | -0.0128±0.0353 | -0.1152±0.0352 |

Y asymmetries for 5.1 T-m field, 5.0 mr production angle

| | | | |
|---|---|---|---|
| 105-120 | 115 | -0.0385±0.0487 | +0.0829±0.0487 |
| 120-140 | 131 | -0.0122±0.0211 | -0.0015±0.0211 |
| 140-160 | 150 | +0.0083±0.0178 | -0.0093±0.0178 |
| 160-180 | 170 | +0.0286±0.0209 | -0.0137±0.0209 |
| 180-200 | 189 | -0.0133±0.0287 | -0.0027±0.0287 |
| 200-220 | 209 | -0.0468±0.0440 | +0.0011±0.0440 |
| 220-250 | 231 | +0.0966±0.0694 | +0.0350±0.0694 |

Y asymmetries for 5.1 T-m field, 7.5 mr production angle

Table 5.4 Parity violating y polarizations and biases as functions of momentum

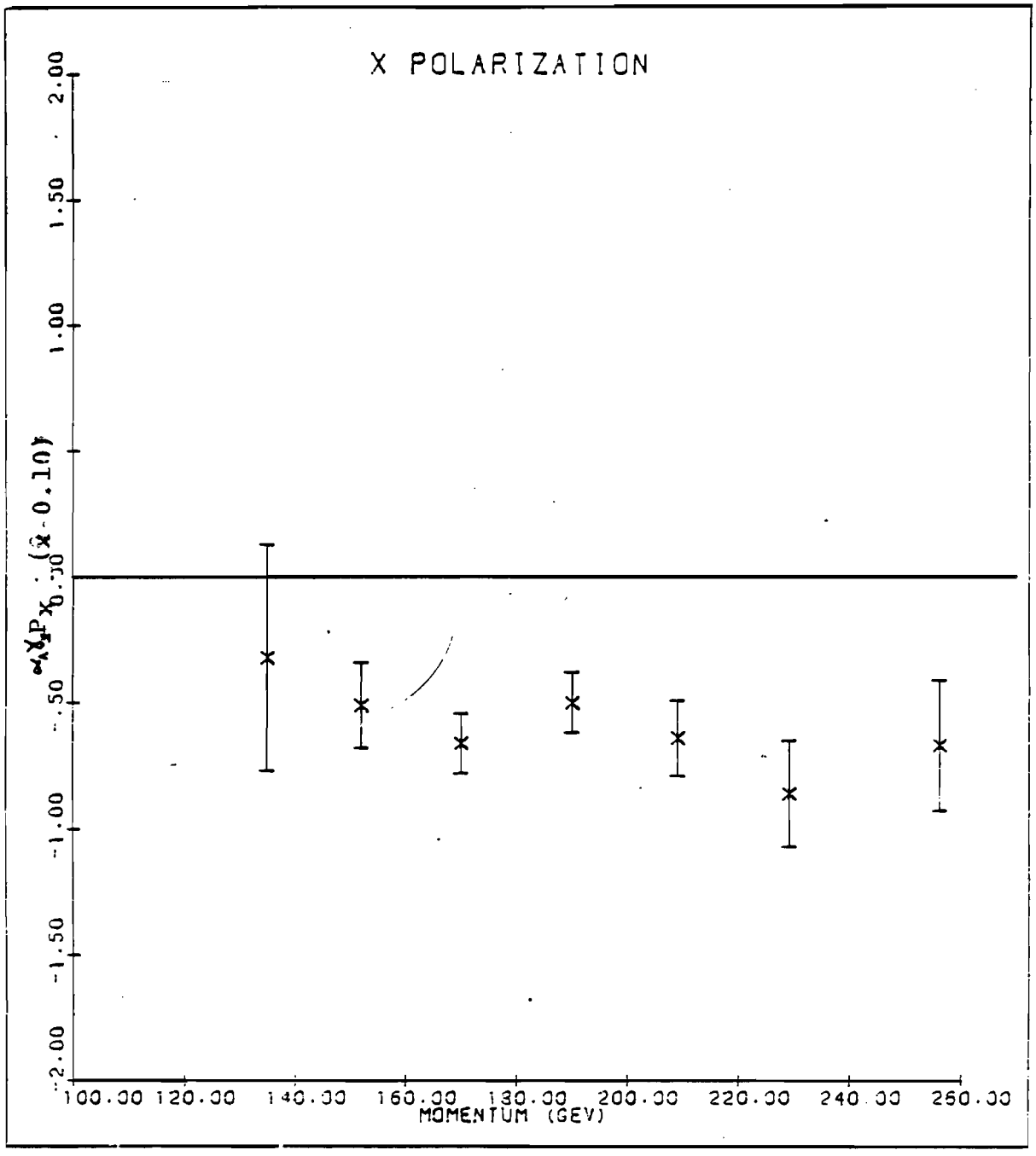


Figure 5.1 $\alpha_\Lambda \gamma_\Xi P_x$ vs. momentum
5 mrad, 6.6 T-m field

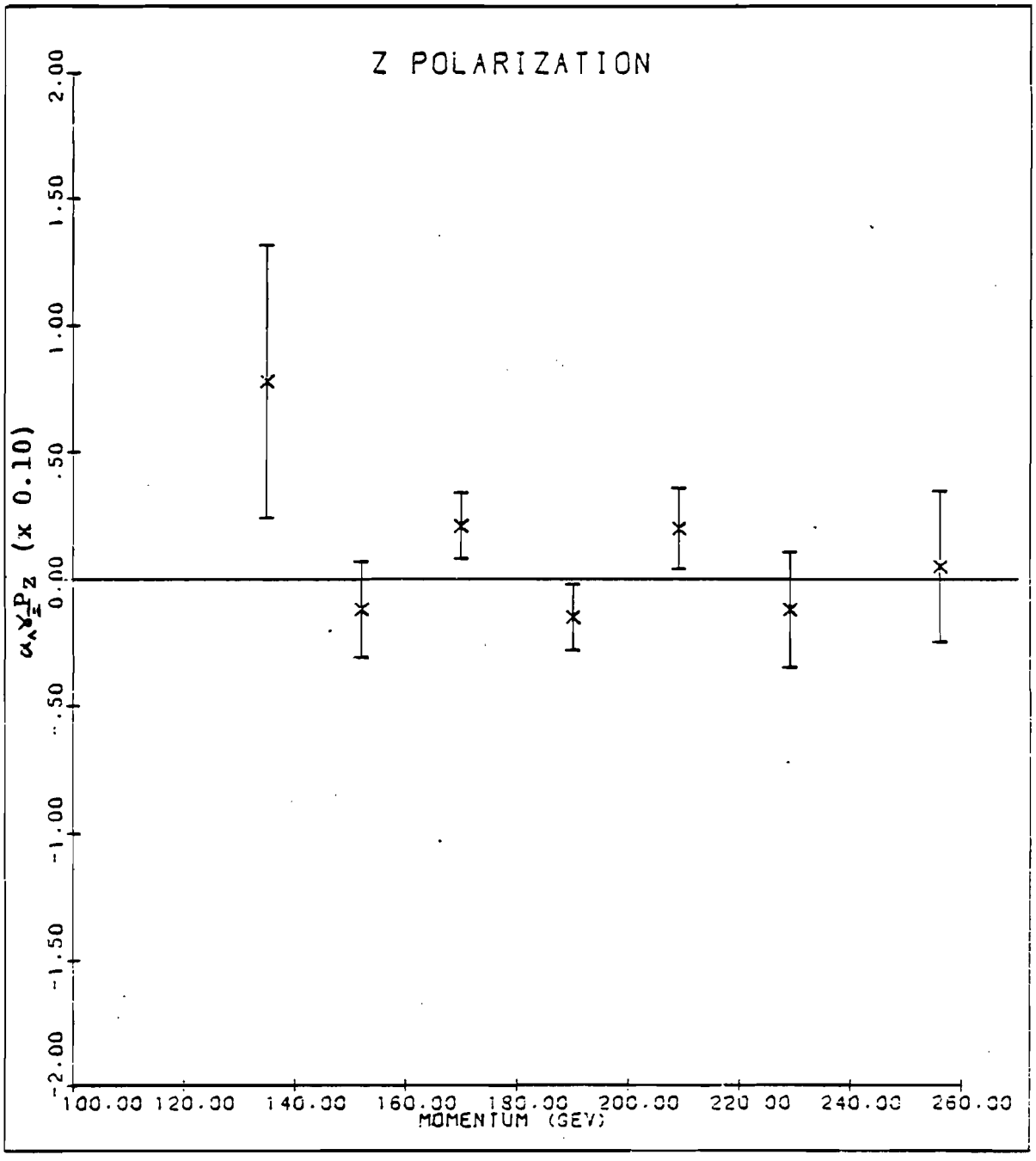


Figure 5.2 $\alpha_\Lambda \gamma_\Sigma P_z$ vs. momentum
5 mrad, 6.6 T-m field

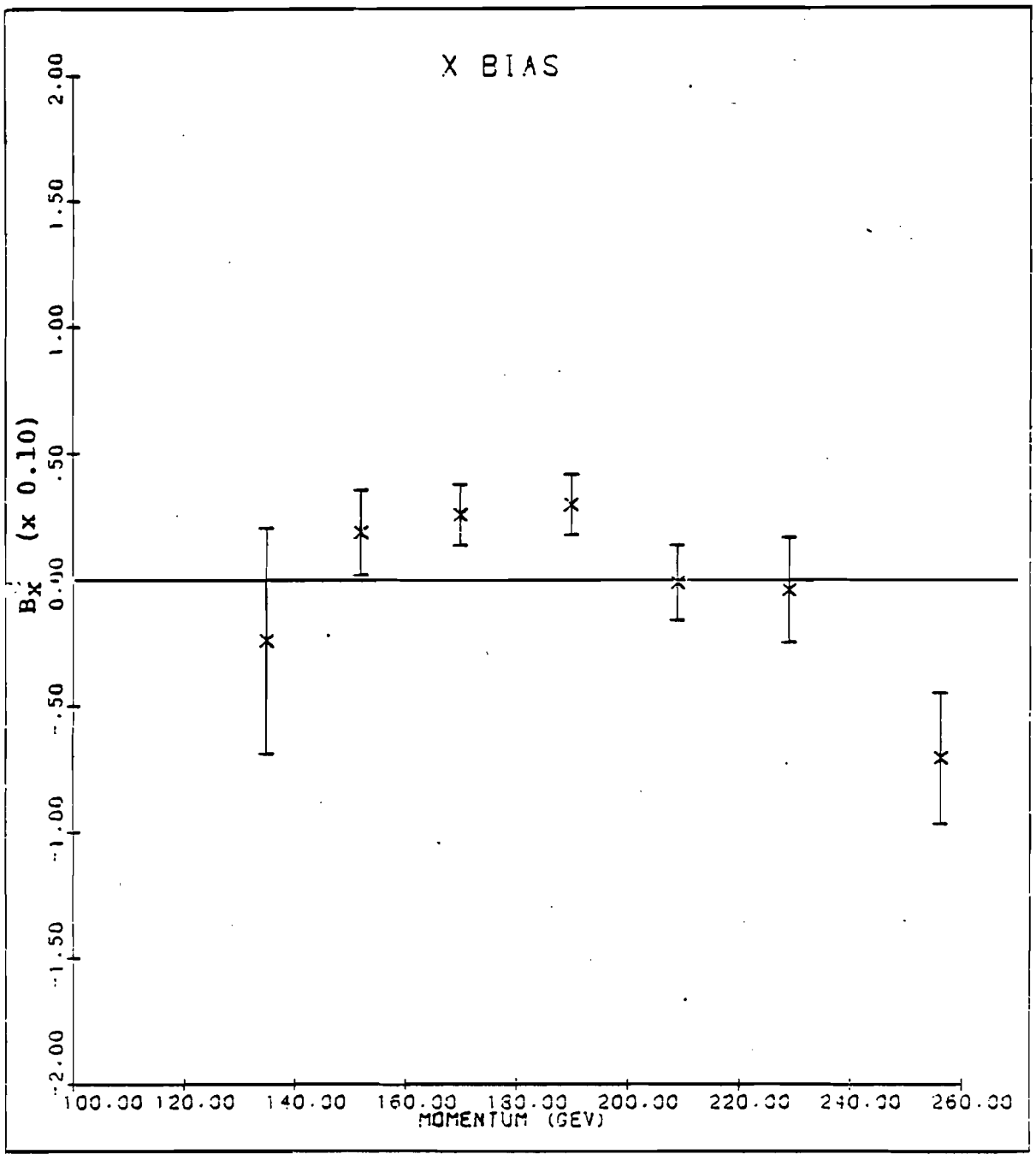


Figure 5.3 x bias vs. momentum
5 mrad, 6.6 T-m field

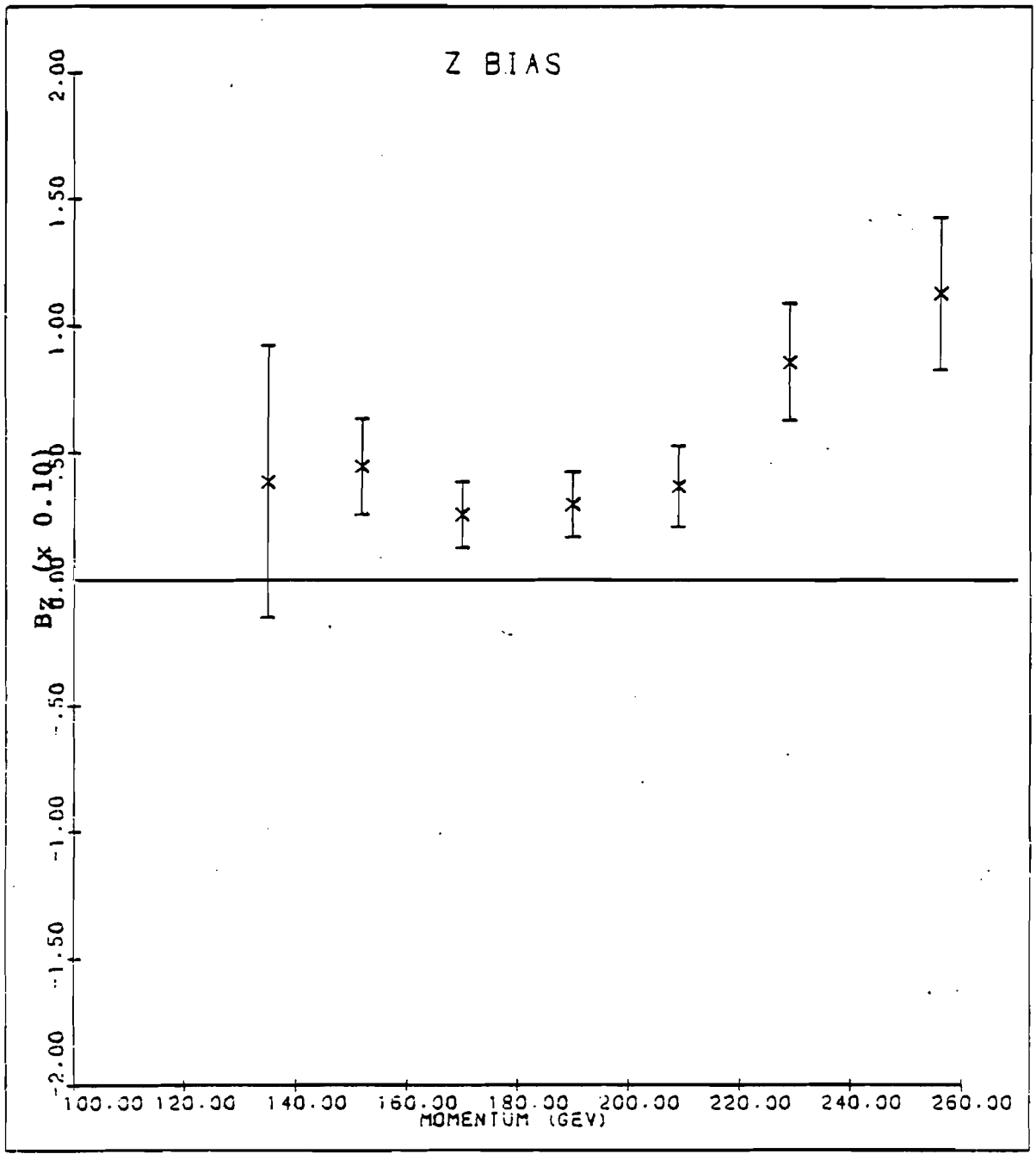


Figure 5.4 z bias vs. momentum
5 mrad, 6.6 T-m field

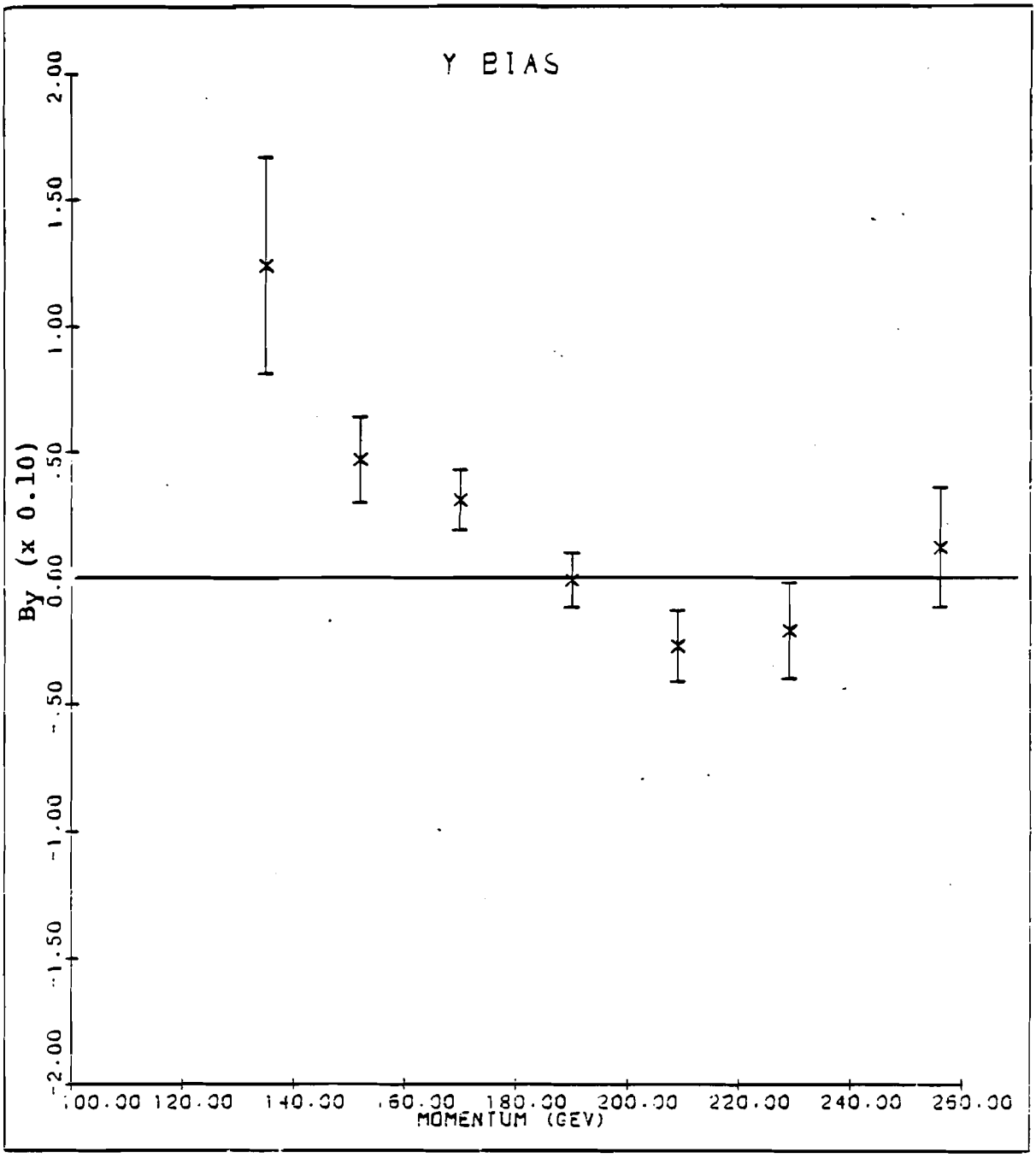


Figure 5.5 y bias vs. momentum
5 mrad, 6.6 T-m field

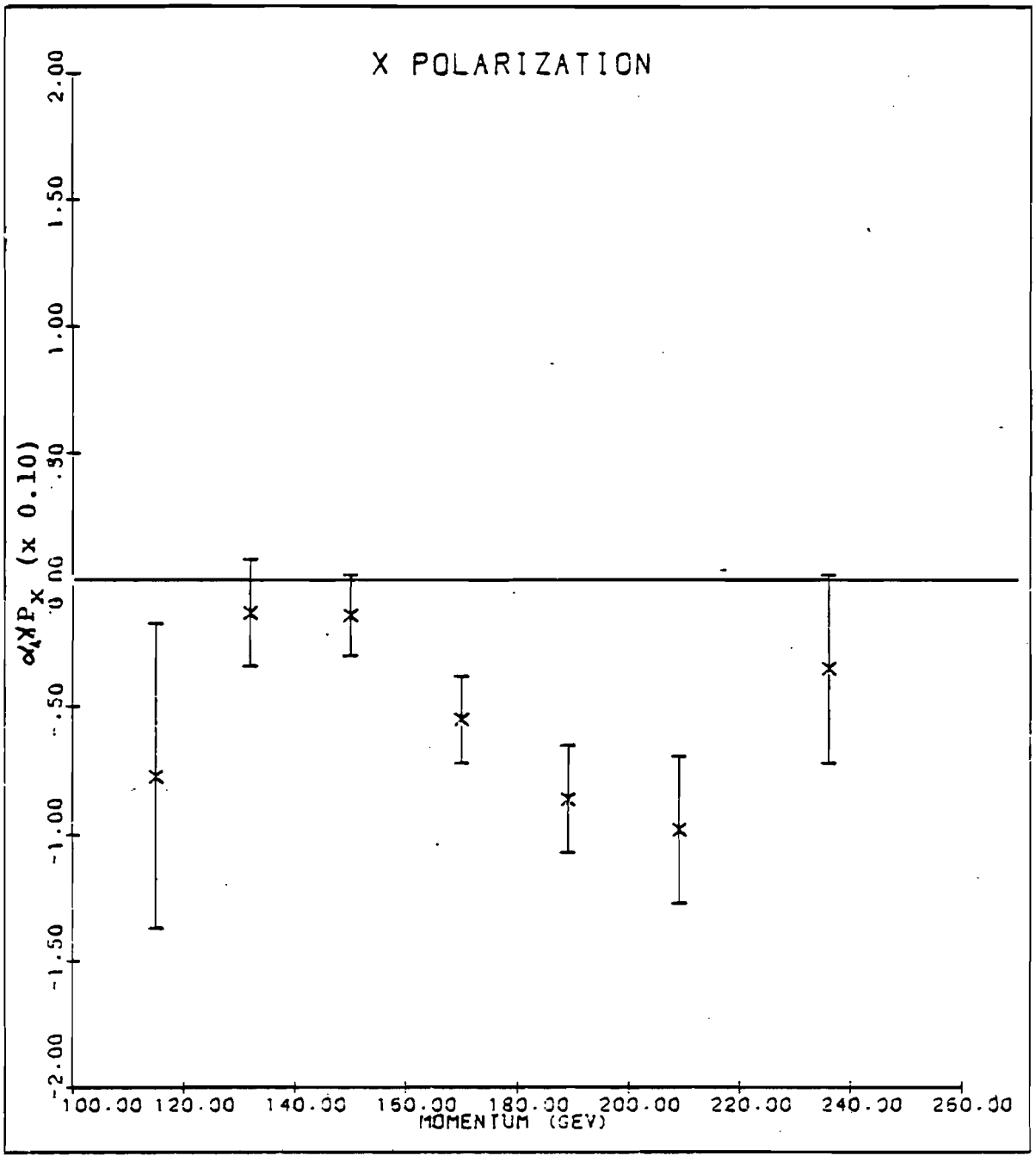


Figure 5.6 $\alpha_\Lambda \gamma_\Sigma P_\Lambda$ vs. momentum
5 mrad, 5.1 T-m field

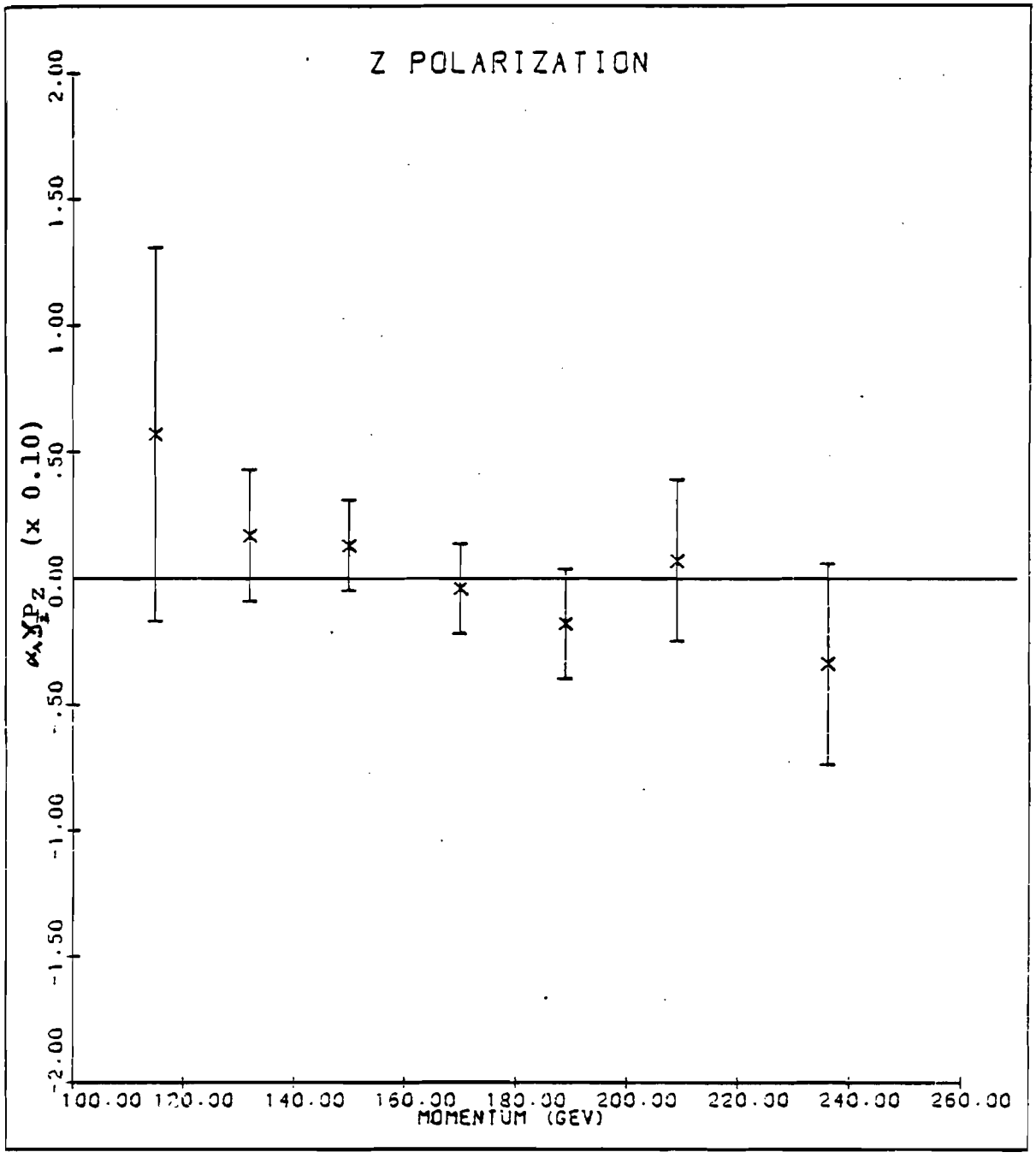


Figure 5.7 $\alpha_\Lambda Y_\Xi P_Z$ vs. momentum
5 mrad, 5.1 T-m field

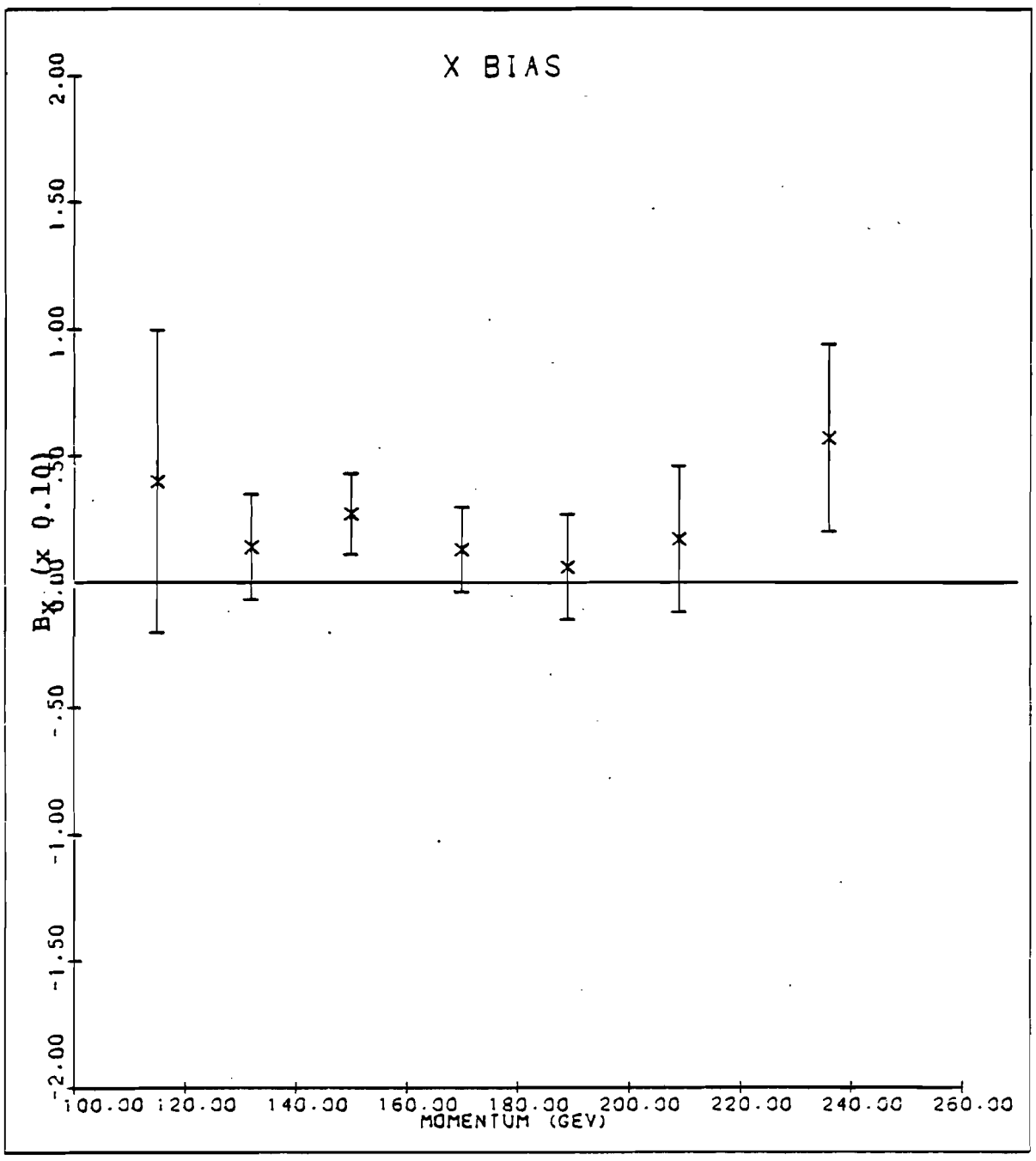


Figure 5.8 x bias vs. momentum
5 mrad, 5.1 T-m field

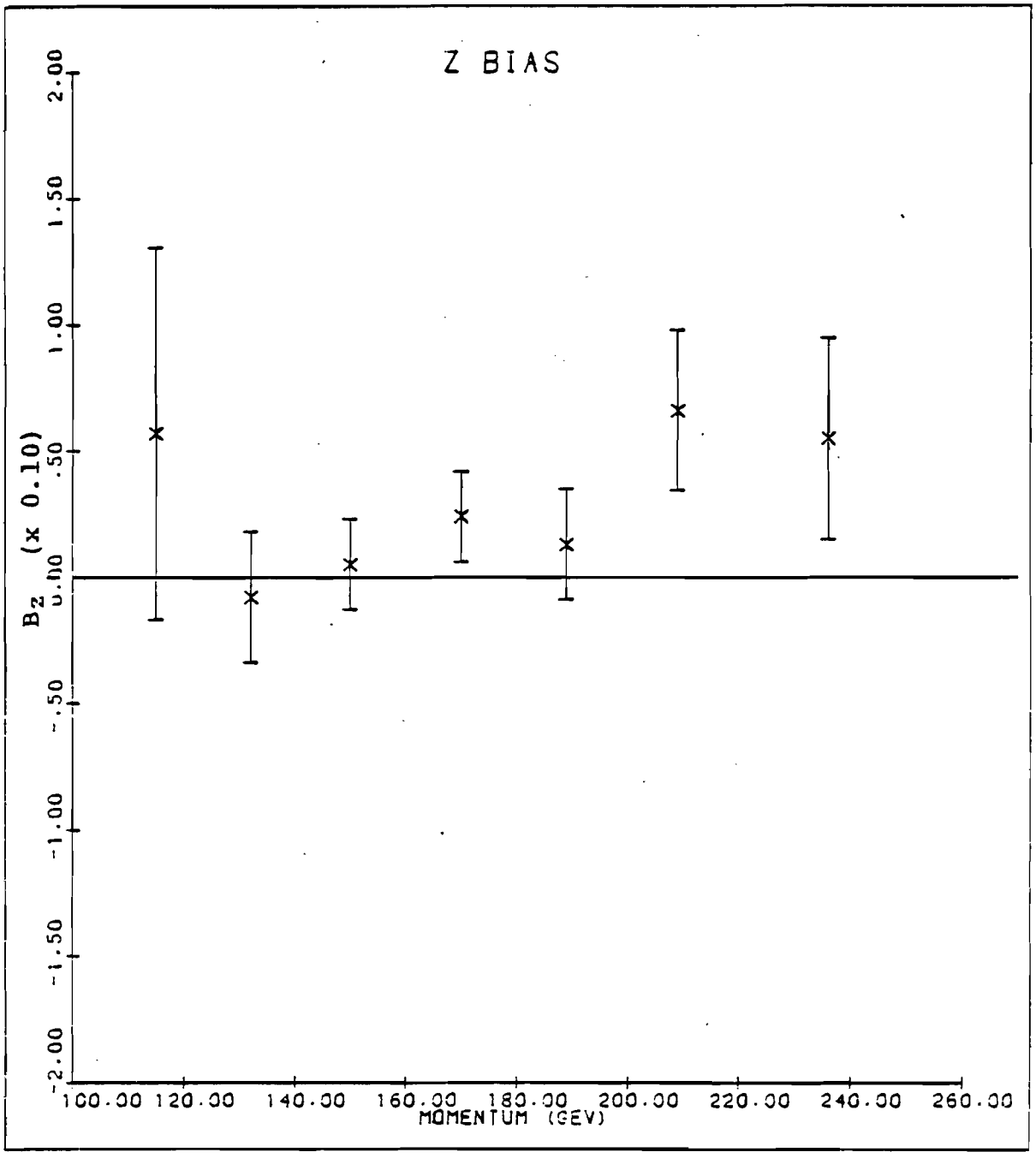


Figure 5.9 z bias vs. momentum
5 mrad, 5.1 T-m field

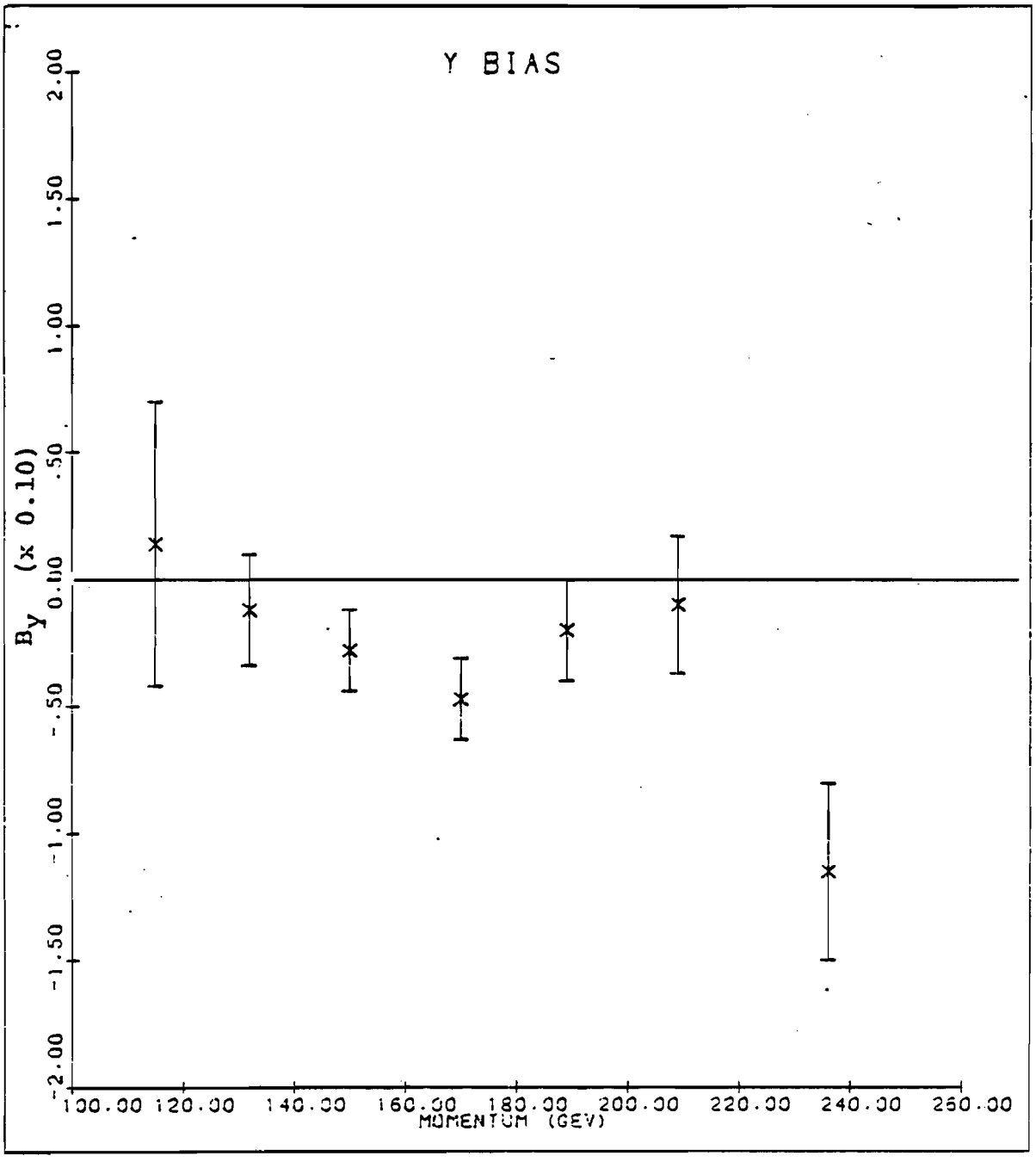


Figure 5.10 y bias vs. momentum
5 mrad, 5.1 T-m field

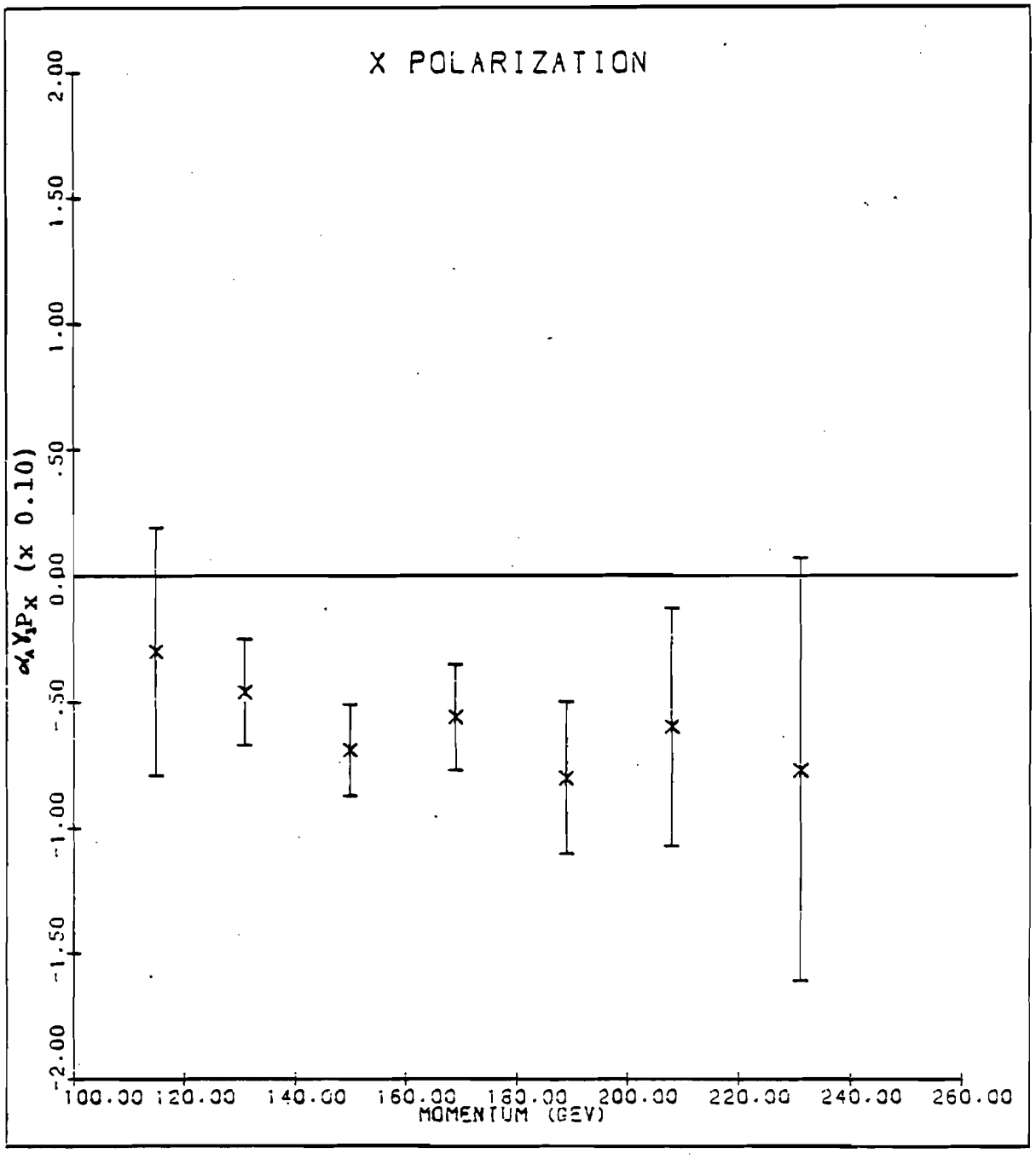


Figure 5.11 $\alpha_\Lambda \gamma_\Sigma P_x$ vs. momentum
7.5 mrad, 5.1 T-m field

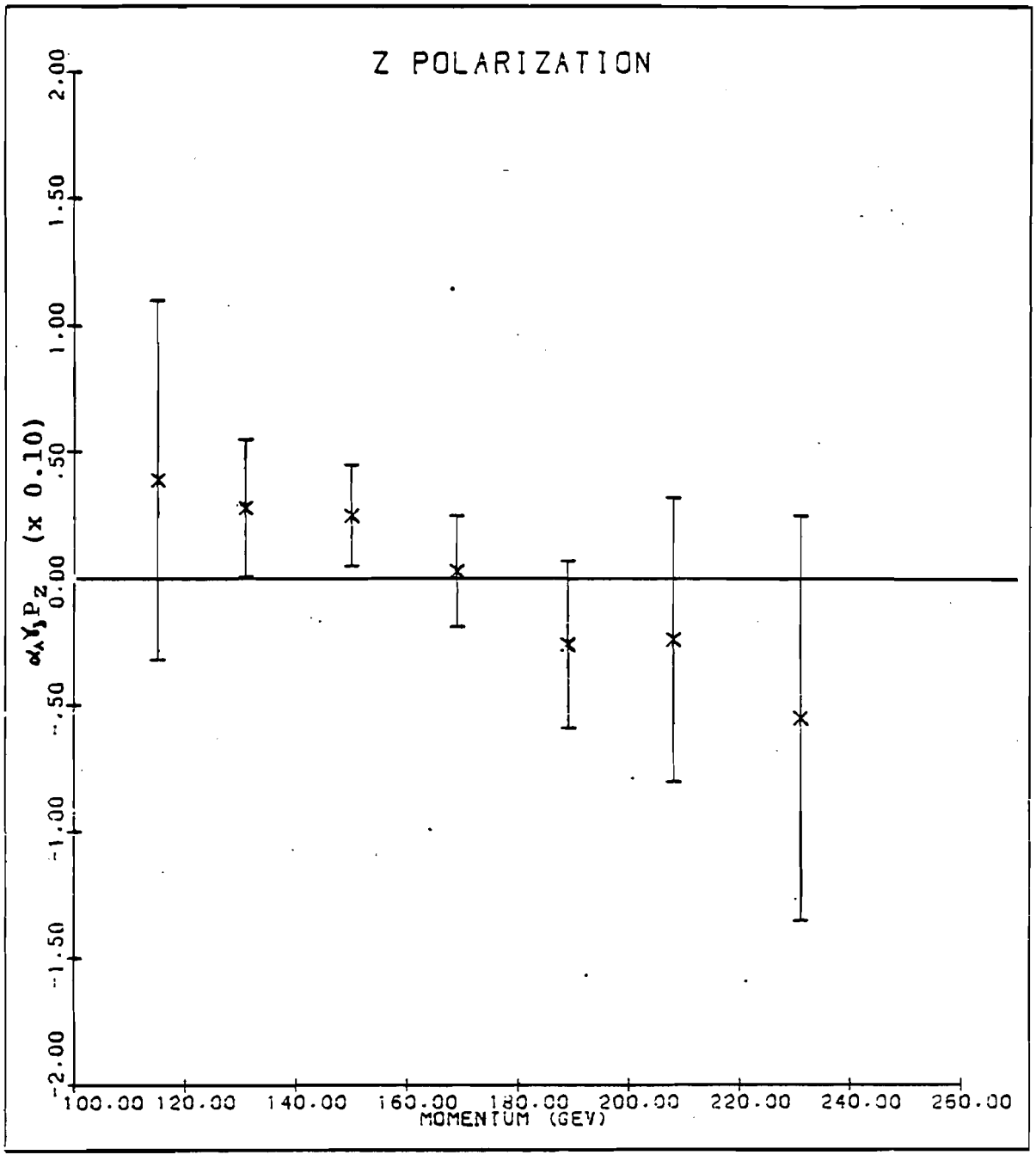


Figure 5.12 $\alpha_\Lambda \gamma_\Sigma P_Z$ vs. momentum
7.5 mrad, 5.1 T-m field

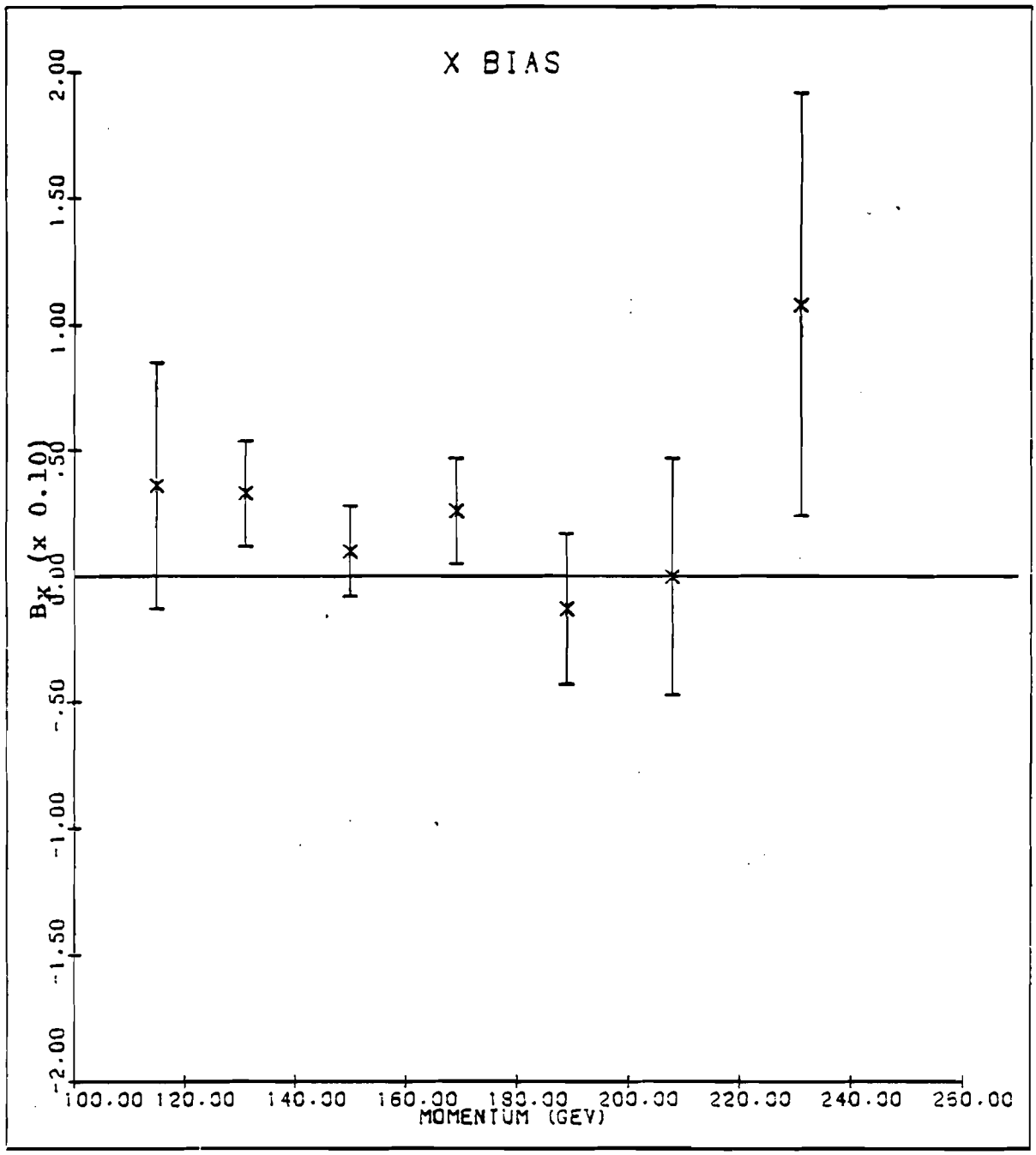


Figure 5.13 x bias vs. momentum
7.5 mrad, 5.1 T-m field

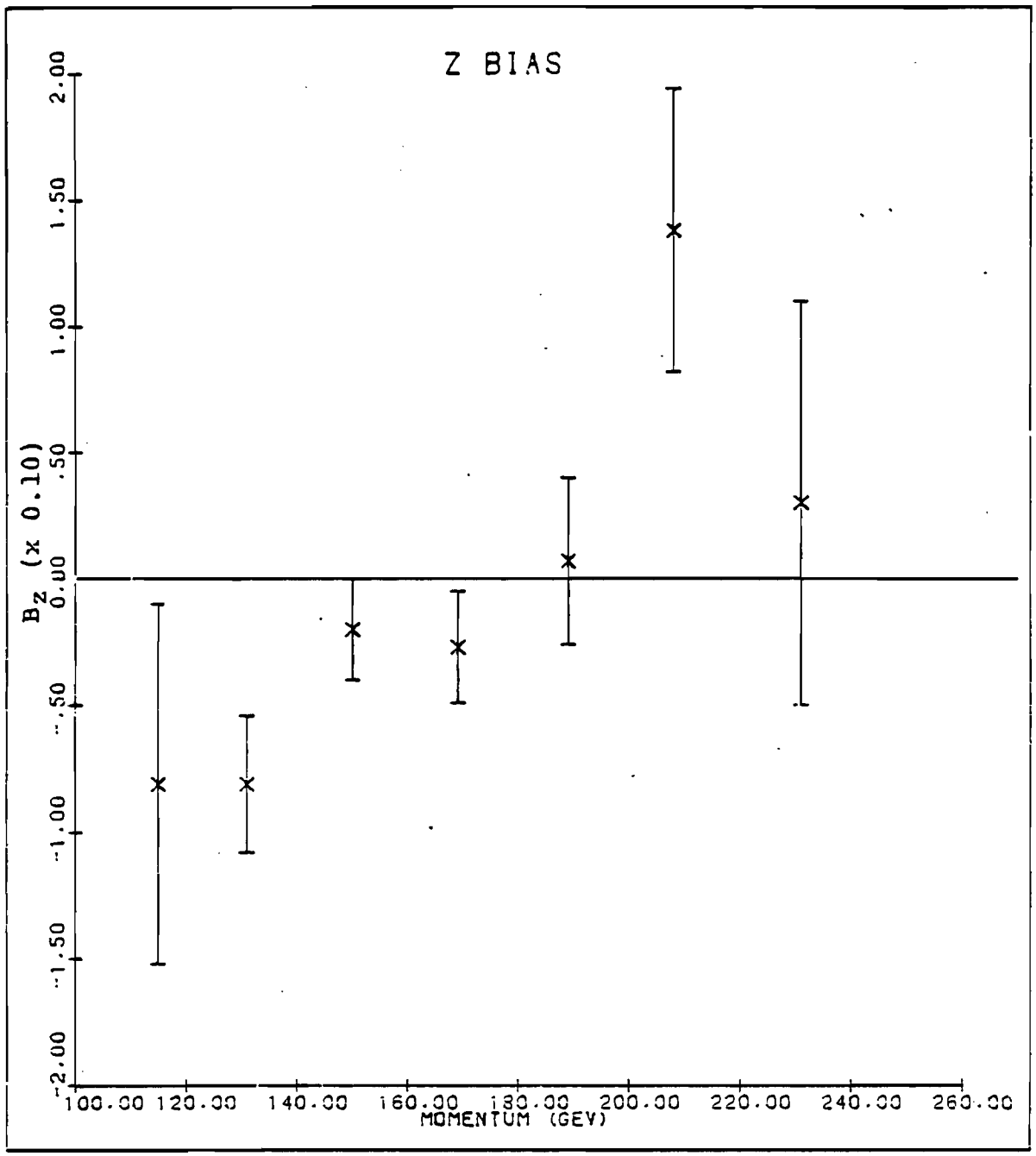


Figure 5.14 z bias vs. momentum
7.5 mrad, 5.1 T-m field

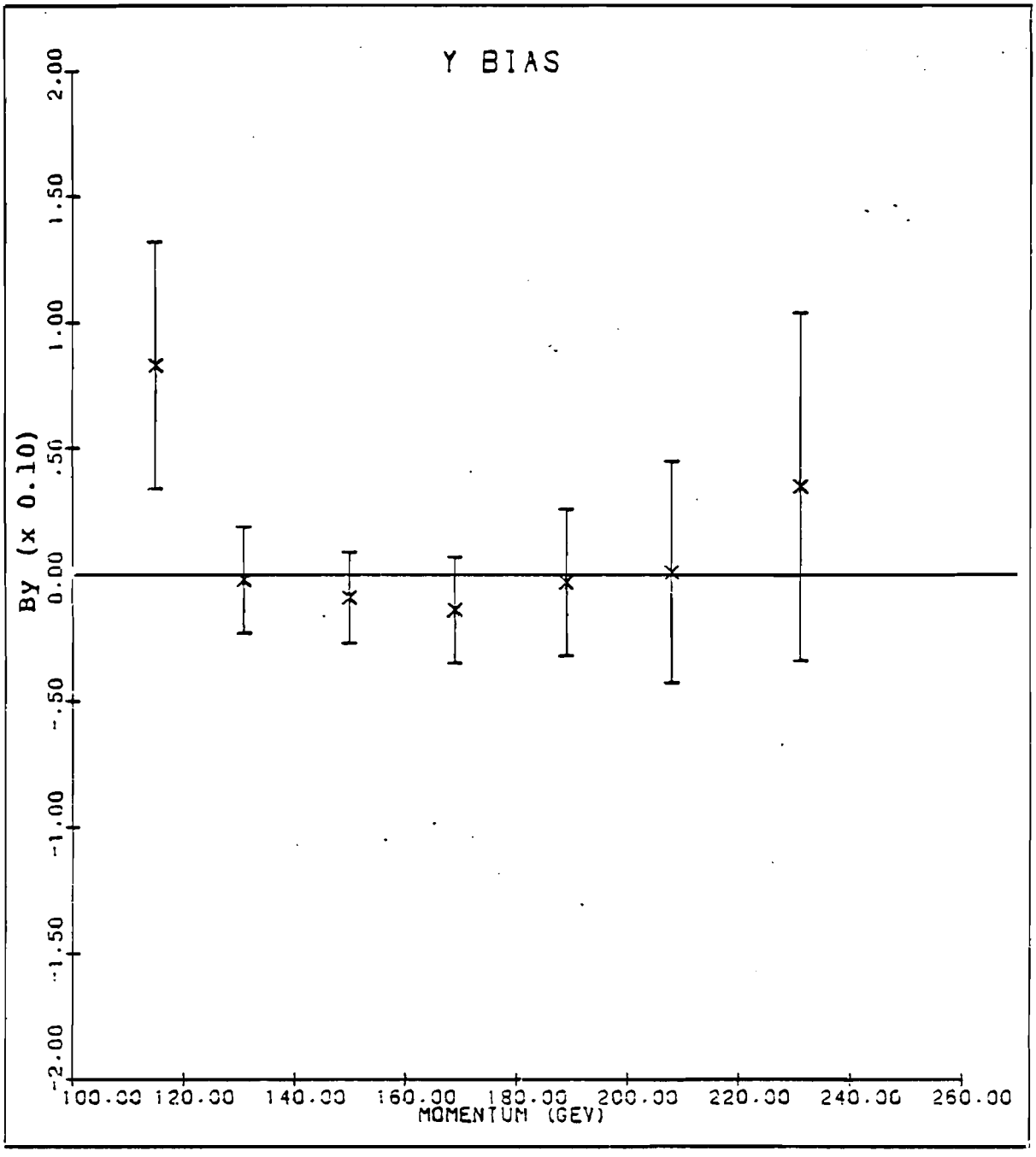


Figure 5.15 y bias vs. momentum
7.5 mrad, 5.1 T-m field

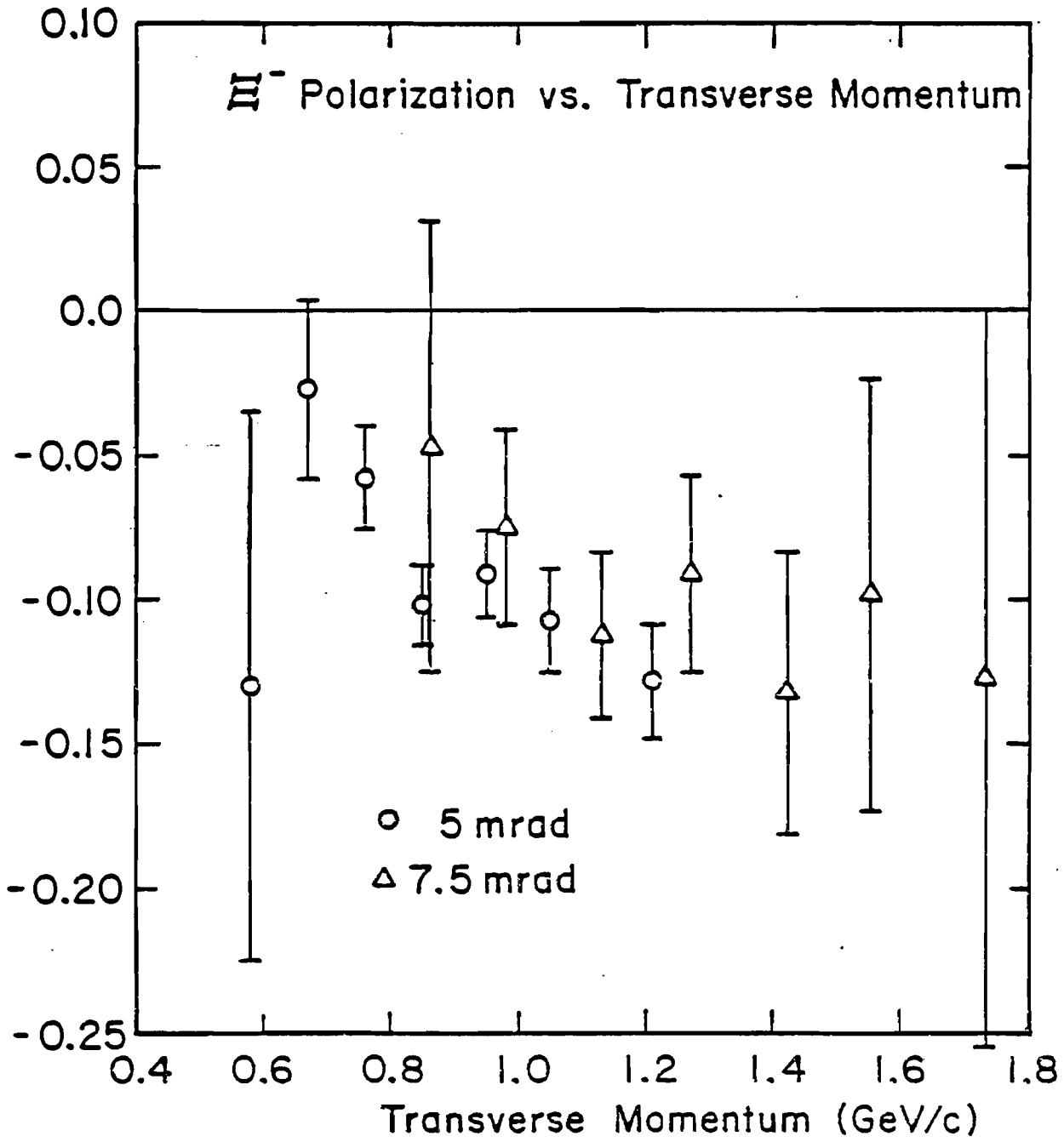


Figure 5.16 polarization as a function of transverse momentum for the 5.0 and 7.5 mr data.

## 5.2 The Asymmetry Parameter, $\alpha_{\Xi^-}$

The product $\alpha_\Lambda\alpha_\Xi$ was studied as a function of cuts in the same manner as the polarization. This was done for both the first and second iteration analysis. Each data set was analyzed separately to be sure that the result was independent of trigger biases, production angle and field integral. A summary of these studies are shown in Tables 5.5-5.6. The weighted average of all the data after the second iteration analysis, was measured to be $-0.303\pm0.004$. The error is purely statistical. The values of $\alpha_\Lambda\alpha_\Xi$ as a function of momentum after all cuts for both first and second iteration are listed in Tables 5.7-5.8. $\alpha_\Lambda\alpha_\Xi$ is plotted as a function of momentum for Sets 3-5 in Figs. 5.17-5.19. The value obtained for $\alpha_\Xi$, $-0.472\pm0.012$, though differing by more than $3\sigma$ from the present world average, is in good agreement with the result recently obtained from a CERN hyperon experiment, $\alpha_\Xi = -0.462\pm0.015$.[25]

| Set | $\int Bdl$ | $\theta$ | 1st Iteration | 2nd Iteration |
|---|---|---|---|---|
| 1 | 6.6 | 5.0 | $-0.2784 \pm 0.0134$ | $-0.2752 \pm 0.0134$ |
| 2 | 6.6 | 5.0 | $-0.2674 \pm 0.0105$ | $-0.2640 \pm 0.0105$ |
| 3 | 6.6 | 5.0 | $-0.2872 \pm 0.0058$ | $-0.2847 \pm 0.0058$ |
| 4 | 5.1 | 5.0 | $-0.2865 \pm 0.0080$ | $-0.2858 \pm 0.0080$ |
| 5 | 5.1 | 7.5 | $-0.2786 \pm 0.0096$ | $-0.2785 \pm 0.0096$ |

Table 5.5 $\alpha_\Lambda \alpha_{\Sigma^-}$ momentum averaged for all data sets, $\chi^2_k < 20$, vertex separation $> 0$ required, first and second iteration.

| | | | | |
|---|---|---|---|---|
| 1 | 6.6 | 5.0 | $-0.3077 \pm 0.0154$ | $-0.3049 \pm 0.0153$ |
| 2 | 6.6 | 5.0 | $-0.2891 \pm 0.0115$ | $-0.2866 \pm 0.0115$ |
| 3 | 6.6 | 5.0 | $-0.3110 \pm 0.0064$ | $-0.3092 \pm 0.0064$ |
| 4 | 5.1 | 5.0 | $-0.3034 \pm 0.0087$ | $-0.3031 \pm 0.0087$ |
| 5 | 5.1 | 7.5 | $-0.2985 \pm 0.0105$ | $-0.2987 \pm 0.0105$ |

Table 5.6 $\alpha_\Lambda \alpha_{\Sigma^-}$ momentum averaged for all data sets, all cuts applied, both first and second iteration.

| Pbin | P | 1st Iteration | 2nd Iteration |
|---|---|---|---|
| 140-160 | 153 | -0.4141±0.0737 | -0.4040±0.0735 |
| 160-180 | 170 | -0.3692±0.0351 | -0.3639±0.0351 |
| 180-200 | 190 | -0.2709±0.0287 | -0.2684±0.0287 |
| 200-220 | 209 | -0.2749±0.0330 | -0.2735±0.0329 |
| 220-240 | 229 | -0.2989±0.0419 | -0.2978±0.0418 |
| 240-290 | 255 | -0.3230±0.0537 | -0.3214±0.0536 |

Data set 1 - 6.6 T-m field, 5.0 mrad production angle

| | | | |
|---|---|---|---|
| 140-160 | 152 | -0.2707±0.0319 | -0.2650±0.0319 |
| 160-180 | 170 | -0.2901±0.0222 | -0.2870±0.0223 |
| 180-200 | 190 | -0.3005±0.0230 | -0.2985±0.0230 |
| 200-220 | 209 | -0.3005±0.0284 | -0.3004±0.0283 |
| 220-240 | 228 | -0.2504±0.0407 | -0.2475±0.0406 |
| 240-290 | 256 | -0.3187±0.0491 | -0.3187±0.0489 |

Data set 2 - 6.6 T-m field, 5.0 mrad production angle

Table 5.7 $\alpha_\Lambda \alpha_{\Sigma^-}$ as a function of momentum for both first and second iteration, Data Sets 1&2.

| Pbin | P | 1st Iteration | 2nd Iteration |
|---|---|---|---|
| 125-140 | 135 | -0.2130±0.0525 | -0.2131±0.0526 |
| 140-160 | 152 | -0.3009±0.0183 | -0.2993±0.0183 |
| 160-180 | 170 | -0.3197±0.0124 | -0.3183±0.0124 |
| 180-200 | 190 | -0.3106±0.0124 | -0.3091±0.0124 |
| 200-220 | 209 | -0.3006±0.0154 | -0.2992±0.0153 |
| 220-240 | 229 | -0.3393±0.0211 | -0.3348±0.0210 |
| 240-290 | 256 | -0.3095±0.0277 | -0.3069±0.0277 |

Data set 3 - 6.6 T-m field, 5.0 mrad production angle

| | | | |
|---|---|---|---|
| 105-120 | 115 | -0.2995±0.0662 | -0.3126±0.0658 |
| 120-140 | 131 | -0.2931±0.0232 | -0.2972±0.0232 |
| 140-160 | 150 | -0.3147±0.0168 | -0.3134±0.0168 |
| 160-180 | 170 | -0.2755±0.0175 | -0.2742±0.0175 |
| 180-200 | 189 | -0.3206±0.0216 | -0.3190±0.0216 |
| 200-220 | 209 | -0.3228±0.0308 | -0.3202±0.0308 |
| 220-270 | 236 | -0.3131±0.0390 | -0.3125±0.0387 |

Data set 4 - 5.1 T-m field, 5.0 mrad production angle

| | | | |
|---|---|---|---|
| 105-120 | 115 | -0.3084±0.0581 | -0.3216±0.0576 |
| 120-140 | 131 | -0.2329±0.0233 | -0.2368±0.0233 |
| 140-160 | 150 | -0.3087±0.0187 | -0.3072±0.0187 |
| 160-180 | 169 | -0.3153±0.0220 | -0.3139±0.0220 |
| 180-200 | 189 | -0.3273±0.0307 | -0.3246±0.0307 |
| 200-220 | 209 | -0.3353±0.0478 | -0.3316±0.0478 |
| 220-250 | 234 | -0.3417±0.0771 | -0.3395±0.0776 |

Data set 5 - 5.1 T-m field, 7.5 mrad production angle

Table 5.8 $\alpha_\Lambda \alpha_{\Sigma^-}$ as a function of momentum for both first and second iteration, data sets 3-5.

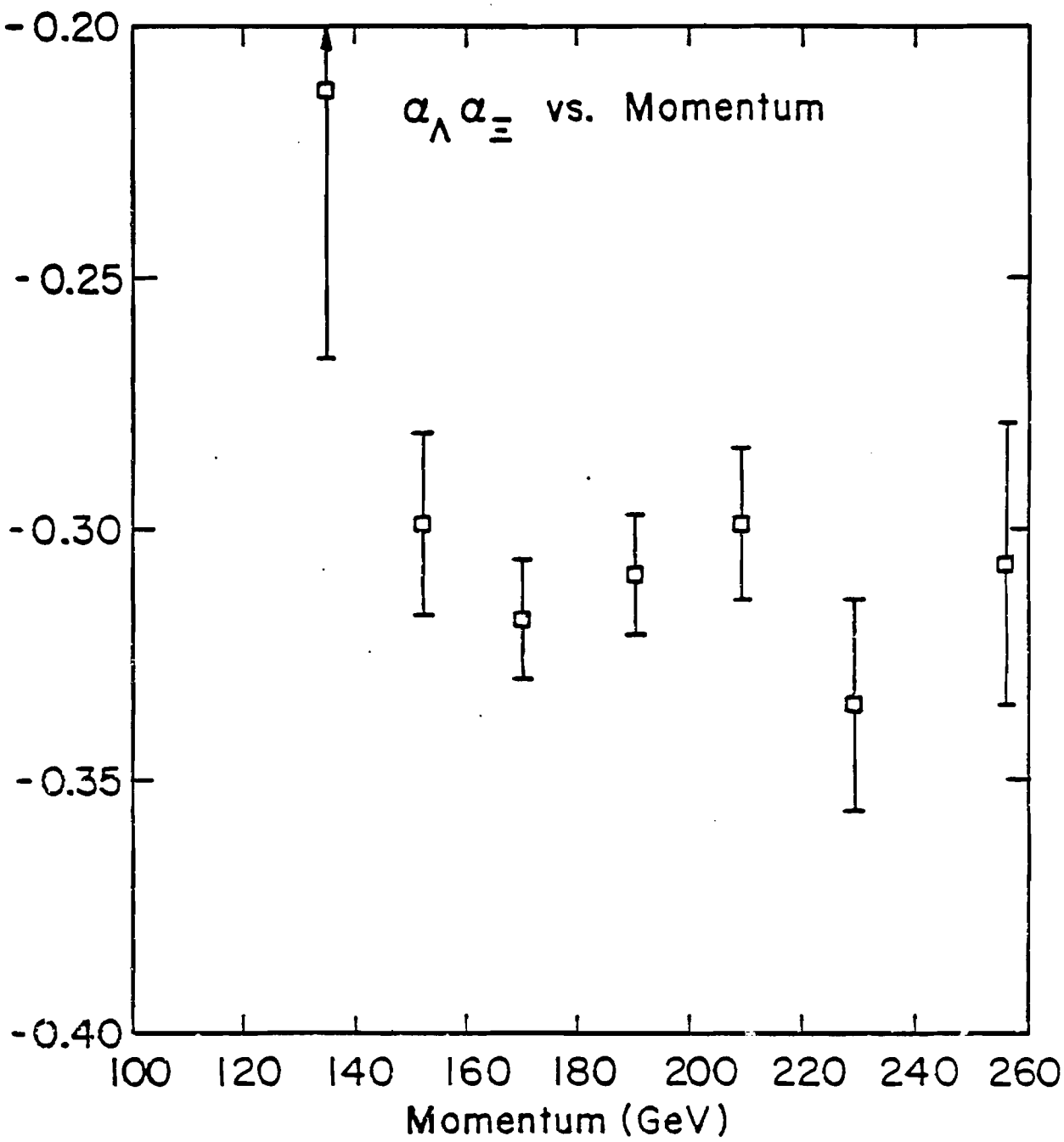


Figure 5.17 $\alpha_\Lambda \alpha_{\Xi^-}$ vs momentum
5 mrad, 6.60 T-m field

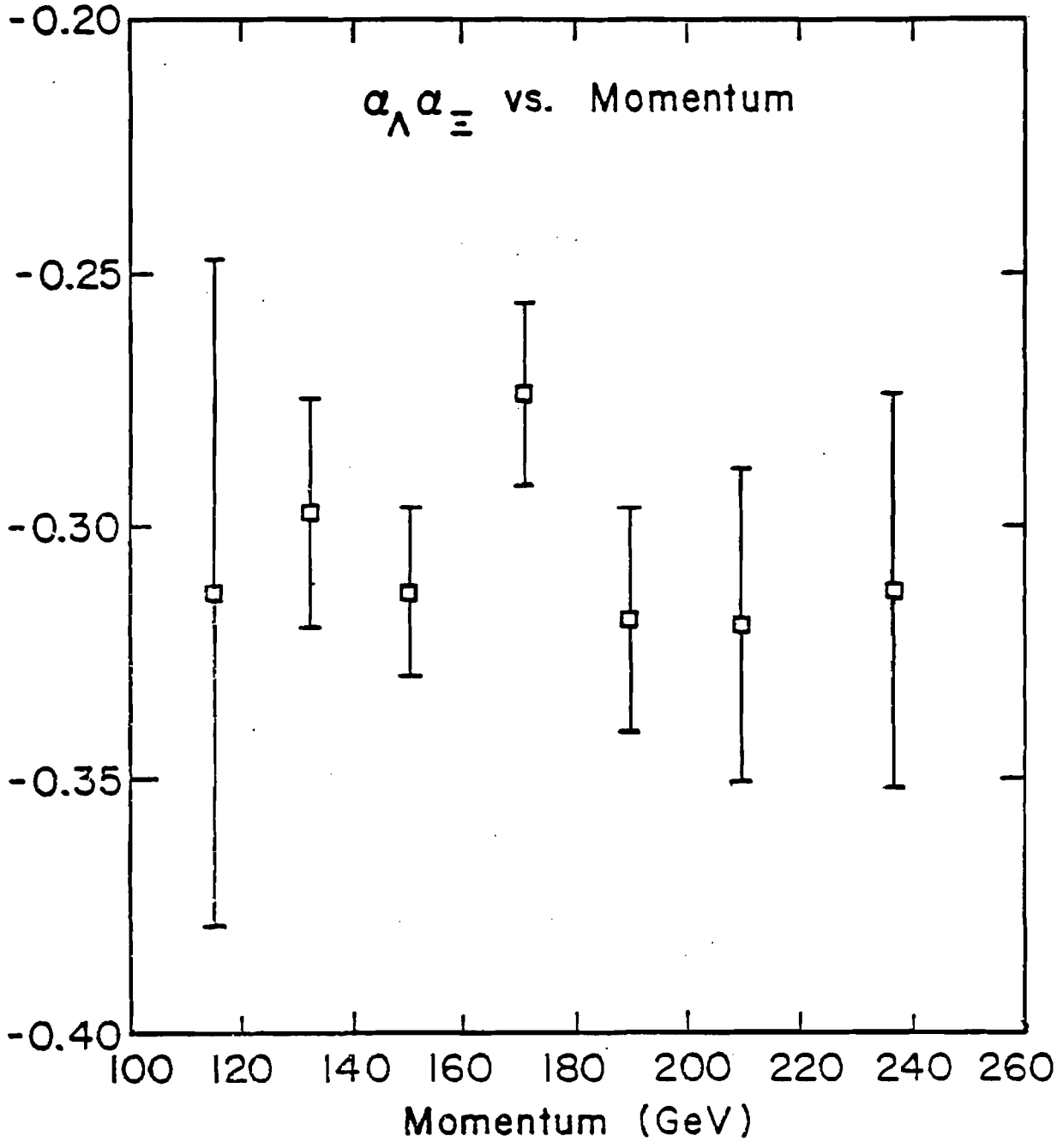


Figure 5.18 $\alpha_\Lambda \alpha_{\Xi^-}$ vs momentum
5 mrad, 5.13 T-m field

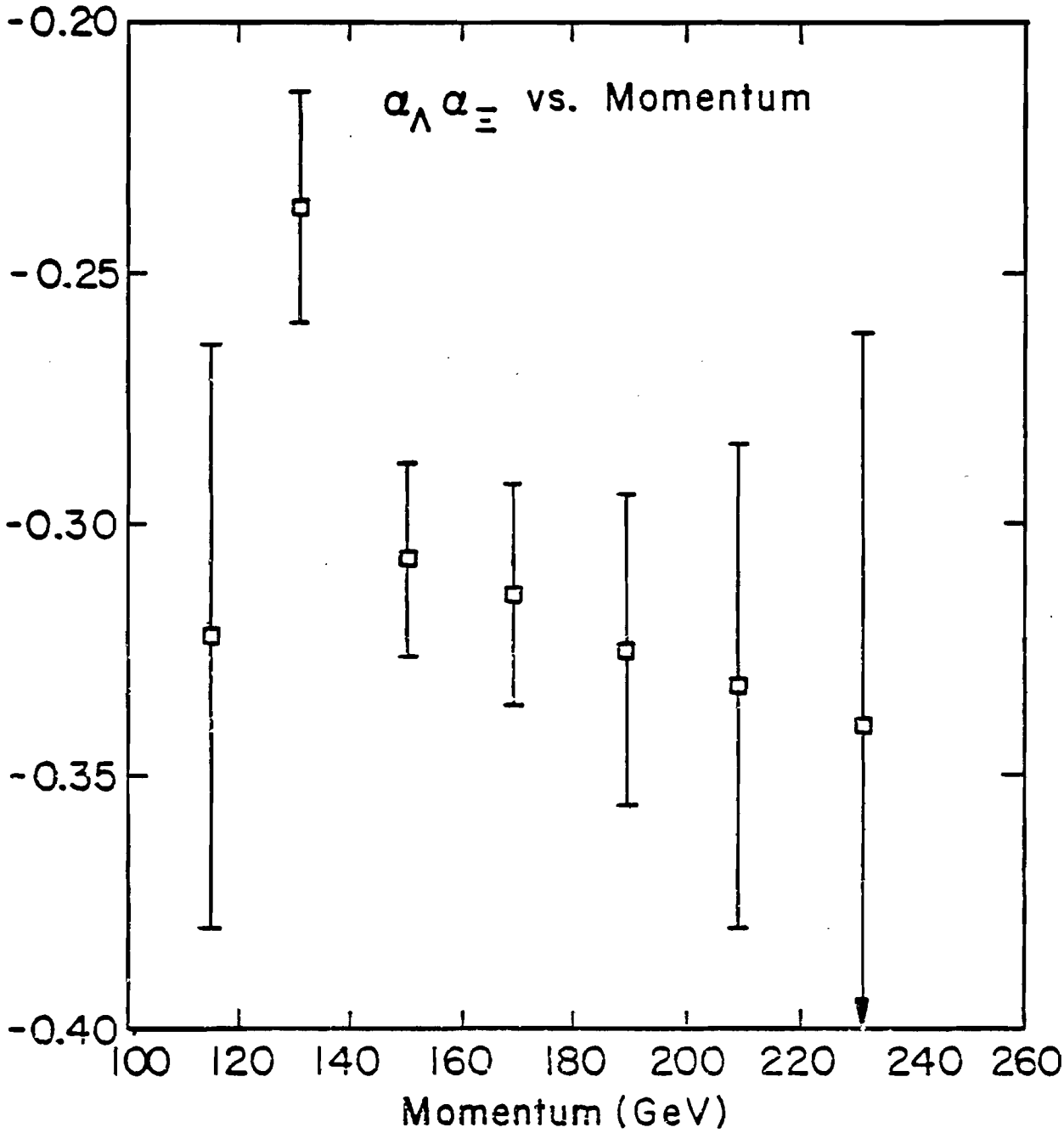


Figure 5.19 $\alpha_\Lambda \alpha_\Xi$- vs momentum
7.5 mrad, 6.60 T-m field

## 5.3 The Magnetic Moment

For a polarization vector which has precessed as it passed through the field, two questions arise. 1) In which direction was the vector initially pointing? 2) In which sense and how many times did it precess?

To illustrate how these questions were resolved in this experiment, the four lowest order precession conditions which were considered, are shown in Fig. 5.20. Since the precession angle is proportional to the field integral, if the field is reduced, the vector will precess through a proportionally reduced angle, and the configuration which matches the data can be selected. In this experiment the field was reduced from 6.60 T-m to 5.13 T-m, 7/9 the original value. What was observed was essentially no change in the direction of the polarization, giving the four possible angles at each of the fields listed in Table 5.9.

$$\phi = \tan^{-1}(\alpha_\Lambda \gamma_\Xi P_z / \alpha_\Lambda \gamma_\Xi P_x)$$

Using the additional constraint that if the field is turned off the spin cannot precess, for each possible solution, a least squares fit to the two points and the constraint through zero, was performed. These fits are

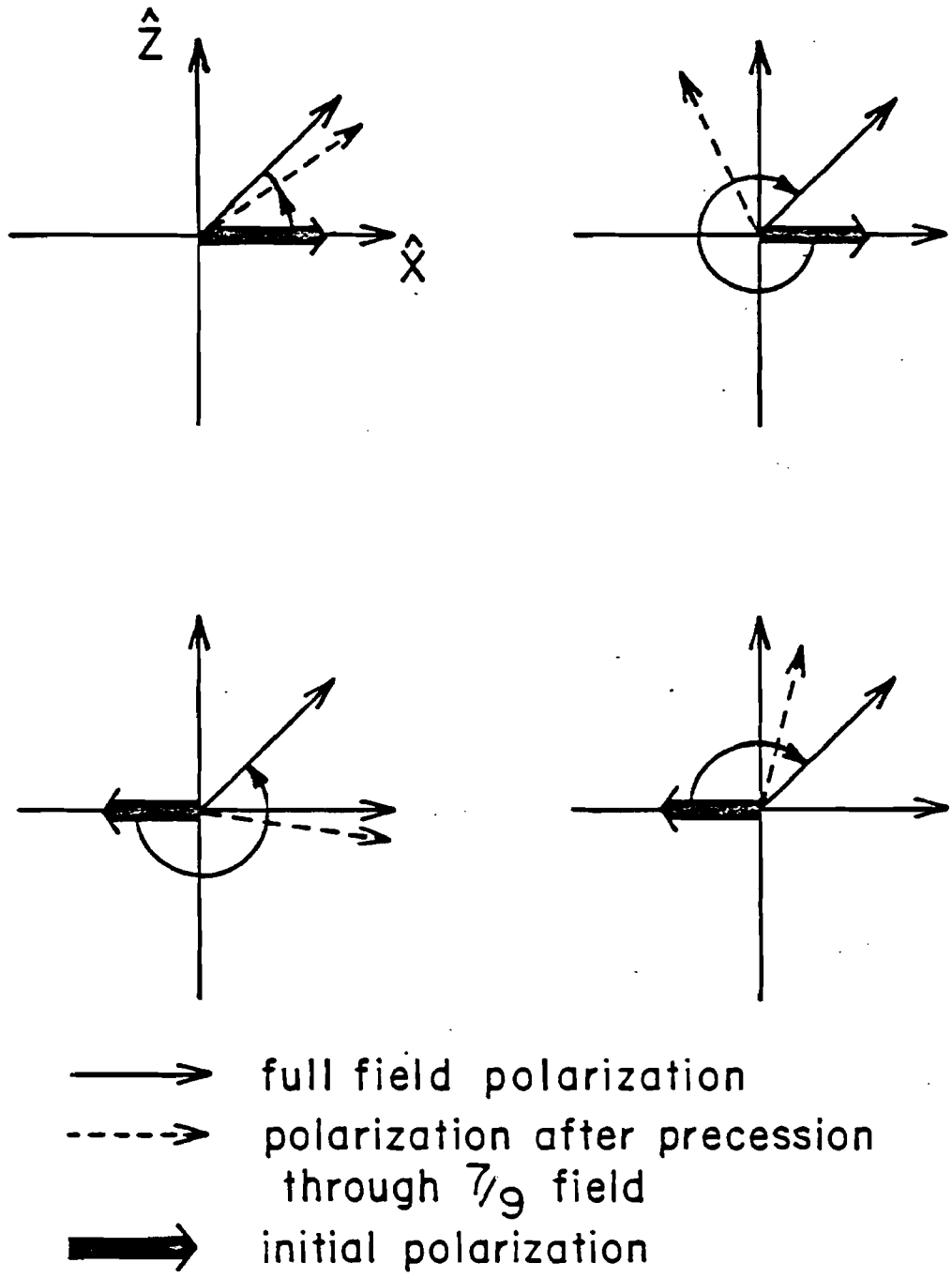


Figure 5.20 The four lowest order precession ambiguities shown for a polarization which has precessed through the full field and the four possible directions after precession through 7/9 field.

illustrated graphically in Fig. 5.21. Clearly the solution which indicates no precession has the best fit.

The slope of each line gives a possible value for the quantity -13.01(g/2 - 1). Extracting the value of g/2 and calculating the magnetic moment, for each solution, using Eq. 1.4, gives the results listed in Table 5.10.

These results are obtained using the momentum averaged polarizations listed in Table 5.1. Combining the data at each of the field integrals gives

at 5.13 T-m

$$\alpha_{\Lambda}\gamma_{\Xi}P_x = -0.0528 \pm 0.0064$$

$$\alpha_{\Lambda}\gamma_{\Xi}P_z = +0.0048 \pm 0.0073$$

and at 6.60 T-m

$$\alpha_{\Lambda}\gamma_{\Xi}P_x = -0.0595 \pm 0.0051$$

$$\alpha_{\Lambda}\gamma_{\Xi}P_z = -0.0001 \pm 0.0056$$

## 5.4 Error Propagation and Systematic Errors

The quoted uncertainties in both the polarization and $\alpha_{\Xi}$ analysis were determined by the $\chi^2$ minimization procedure of

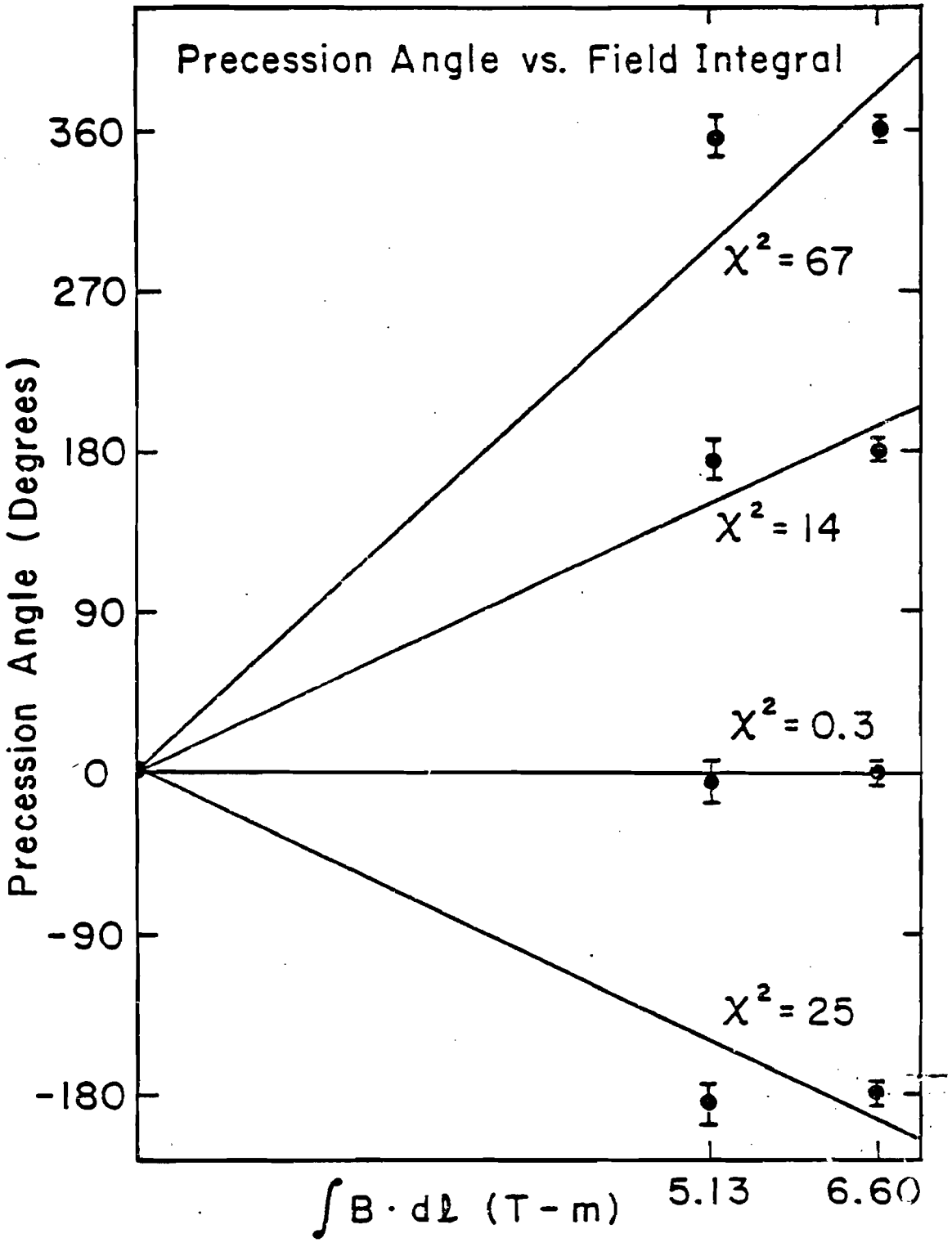


Figure 5.21 The precession angle vs. field integral for the four ambiguious solutions.

| $\vec{P}o$ | Rotation | Field Integral (T-m) 5.13 | 6.60 |
|---|---|---|---|
| -x | -- | $-5.2\pm7.9°$ | $+0.1\pm5.7°$ |
| +x | clockwise | $+174.8\pm7.9°$ | $+180.1\pm5.7°$ |
| -x | clockwise | $+354.8\pm7.9°$ | $+360.1\pm5.7°$ |
| +x | c-clockwise | $-185.2\pm7.9°$ | $-179.9\pm5.7°$ |

Table 5.9 Precession Angles at 6.6 and 5.1 T-m fields. $\vec{P}o$ indicates the initial polarization direction.

| g/2-1 | $\mu$ (n.m.) | $\chi^2$ |
|---|---|---|
| $+0.018\pm0.058$ | $-0.723\pm0.041$ | 0.34 |
| $-2.222\pm0.058$ | $+0.868\pm0.041$ | 14.4 |
| $-4.462\pm0.058$ | $+2.458\pm0.041$ | 67.1 |
| $+2.257\pm0.058$ | $-2.313\pm0.041$ | 24.7 |

Table 5.10 g-factors and magnetic moments for ambiguous solutions.

the hybrid Monte Carlo. The errors were determined by the change in the asymmetry giving a $\chi^2$ increase of 1. Since the number of events analyzed was large, the error determined in this manner agreed with the purely statistical error in the asymmetry measurements given by

$$\delta A = \sqrt{3/N}$$

where N is the total number of events analyzed.

The errors in the precession angles quoted in Table 5.9, are determined from the measured x and z asymmetries and their corresponding uncertainties.

$$d\phi = \sqrt{P_x^2\, dP_z^2 + P_z^2\, dP_x^2} / |P|^2$$

(Note, P has been written for simplicity, the actual calculations were done using the measured asymmetry, $\alpha_\Lambda \gamma_\Xi P$.)

The error in the magnetic moment (determined from the $\phi$ vs $\int Bdl$ plot) comes directly from the error in the determination of the slope of the line which is given by

$$\Delta s = 1/\sqrt{\sum_i (1/\sigma_i^2) Bdl_i}$$

where $\sigma_i$ is the uncertainty in the angle at the field $Bdl_i$. This gives an uncertainty in the quantity (g/2 - 1)

$$\Delta (g/2 - 1) = \Delta g/2 = \Delta s/13.01$$

giving an uncertainty in the magnetic moment

$$\Delta\mu = 0.71\ \Delta g/2$$

The uncertainties quoted for the master $\chi^2$ fit are again determined from the change in the parameter corresponding to a $\chi^2$ change of 1. The uncertainties for the polarization and biases agree with those obtained from the statistical calculation and the hybrid Monte Carlo fit. The uncertainty in the parameter g/2 - 1 is slightly smaller than that obtained from the $\phi$ vs $\int$ Bdl fit, i.e. $\Delta\sigma$ = 0.003. The results for the parameter g/2 - 1 agree within 0.5 $\sigma$.

Systematic errors in the magnetic moment coming from non-$\Xi^-$ background or collimator produced $\Xi$'s, both less than 1% effects, are certainly smaller than the statistical error in the measurement.

Based on the MC studies, the contribution of reconstruction biases to the measurement of the asymmetry parameter is assumed to be small and less than the statistical error. However, since the biases and the asymmetry were seen to be affected by kinematic constraints a possible systematic error based on studying the variation of the signal with cuts was estimated to be 0.004.

## 5.5 The Magnetic Moment Fit

Since the biases were considered to be functions of momentum only, they were expected to be independent of the running conditions such as production angle and precession field. The results of the master $\chi^2$ fit indicated that this assumption was reasonable. The momentum dependence of the biases was apparent even in the momentum averaged asymmetries, where for example, the 7.5 mrad data had a mean momentum 30 GeV lower than the 5 mrad, 6.6 T-m data.

To test the consistency of the data sets independently, the master fit was performed using the momentum averaged asymmetries. The biases were considered to be functions of the data set and all sets were required to have the same value of g/2 - 1. The results of this fit are shown in Table 5.11. The results of the fit give values of the polarization and biases completely constent with the momentum averaged values given in Table 5.1.

The $\chi^2$ for the fit is 2.21 for 4 degrees of freedom (20 data points and 16 fitted parameters). The value for g/2 - 1 is $+0.008 \pm 0.005$. Using Eq. 1.4 this gives a magnetic moment of

$$\mu_{\Xi^-} = -0.716 \pm 0.040 \text{ nuclear magnetons}$$

| Data Set | Polarization | Bx | Bz |
|---|---|---|---|
| 1 | $-0.094 \pm 0.025$ | $+0.021 \pm 0.016$ | $+0.033 \pm 0.016$ |
| 2 | $-0.098 \pm 0.017$ | $+0.010 \pm 0.011$ | $+0.033 \pm 0.012$ |
| 3 | $-0.099 \pm 0.010$ | $+0.014 \pm 0.006$ | $+0.041 \pm 0.007$ |
| 4 | $-0.076 \pm 0.013$ | $+0.020 \pm 0.008$ | $+0.019 \pm 0.009$ |
| 5 | $-0.102 \pm 0.015$ | $+0.019 \pm 0.010$ | $-0.020 \pm 0.012$ |

$\chi^2 = 2.21$
$\chi^2/df = 0.55$
$g/2 - 1 = +0.008 \pm 0.055$

Table 5.11 $\chi^2$ fit for all data sets constrained to the same value of $g/2 - 1$.

# CHAPTER 6

# Implications

## 6.1 Inclusive Polarization

The underlying mechanism which causes inclusive polarization is not understood. However, it does indeed appear to be a general feature of hyperon production. Figs. 6.1-6.2 show the inclusive polarization for the $\Sigma^+$, $\Sigma^-$, $\Lambda$, $\Xi^0$ and $\Xi^-$.

It is possible to construct a mechanism to explain relationships amongst polarizations of the various hyperons. In the production of $\Sigma^+$, $\Sigma^0$, and $\Lambda$ hyperons, it is assumed that one quark in the incident proton is lost through a hard

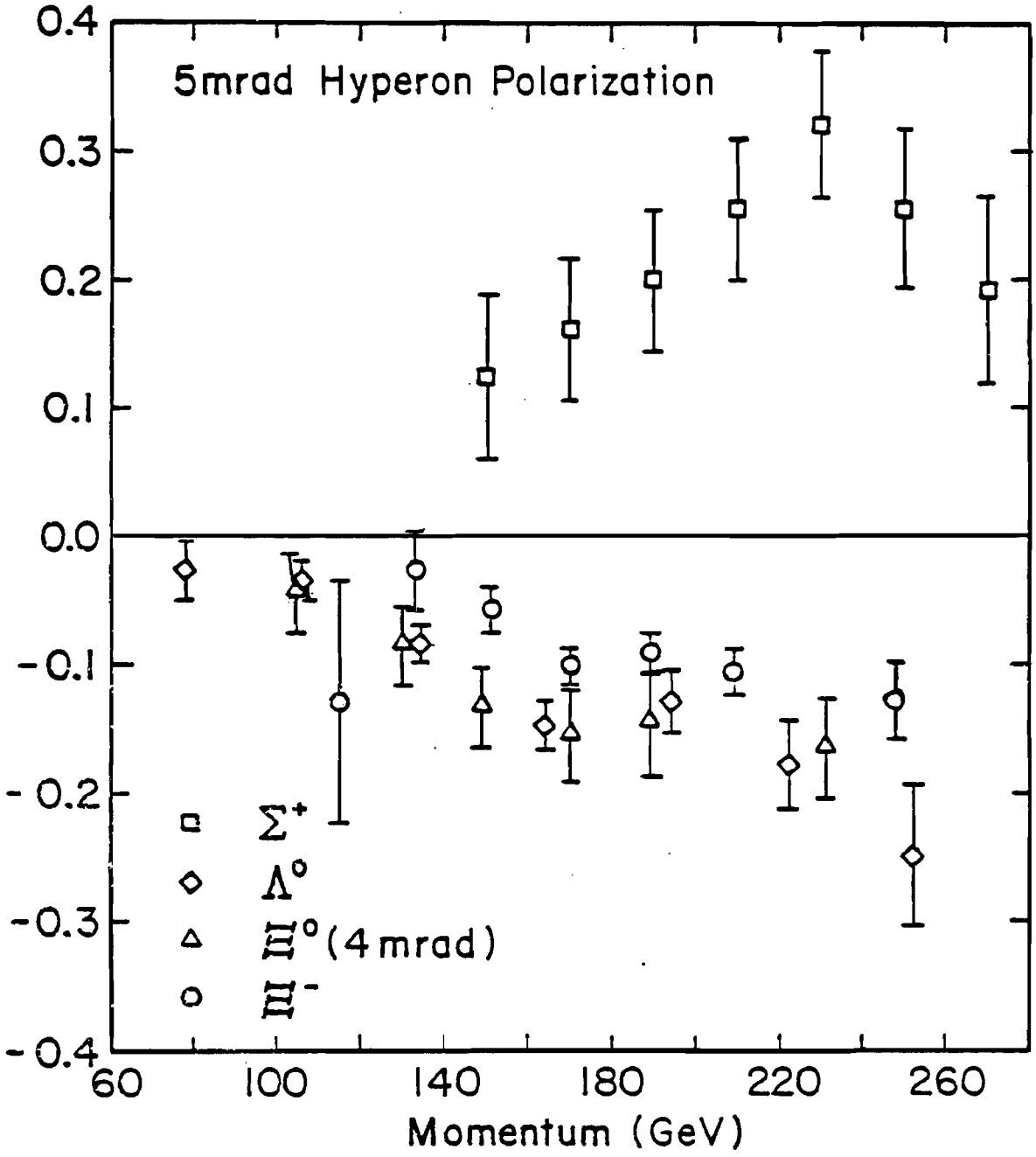


Figure 6.1 Hyperon inclusive polarization as a function of momentum for 5 mrad production angle.

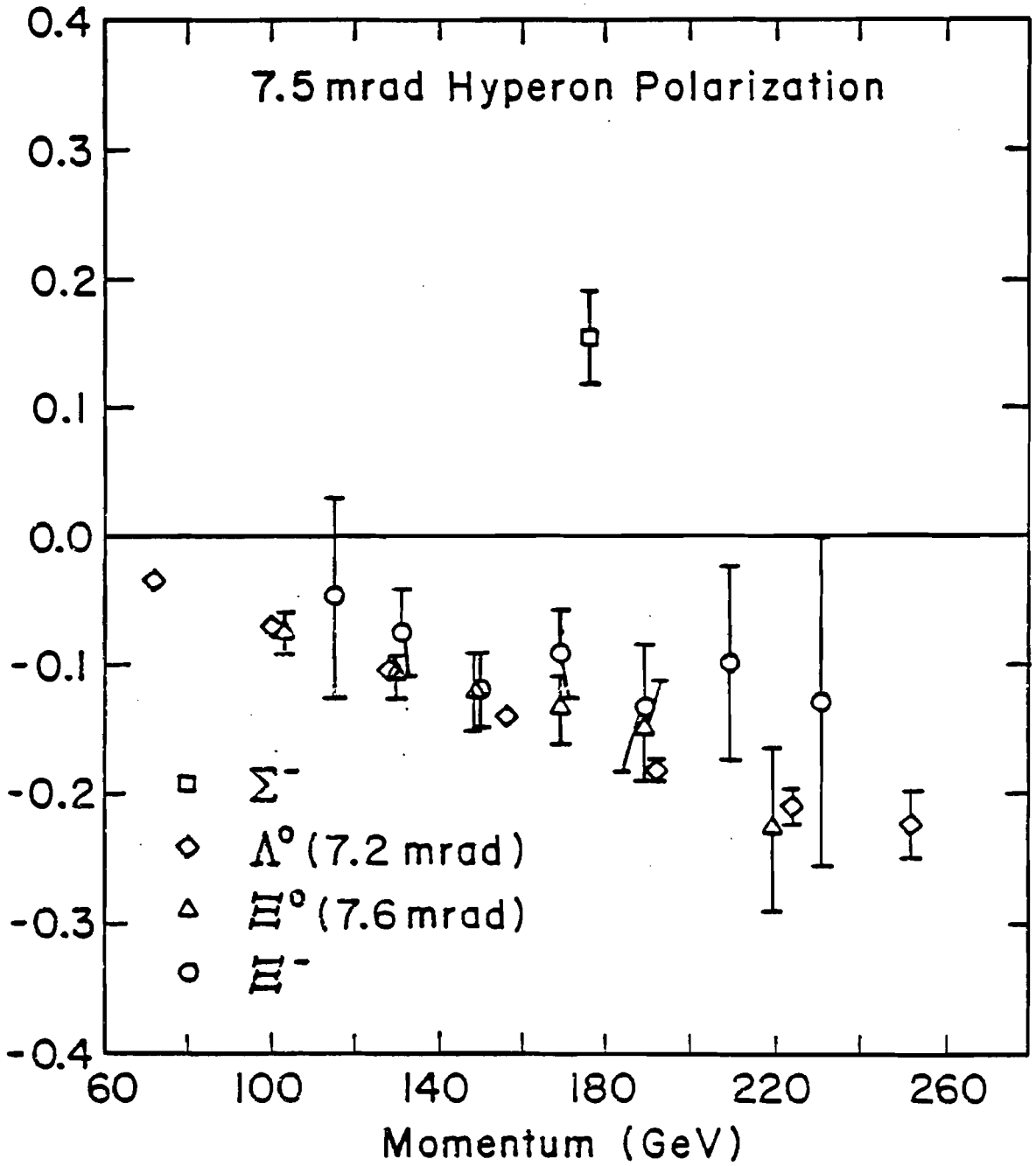


Figure 6.2 Hyperon inclusive polarization as a function of momentum for 7.5 mrad production angle.

collision leaving a spectator diquark (uu or ud) which then combines with an s quark from the sea to form the outgoing hyperon. Thus uud → uds produces a $\Lambda$ or $\Sigma^0$, and uud → uus produces a $\Sigma^+$. It is assumed that the s quark is polarized by some unspecified mechanism, which is correlated with transverse momentum. In the $\Lambda$, because the (ud) spectator is in a singlet state, the polarization of the $\Lambda$ is just given by the polarization of the strange quark. For the $\Sigma^0$ and $\Sigma^+$ the non-strange quarks must be in a triplet state, so the polarization of the composite baryon is opposite to that of the strange quark. When this is worked out in detail, one finds [7]

$$\vec{P}_{\Lambda} = \vec{P}_{\Sigma^0} = -1/3\ \vec{P}_{\Sigma^+}$$

In the $\Xi^0$ and $\Xi^-$ a single, unpolarized spectator quark comes from the incident proton (uud → dss or uud → uss). It is assumed that the same mechanism that produces the strange quark in the $\Sigma$'s and $\Lambda$ produces two succesive strange quarks, uncorrelated with each other, but with the same polarization as in the case of the $\Lambda$. Thus the resulting polarization will be the same sign as the $\Lambda$, and roughly the same magnitude. [26]

$$\vec{P}_{\Lambda} = \vec{P}_{\Xi^0} = \vec{P}_{\Xi^-}$$

The sign reversal of the $\Sigma^+$ polarization has been

observed,[27] though the measured magnitude is larger than the predicted one. This implies that the (uu) diquark must also be polarized, but in a direction opposite to that of the s quark. Miettinen and DeGrand argue that if it is assumed that sea quarks recombine with spins down relative to the scattering plane, while spectator quarks recombine with their spins up, the observed relations

$$\vec{P}_{\Lambda} = \vec{P}_{\Xi^0} = \vec{P}_{\Xi^-} = -\vec{P}_{\Sigma^+}$$

can be explained.[8] However, they predict that $\vec{P}_{\Sigma^-} = -\vec{P}_{\Sigma^+}$ which does not agree with the direction of the $\Sigma^-$ polarization determined from the E620 data.[16]

## 6.2 The $\Xi$ Asymmetry Parameters

In the decay $\Xi \to \Lambda\pi$, the s (L=0) and p (L=1) waves are composed of the isospin changing amplitudes $\Delta I = 1/2$ and $\Delta I = 3/2$. These amplitudes can be related to experimental observables such as lifetimes and asymmetry parameters.[28]

If only $\Delta I = 1/2$ transitions are allowed

$$\frac{\alpha(\Xi^0 \to \Lambda\pi^0)}{\alpha(\Xi^- \to \Lambda\pi^-)} = 1$$

and

$$\frac{\Gamma(\Xi^0 \to \Lambda\pi^0)}{\Gamma(\Xi^- \to \Lambda\pi^-)} = 1/2$$

(Phase space corrections modify these ratios to 0.977 and 0.484, respectively.) Experimental evidence indicates that the $\Delta I = 1/2$ amplitudes dominate in hyperon decay, though the extent of the dominance has not been precisely determined and theoretical attempts to explain the reasons for a "$\Delta I = 1/2$ Rule" have not been overwhelmingly succesful.[29]

The recent precise determination of the $\Xi^0$ asymmetry parameter $(-0.407 \pm 0.012)$[30] and the $\Xi^-$ result presented here $(-0.472 \pm 0.012)$ measure the deviation

$$\Delta\alpha = (\alpha_0 / \alpha_-) - 0.977 = -0.115 \pm 0.034$$

This is more than a $3\sigma$ deviation from the $\Delta I = 1/2$ rule.

Using the most recent lifetime measurements ($\tau_0 = 2.89 + 0.10 \times 10^{-10}$ s, $\tau_- = 1.623 \pm 0.018 \times 10^{-10}$ s) $\Delta\alpha$ and $\Delta\Gamma$ can be expressed in terms of the 3/2 and 1/2 contibutions to the s and p waves

$$\Delta\alpha = 1.37\ (s_{3/2}/s_{1/2} - p_{3/2}/p_{1/2})$$

and

$$\Delta\Gamma = -1.44\ (s_{3/2}/s_{1/2}) - 0.06\ (p_{3/2}/p_{1/2})$$

Solving these equations for the s and p ratios give

$$s_{3/2}/s_{1/2} = -0.038 \pm 0.011$$

and

$$p_{3/2}/p_{1/2} = +0.046 \pm 0.028$$

Amplitude ratios of this same order have long been demonstrated in the study of K decays.[31,32]

## 6.3 Baryon Magnetic Moments

Table 1.1 indicates fair agreement between baryon moments and the simple quark model predictions, provided one allows for symmetry breaking by the s-quark. A most obvious example can be seen from the measurement of the $\Lambda$ magnetic moment. By making the strange quark mass about 200 MeV heavier than the u and d quark masses, the $\Lambda$ moment can be precisely predicted. (Conversely, the precise measurement of the $\Lambda$ moment indicates that the strange quark is 200 MeV heavier than the u and d.)

However the discrepancies in the other predictions are not negligible. Attempts to fine tune magnetic moment models can be made by introducing the effects of configuration mixing, as well as symmetry breaking. In configuration mixing a certain percentage of the time the two quarks which

are normally in an S = 1, L = 0 state are in an S = 0, L = 1 state, with the full wave function appropriately adjusted to conserve angular momentum, parity and isospin. Other configurations are also possible.[33,34]

Further symmetry breaking effects include a mass difference between the u and d quarks, and making the quark mass a function of the baryon of which it is a constituent. Predictions for a number of these "refined" models are listed in Table 6.1.[35-42] It should also be noted that a fair agreement with experimental data is found in bag models of quark confinement.[43]

However, in all of this, it can be seen that, while some moment predictions move closer to their experimental values, others move away, and overall the improvement is small. Clearly, the physics of precisely predicting magnetic moments has not been found. However, this report can close on an interesting note.

If all symmetry breaking is ignored, all the quarks will have the same mass, namely 1/3 the mass of the baryon. Because the charges of the d and s quarks are the same, $\mu_d$ and $\mu_s$ will be equal. This leads to a number of interesting effects. For the $\Sigma^-$ and the $\Xi^-$ which contain only d and s quarks the baryon moment is just equal to the quark moment.

| | a | b | c | d | e | f | g | h | i |
|---|---|---|---|---|---|---|---|---|---|
| p | 2.79* | 2.79* | 2.79* | 2.79* | 2.79* | 2.85 | 2.79* | 2.79* | 2.64 |
| n | -1.91* | -1.91* | -1.86 | -1.91* | -1.91* | -1.85 | -1.91* | -1.91* | -1.76 |
| $\Lambda^0$ | -0.61* | -0.61* | -0.61* | -0.61* | -0.80 | -0.61 | -0.61* | -0.61* | -0.61 |
| $\Sigma^+$ | 2.67 | 2.14 | 2.16 | 2.39 | 2.20 | 2.54 | 2.74 | 2.68 | 2.53 |
| $\Sigma^0$ | 0.79 | 0.65 | 0.68 | | | 0.77 | | | 0.79 |
| $\Sigma^-$ | -1.09 | -0.83 | -0.78 | -0.95 | -0.69 | -1.00 | -1.21 | -1.37 | -0.96 |
| $\Xi^0$ | -1.43 | -1.13 | -1.13 | -1.27 | -1.37 | -1.20 | -1.46 | -1.24* | -1.39 |
| $\Xi^-$ | -0.49 | -0.46 | -0.59 | -0.48 | -0.63 | -0.43 | -0.52 | -0.58 | -0.53 |
| $\Sigma^0 \to \Lambda^0$ | -1.42 | -1.21 | | +1.45 | -1.35 | -1.51 | -1.68 | -1.96 | |

a. Ref. 15
b. Ref. 35
c. Ref. 41
d. Ref. 40
e. Ref. 38
f. Ref. 34
g. Ref. 37
h. Ref. 39
i. Ref. 43

Table 6.1 Theoretical predictions for baryon magnetic moments. (* indicates the experimental value was input)

That is

$$\mu_B = (g/2)(h/c)(q_B/m_B) = (h/c)(q_q/m_q)$$

$q_B/m_B = -1/m_B$ and $q_q/m_q = (-1/3)/(m_B/3)$, implies that if $g/2 = 1$ for quarks, then $g/2 = 1$ for the baryon. For the $\Xi^-$ this gives a magnetic moment (in nuclear magnetons) of -0.71, in agreement with the results reported here, and -0.78 for the $\Sigma^-$, also within one standard deviation of agreement with the new $\Sigma^-$ result. [16]

Also $\mu_d$ and $\mu_s$ will equal $-1/2\ \mu_u$ which then predicts that the ratio $\mu_\Xi / \mu_\Lambda$ will be 2. The experimental result is $2.014 \pm 0.028$.

## 6.4 Summary

In summary the following measurements have been made:

1. The magnetic moment of the $\Xi^-$ hyperon

$$\mu_{\Xi^-} = -0.716 \pm 0.040$$

2. The value of the product $\alpha_\Lambda \alpha_{\Xi^-}$

$$\alpha_\Lambda \alpha_{\Xi^-} = -0.303 \pm 0.004 \pm 0.004$$

3. The inclusive polarization of the $\Xi^-$ hyperon (at production angles of 5 and 7.5 mrad). The mean polarization of 192,110 events is $-0.093 \pm .007$, with an average $\Xi^-$ momentum of 180 GeV/c.

# Appendix A

## The Reconstruction Program

The first step in the gometrical reconstruction was fitting tracks in the y view, followed by fitting tracks in the x view upstream of the analyzing magnet. The x and y tracks belonging to a particular particle were identified by using the ambiguity planes in chambers 4 and 5.

All three particles were required to have the same bend center in the analyzing magnet (z coordinate). Downstream of the magnet the x coordinates were searched for tracks which intercepted the upstream tracks at the bend center. Each point used in the track fitting was given the same weight ($\sigma^2$ = 1/300) which was determined from the resolution of the MWPC's.

Using the slopes and intercepts, preliminary verticies for both the $\Xi^-$ and the $\Lambda$ were calculated. With the constraint that the verticies in the x-z and y-z planes must occur at the same z coordinate, a $\chi^2$ function was minimized with respect to the slopes and intercepts. The final

geometric $\chi^2$ for the event was then calculated using the fitted values of the slopes and intercepts and the x and y coordinates of the wire hits.

Following the geometric fit, a kinematic fit was performed to see if the tracks chosen as the proton and $\pi^-$ from the $\Lambda$ decay were consistant with the two particles being the decay products of a $\Lambda$.[44] This was a particularly useful procedure since it was possible for reconstruction program to assign the wrong $\pi^-$ to the decay. The measured parameters used in the fit were the slopes of the proton and $\pi^-$ upstream of the analyzing magnet, their bend angles in the magnet, and the direction and momentum of the $\Lambda$. The parameters of the decay which are fit, are the decay angles $\theta$ and $\phi$ in the $\Lambda$ rest system and the momentum of the $\Lambda$ in the laboratory. The constraints which are used are the kinematic relations for the energy and center of mass momentum consistant with the decay $\Lambda \rightarrow p\ \pi^-$. Using the constraint equations the parameters to be fit can be related to the measured quantities. Since there are five parameters and six measured inputs a $\chi^2$ can be formed to measure the difference between the input quantities and those determined by the kinematics. For example

$$\chi^2 = \frac{(sx-sx^0)^2}{\sigma_x^2} + \frac{(sy-sy^0)^2}{\sigma_y^2} + \frac{(\alpha p-\alpha p^0)^2}{\sigma_\alpha^2} + \ldots.$$

where sx and sy are slopes of the proton in the x and y views, $\alpha p$ is the bend angle of the proton in the analyzing magnet, and $sx^0$, $sy^0$ and $\alpha p^0$ are the slopes determined from the kinematical relations. The $\sigma$'s are the errors in the measured quantities determined by the geometrical fitting procedure. Cross terms in the have been neglected, though they should appear because the errors in the various quantities are not independent. The further approximation that

$$\sigma_x^2 = \sigma_y^2 = \sigma^2 = (\sigma_x^2 + \sigma_y^2)/2$$

was also made. The above approximations are not justified in a mathmatical sense. In particular there is a large difference in the accuracy of the measurement of the upstream tracks in the horizontal and vertical views, since the vertical tracks are determined using all of the chambers, rather than just those upstream.

However, these approximations make the calculation and minimization of the $\chi^2$ much simpler, and the original question of whether the event is constiant with the $\Lambda \rightarrow p\ \pi^-$ hypothesis is not affected by these approximations.

In the present experiment, the $\chi^2$ distribution has a larger percentage of events with a $\chi^2$ greater than 10 than would be expected from a classical one constraint $\chi^2$ distribution. However, the same behavior was observed in the

Monte Carlo. The $\chi^2$cut on the real events was made based on studies of the Monte Carlo events where the accuracy of the reconstruction program and the fit could be tested.

# Appendix B

## The Hybrid Monte Carlo Program

### B.1 The Acceptance Function

There are two major factors which contribute to the "acceptance function". The first and most obvious is the experimental apparatus which has physical boundaries and trigger requirements which limit the laboratory acceptance and hence the cos θ acceptance in the center of mass. In addition to this, the reconstruction program, which has difficulty in reconstructing events with narrow opening angles in the laboratory, also has an acceptance function which affects the asymmetry determination.

The limiting apertures and trigger boundaries are easily included in the software model of the apparatus. If these are input correctly, when the real events are tested for acceptance (a first step in the HMC analysis) none should fail. In practice, two things occur. 1) A few real events fail due to measurement errors in the reconstruction which

cause the event to be projected outside the boundaries, however the number of these events should be small. 2) The software appertures are usually made slightly more restrictive than the real boundaries, so a small percentage of real events are lost because of this.

Including the effects of the reconstruction program is a more complicated problem. The majority of events which do not reconstruct have narrow opening angles in either one or both of the decays. The loss of these events manifests itself in the polarization analysis as a depletion of events in certain regions of cos $\theta$. In particular, for the proton distribution in the $\Lambda$ rest frame the depletion occurs in the center of the cos $\theta_x$ and cos $\theta_y$ distributions, and on the edges of the cos $\theta_z$ distribution (cos $\theta_z = \pm 1$).

Since the HMC events are generated flat in cos $\theta$, and not affected by narrow laboratory angles, they will not agree with the distribution of the real events in these "problem" regions of cos $\theta$. By testing the HMC events for a minimum separation between the laboratory vectors, in principle, the disagreement can be resolved. The problem arises in choosing the minimum distance. If the distance is too small the test is inefficient, and if it is too large, though making the distributions agree, a large number of real events, which were reconstructed, fail the cut. Since the cut is designed

to compensate for depletions in the end bins in cos $\theta$, too severe a cut eliminates more of these events. This is particularly disadvantageous since the largest sensitivity to the real asymmetry in the data comes from the events having cos $\theta$ values nearest to $\pm 1$.

In this experiment, the asymmetry of the proton distribution in the $\Lambda$ rest frame was analyzed. (See Sec. 4.2.) Hence it was the $\Lambda$ acceptance which was tested. This was a nice feature of the analysis since the geometrical acceptance for $\Lambda$'s was better than for $\Xi$'s. However, the reconstruction acceptance for $\Lambda$'s was coupled to the acceptance for the entire event. For example, for a fixed separation between the proton and the pion (from the $\Lambda \rightarrow p\,\pi^-$ decay), the reconstruction program may or may not be successful in reconstructing the event, depending on the position of the pion from the $\Xi^- \rightarrow \Lambda\,\pi^-$ decay.

In this analysis, the separation cut on the $\Lambda$'s required the sum of the proton-pion separation in chambers 4 and 5, including both x and y views, to be greater than 24 mm. In addition, the sum of the separations in the y view, in chambers 5 and 6, were required to be greater than 10 mm for the proton and $\pi^-$ from the $\Lambda$ decay, and 8 mm for the separation between the two $\pi^-$'s.

Unlike the geometrical limiting apertures, which could have effects on the acceptance which depended on production angle, the failures of the reconstruction program were independent of production angle. Hence, they produce biases which subtract from the polarization signal. The separation cuts which were used were ones which minimized the biases without sacrificing sensitivity to the polarization.

If a HMC event failed to be accepted it was disgarded and a new value of cos $\theta$ was chosen. This procedure was repeated until ten Monte Carlo events had been accepted or until 200 attempts had been made. If ten events had not been accepted after 200 tries the real event was eliminated from the analysis. This occured for less than 0.1% of the events analyzed. For each event this entire procedure was repeated for each of the coordinates.

In order to determine whether the HMC events were indeed modeling the real event distributions at the spectrometer apertures, distributions of the Monte Carlo events at geometric apertures and for track separations were compared with the corresponding distributions for the real events, and a $\chi^2$ computed for each comparison. The distribution of $\chi^2/df$ for these comparisons is plotted in Fig. B1.

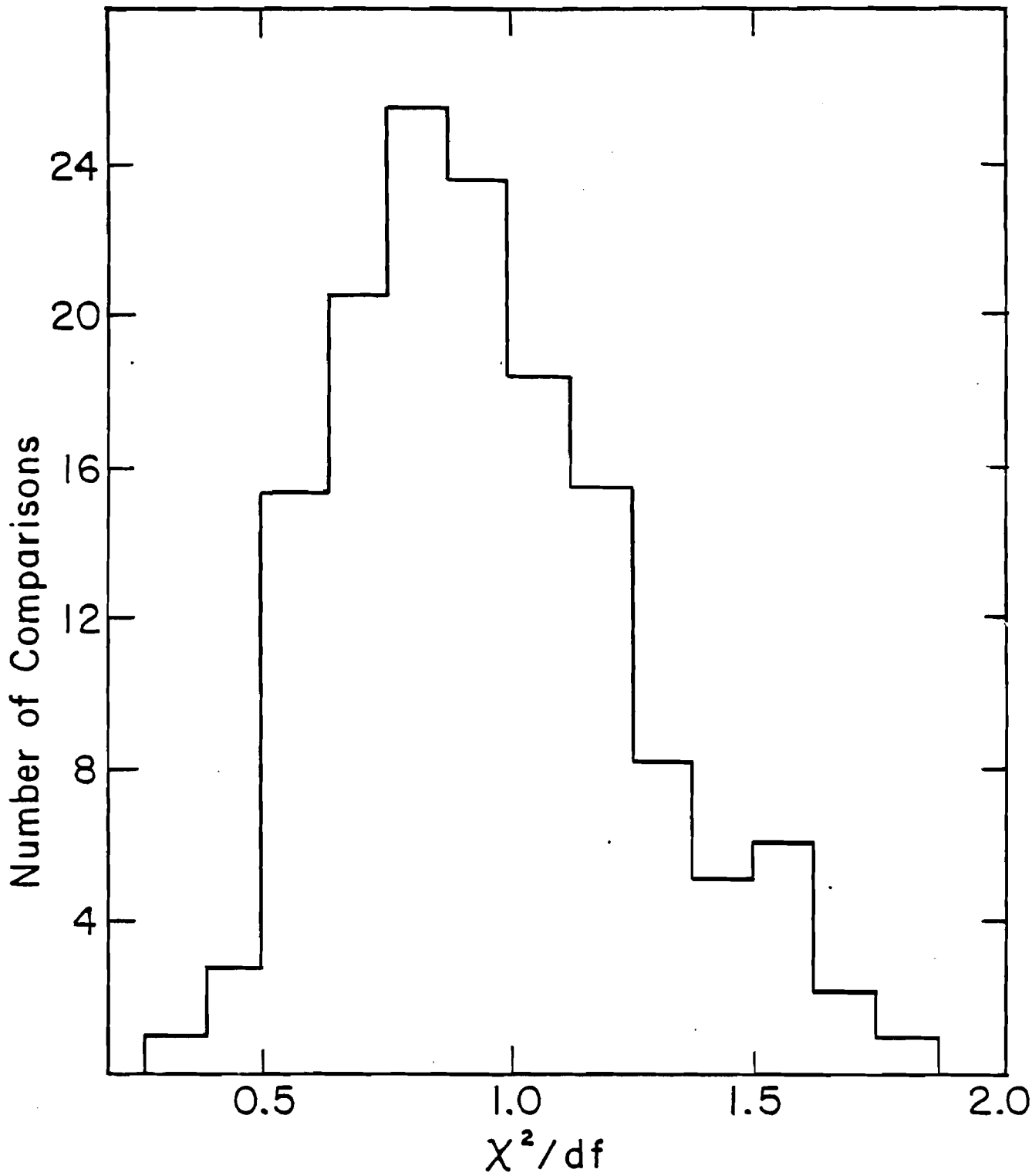


Figure B.1 Distribution of $\chi$'s for comparisons of real and Hybrid Monte Carlo Distributions at spectrometer apertures and for track separations.

## B.2 The $\chi^2$ Function

A complication in the comparison of the real and HMC events arises since the real events, from which the "isotropic" Monte Carlo events were generated, have an asymmetry due to both the apparatus acceptance and the real polarization. To correct the Monte Carlo distribution for the real polarization, the cos θ for each Monte Carlo event (j) must be weighted by

$$W_{ij} = 1 / (1 + A \cos \theta_i)$$

where $\theta_i$ refers to the real event in cos θ bin (i) from which the HMC event was generated. (Twenty bins were used.)

If the asymmetry of the real events were known, the cos θ distrbutions of the real and HMC events could be made to agree by making the weight

$$W_{ij} = (1 + A \cos \theta_{ij}) / (1 + A \cos \theta_i)$$

In practice, the asymmetry is found by expanding this weight as a power series in A and calculating the coefficients of the asymmetry for each HMC event. The weight can be expanded

$$W = 1 + \sum_I (-A)^I \cos^{I-1}\theta (\cos \theta_i - \cos \theta_{ij})$$

(Only the first four terms in the expansion were kept.)

A $\chi^2$ technique was then used to choose a value for the asymmetry in the real events. A $\chi^2$ was constructed

$$\chi^2 = \sum_J (N_R(J) - N_{MC}(J,A))^2 / N_R(J)$$

where J was the bin in cos θ , A was the asymmetry to be measured, $N_R(J)$ was the number of real events and $N_{MC}(J)$ was the sum of the weights, $W_{ij}$. $N_{MC}$ was renormalized to satisfy

$$\sum_J N_{MC}(J) = \sum_J N_R(J)$$

$\chi^2$ and the first and second derivatives with respect to A were calculated and $\chi^2$ was minimized using Newton's method to obtain A.[45]

# Appendix C

## Polarization Results for Sets 1 & 2

The two data sets presented here were not taken with the final version of the $\Xi^-$ trigger. They were taken in the beginning of the experiment before the final running conditions had been determined. The data was taken at a 5 mrad production angle and a 6.6 T-m field. The two sets have significantly less data than Set 3 which was taken at the same production angle and field integral but with the final version of the trigger. The two sets give results consistent with the rest of the data and are included in the final result.

| P Bin | P | Px | Pz |
|---|---|---|---|
| 140-160 | 153 | +0.0397±0.0797 | +0.0331±0.0698 |
| 160-180 | 171 | -0.1032±0.0393 | -0.0090±0.0344 |
| 180-200 | 190 | -0.0253±0.0291 | -0.0131±0.0283 |
| 200-220 | 209 | -0.0384±0.0314 | -0.0046±0.0329 |
| 220-240 | 229 | -0.1172±0.0426 | +0.0235±0.0150 |
| 240-290 | 255 | -0.0886±0.0499 | +0.1129±0.0580 |

Polarization for Data Set 1

| | | | |
|---|---|---|---|
| 125-140 | 134 | -0.0470±0.0869 | +0.0178±0.0988 |
| 140-160 | 152 | -0.0664±0.0304 | +0.0142±0.0343 |
| 160-180 | 170 | -0.0501±0.0217 | -0.0299±0.0234 |
| 180-200 | 190 | -0.0575±0.0219 | -0.0320±0.0240 |
| 200-220 | 209 | -0.0617±0.0271 | -0.0013±0.0292 |
| 220-240 | 229 | -0.0717±0.0385 | -0.0348±0.0406 |
| 240-290 | 255 | -0.1096±0.0486 | -0.0030±0.0533 |

Polarization for Data Set 2

Table C.1 Polarization results vs. momentum for Data Sets 1 & 2

| P Bin | P | Bx | Bz |
|---|---|---|---|
| 140-160 | 153 | +0.0113±0.0797 | +0.0224±0.0698 |
| 160-180 | 171 | -0.0311±0.0393 | +0.0173±0.0344 |
| 180-200 | 190 | -0.0119±0.0291 | -0.0352±0.0283 |
| 200-220 | 209 | +0.0693±0.0314 | +0.0937±0.0329 |
| 220-240 | 229 | -0.0479±0.0426 | +0.0955±0.0448 |
| 240-290 | 255 | +0.0616±0.0499 | +0.1060±0.0580 |

Biases for Data Set 1

| | | | |
|---|---|---|---|
| 125-140 | 134 | +0.1640±0.0869 | -0.0840±0.0988 |
| 140-160 | 152 | +0.0567±0.0304 | -0.0695±0.0343 |
| 160-180 | 170 | +0.0057±0.0217 | +0.0239±0.0234 |
| 180-200 | 190 | +0.0152±0.0219 | +0.0588±0.0240 |
| 200-220 | 209 | +0.0110±0.0271 | +0.0691±0.0292 |
| 220-240 | 229 | +0.0125±0.0385 | +0.0662±0.0406 |
| 240-290 | 255 | -0.0587±0.0486 | +0.0707±0.0533 |

Biases for Data Set 2

Table C.2 x and z biases as functions of momentum for Data Sets 1 & 2

| P Bin | P | "Py" | By |
|---|---|---|---|
| 140-160 | 153 | -0.0439±0.0570 | +0.0146±0.0570 |
| 160-180 | 171 | -0.0493±0.0299 | +0.0191±0.0299 |
| 180-200 | 190 | +0.0410±0.0249 | -0.0198±0.0249 |
| 200-220 | 209 | +0.0295±0.0287 | -0.0471±0.0287 |
| 220-240 | 229 | -0.0521±0.0389 | -0.0040±0.0389 |
| 240-290 | 255 | -0.0405±0.0462 | -0.0227±0.0462 |

Y asymmetries for Data Set 1

| | | | |
|---|---|---|---|
| 125-140 | 134 | +0.0178±0.0742 | -0.0615±0.0742 |
| 140-160 | 152 | +0.0132±0.0301 | -0.0245±0.0301 |
| 160-180 | 170 | +0.0050±0.0210 | +0.0042±0.0210 |
| 180-200 | 190 | +0.0433±0.0210 | -0.0290±0.0210 |
| 200-220 | 209 | -0.0328±0.0250 | -0.0604±0.0328 |
| 220-240 | 229 | -0.0115±0.0348 | -0.0299±0.0348 |
| 240-290 | 255 | -0.0283±0.0433 | -0.0282±0.0433 |

Y asymmetries for Data Set 2

Table C.3 Parity violating y polarizations and biases as functions of momentum for Data Sets 1 & 2

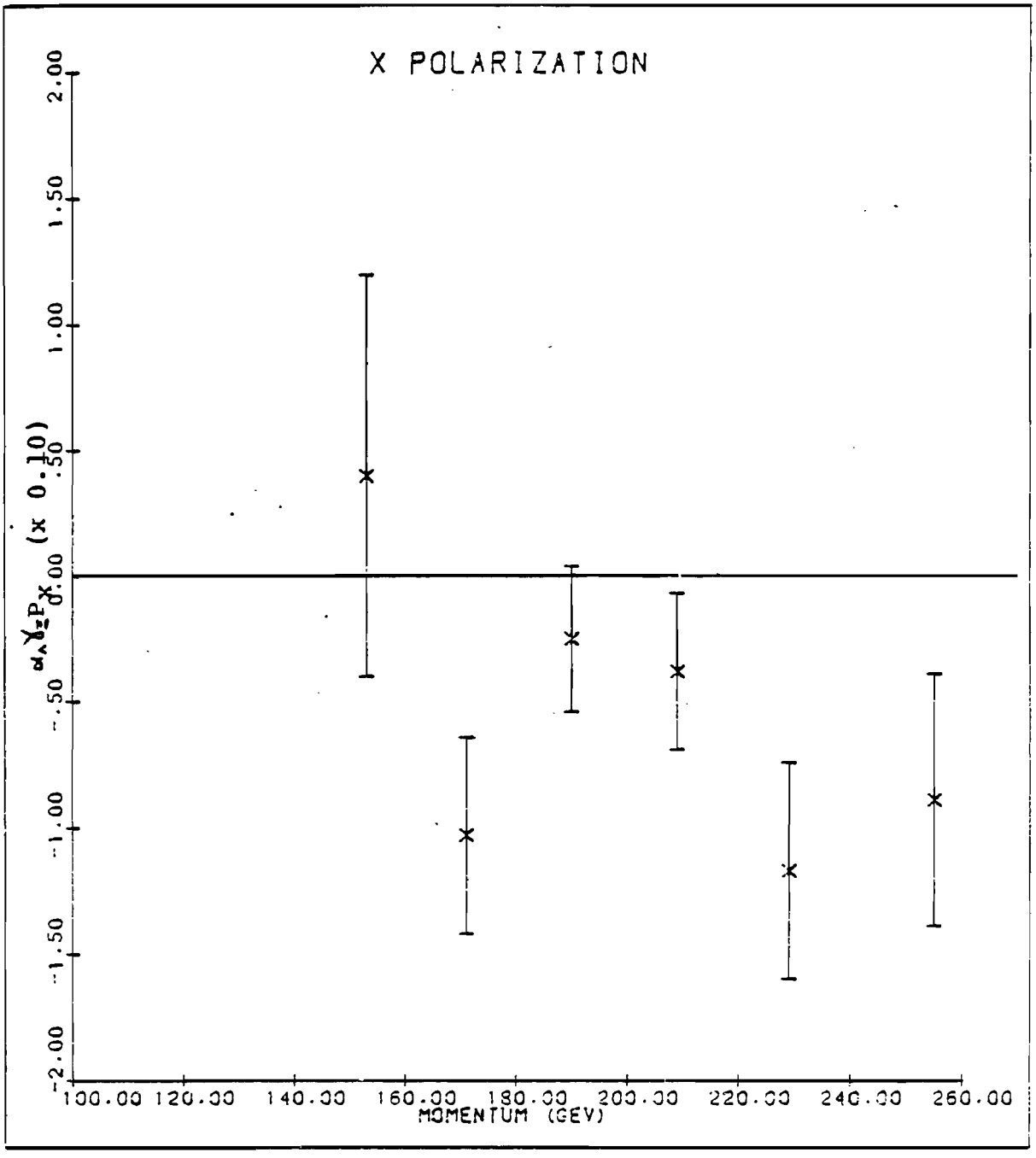


Figure C.1 $\alpha_\Lambda \gamma_\Sigma P_x$ vs. momentum
Data Set 1

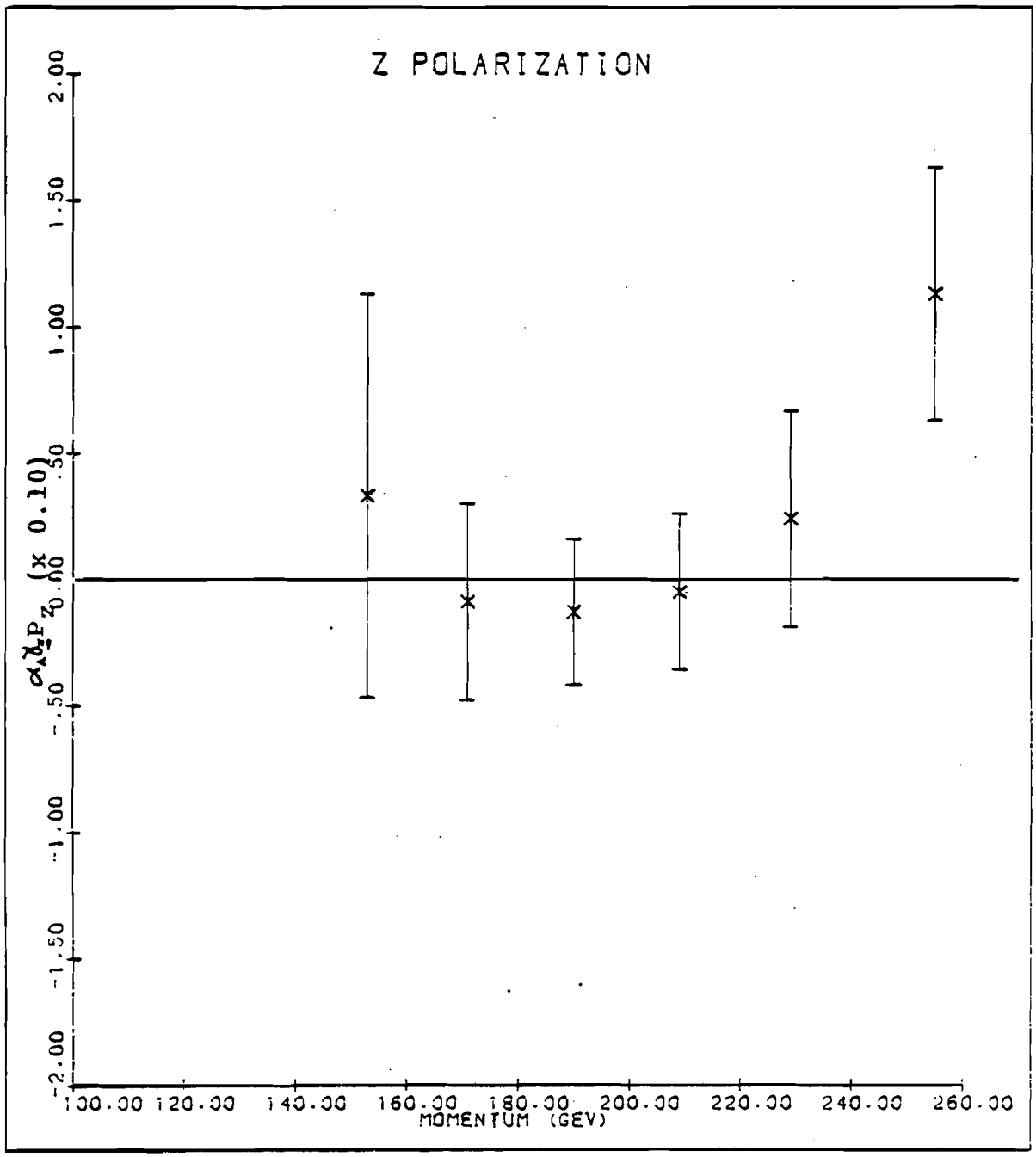


Figure C.2 $\alpha_A \gamma_\pm P_Z$ vs. momentum
Data Set 1

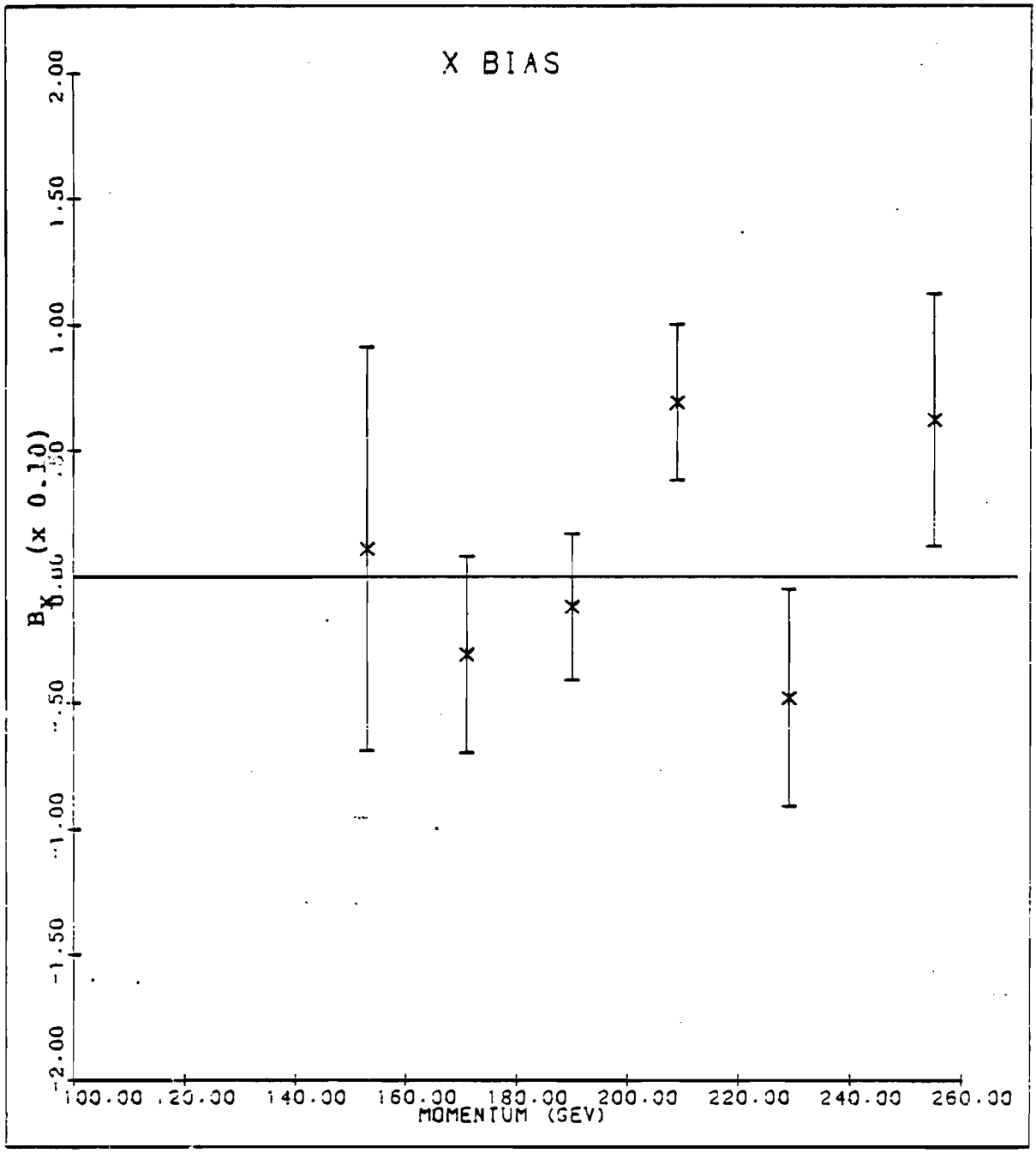


Figure C.3 x bias vs. momentum
Data Set 1

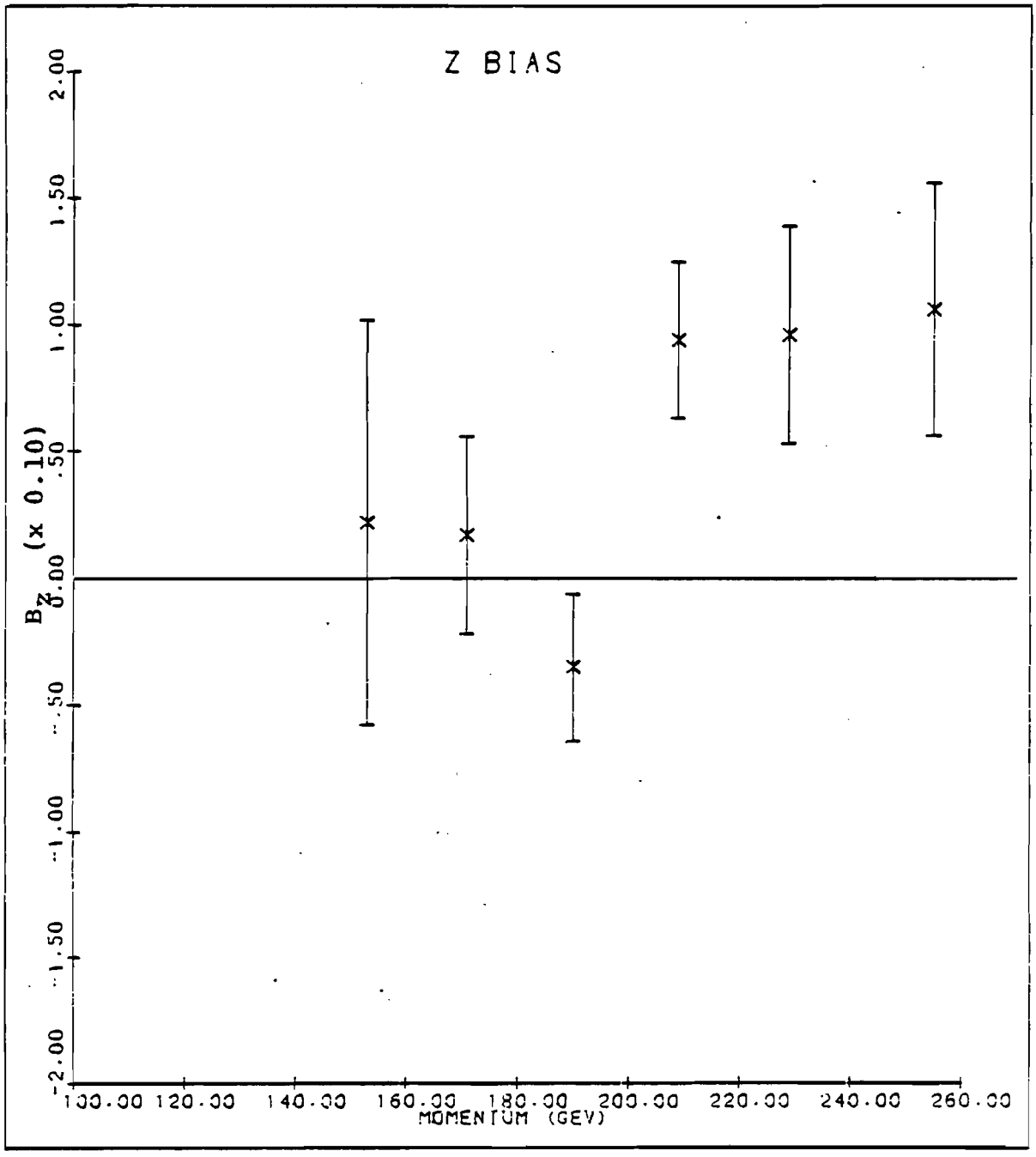


Figure C.4 z bias vs. momentum
Data Set 1

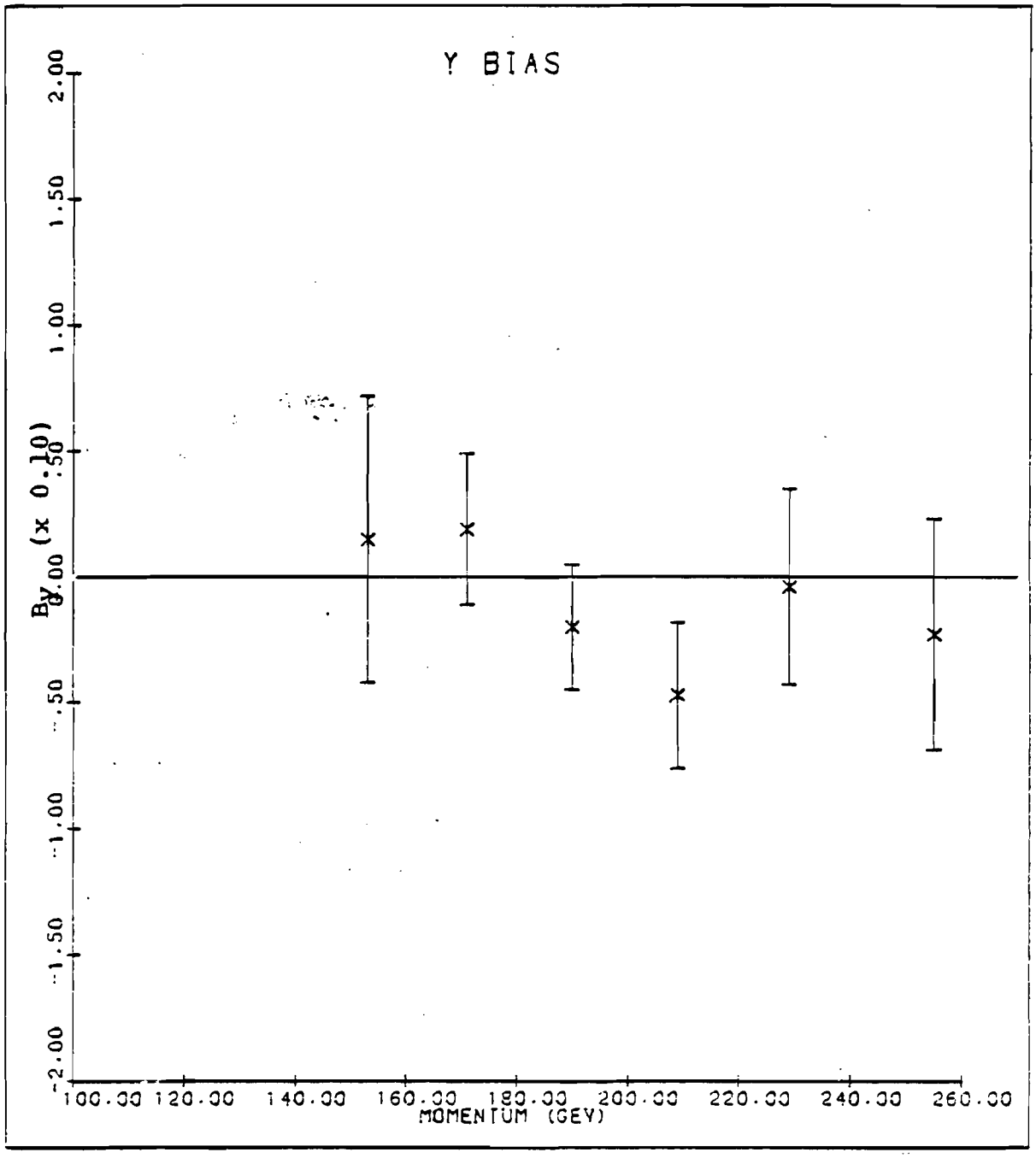


Figure C.5 y bias vs. momentum
Data Set 1

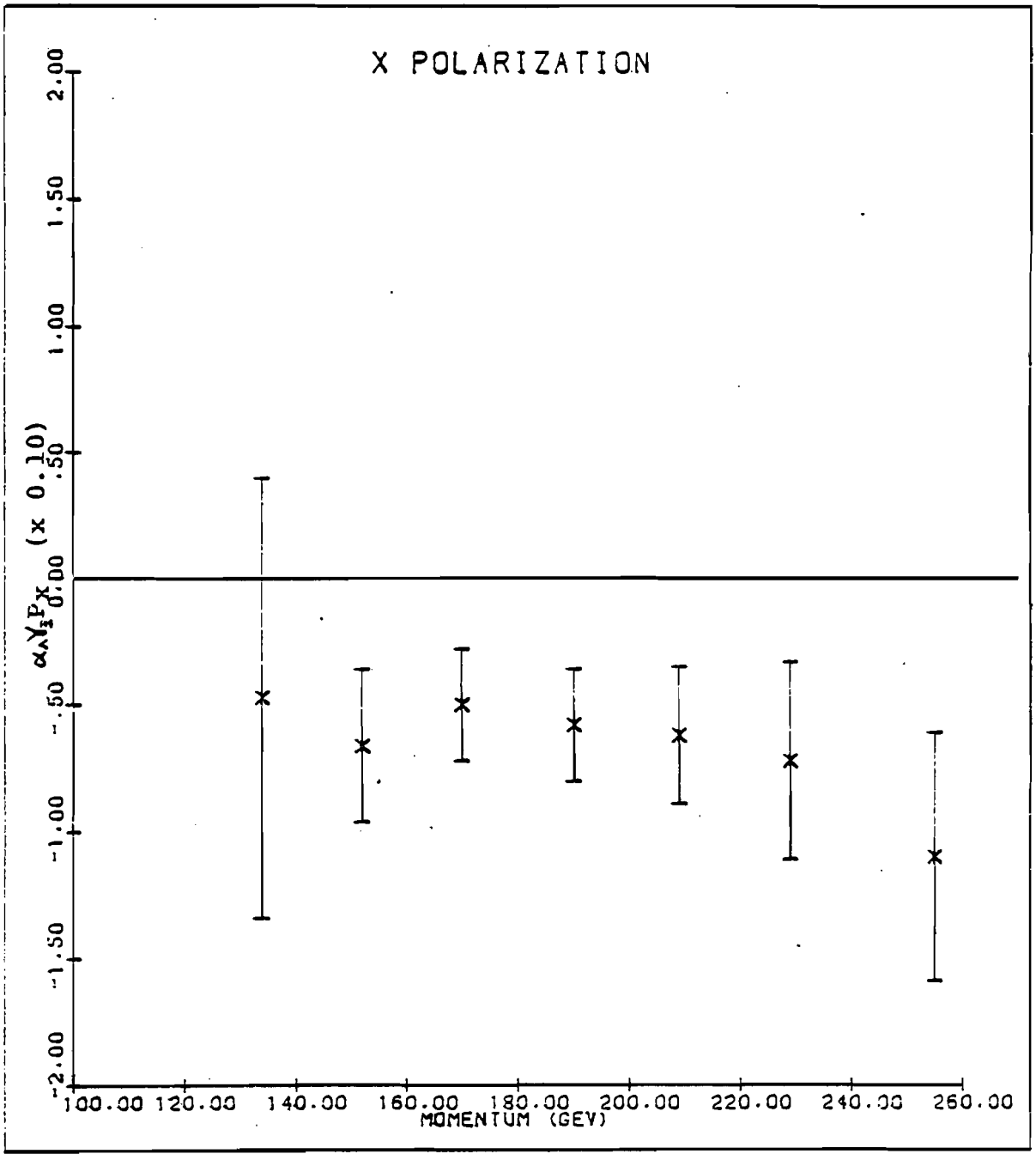


Figure C.6 $\alpha_\Lambda \gamma_\Xi P_x$ vs. momentum
Data Set 2

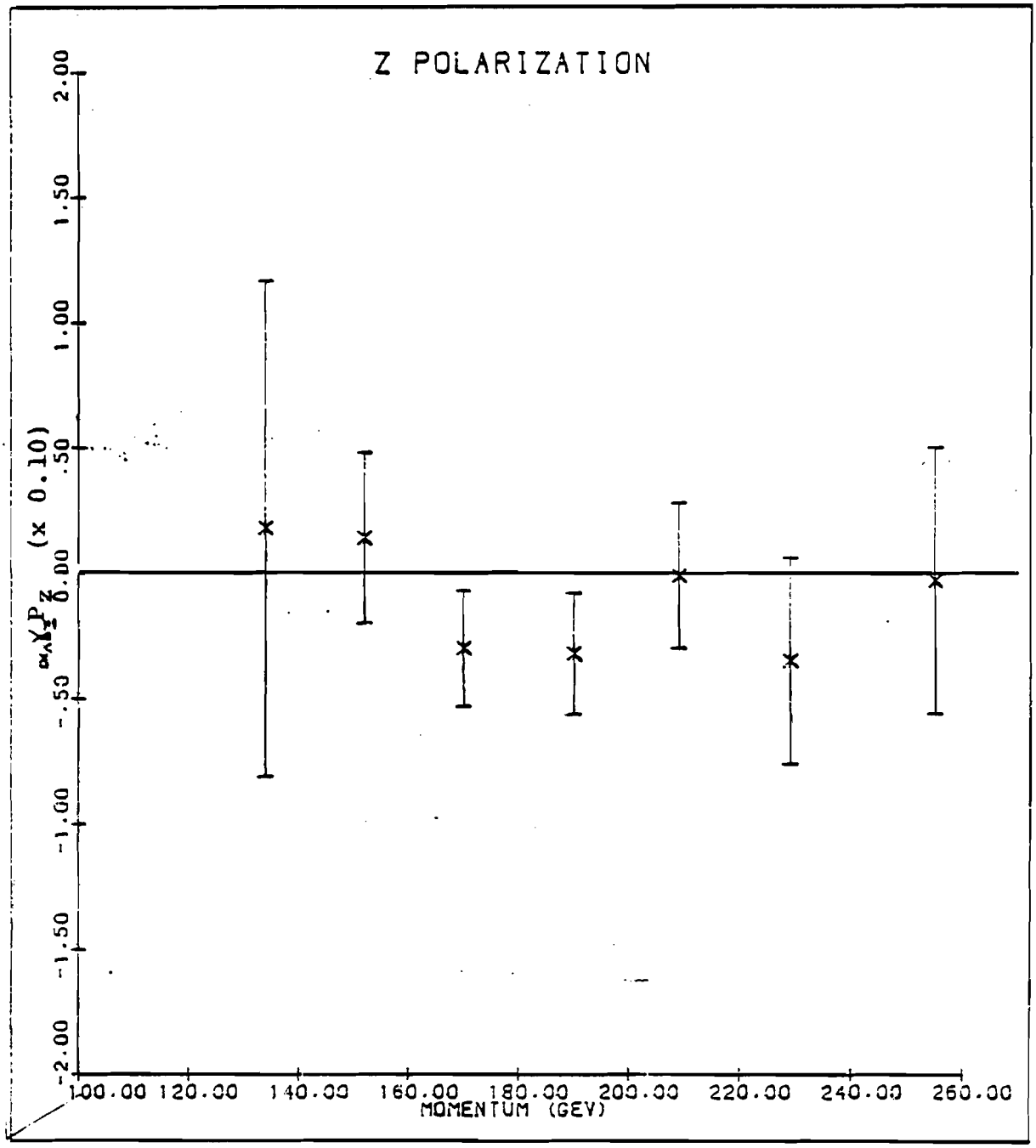


Figure C.7 $\alpha_\Lambda \gamma_\Xi P_z$ vs. momentum
Data Set 2

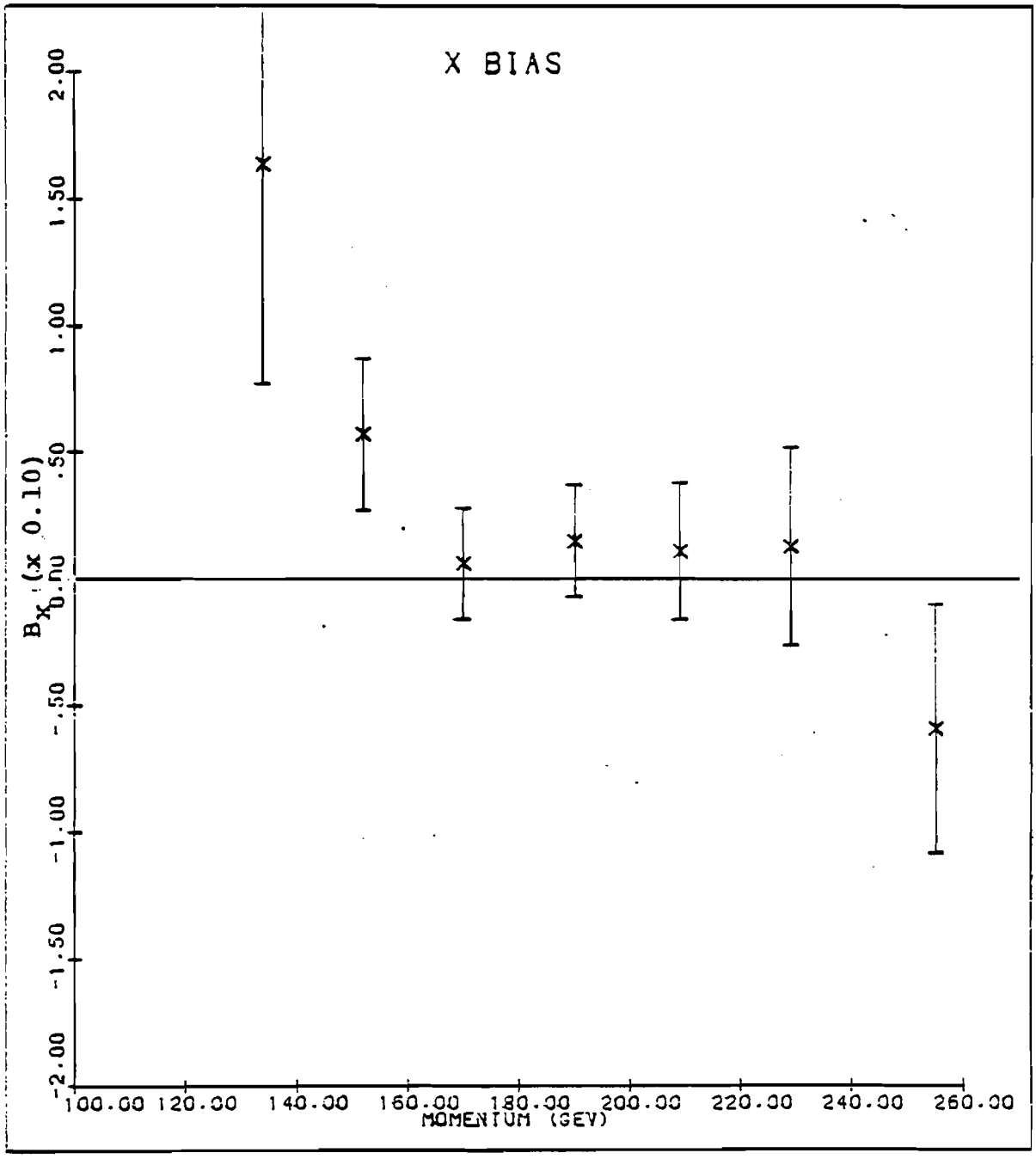


Figure C.8 x bias vs. momentum
Data Set 2

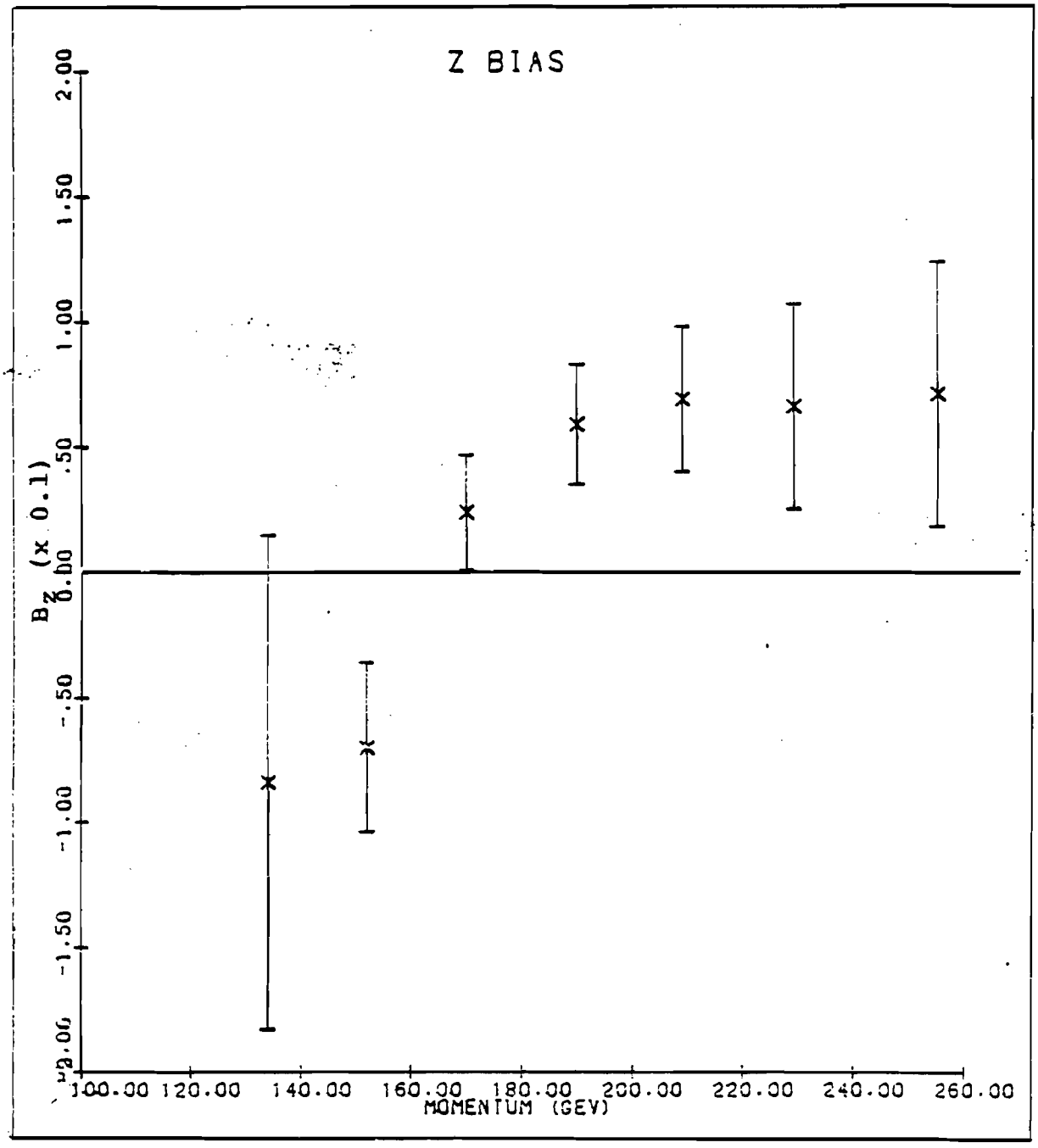


Figure C.9 z bias vs. momentum
Data Set 2

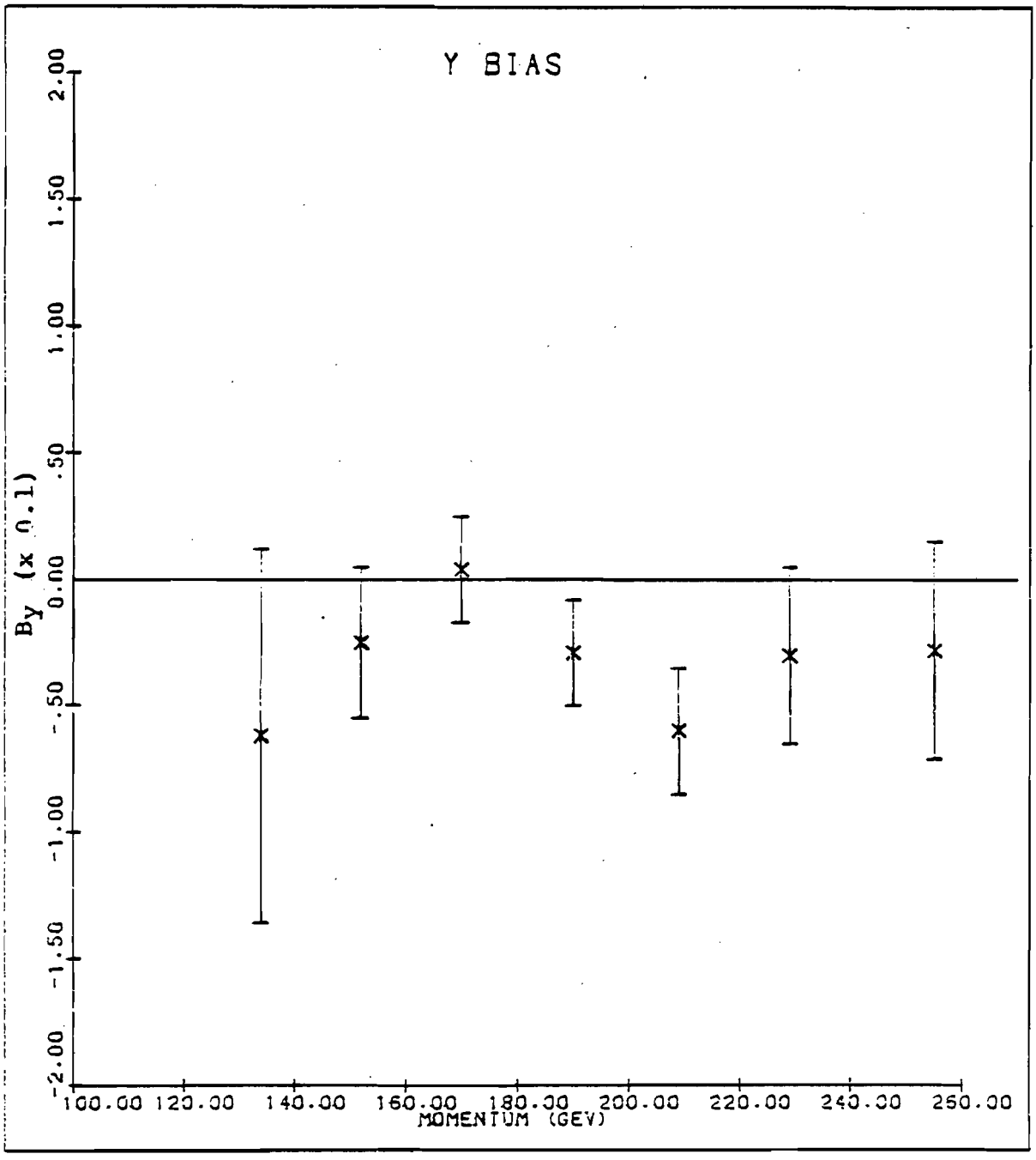


Figure C.10 y bias vs. momentum
Data Set 2

# REFRERENCES


1. G. Bunce, et.al., Phys. Rev. Lett. 36, 1113 (1976)

2. L. Schachinger, et.al., Phys. Rev. Lett. 41, 1348 (1978)

3. K. Heller, et.al., Phys. Lett. 68B, 480 (1977)

4. R. Grobel, PhD thesis, University of Wisconsin (1980) (unpublished)

5. K. Raychaudhuri, et.al., Phys. Lett. 90B, 319 (1980)

6. B. Anderson, et.al., University of Lund, LUTP 79-7 (1979)

7. K. Heller, et.al., Phys. Rev. Lett. 41, 607 (1978); Erratum: Phys. Rev. Lett. 45, 1043 (1980)

8. T. DeGrand and H. Miettinen, Phys. Rev. D 24, 2419 (1981)

9. P. T. Cox, PhD thesis, University of Michigan, UMHE-80-19 (1980) (unpublished)

10. P. T. Cox, et.al., Phys. Rev. Lett. 46, 877 (1981)

11. Particle Data Group, Rev. Mod. Phys. 51, 5283 (1980)

12. G. McD. Bingham, et.al., Phys. Rev. D1, 3010 (1970)

13. R. L. Cool, et.al., Phys. Rev. D10, 792 (1974)

14. S. Coleman and S. L. Glashow, Phys. Rev. Lett. 6, 423 (1961)

15. A. DeRujula, et.al., Phys. Rev. D12, 147 (1975)

16. L. Deck, PhD thesis, Rutgers University (1981) (unpublished)

17. H. J. Lipkin, Phys. Rev. Lett. 41, 1629 (1978)

18. A detailed derivation of the Thomas precession is given by J. D. Jackson, "Classical Electrodynamics", pp. 541-547, 2nd edition John Wiley & Sons Inc., (1975)

19. See, for example, H. Goldstein, "Classical Mechanics", pp. 132-134, Addison-Wesley Publishing Co., Inc. (1950)

20. For a more rigorous derivation see V. Bargmen, et.al., Phys. Rev. Lett. 2, 435 (1959), or R. Hagerdorn, "Relativistic Kinematics", pp. 126-137, W. A. Benjamin, Inc. (1973)

21. L. Schachinger, PhD thesis, Rutgers University (1978) (unpublished)

22. P. Martin, PhD thesis, University of Wisconsin (1978) (unpublished)

23. K. B. Luk, private communication.

24. G. Bunce, Nucl. Inst. Meth. 172, 553 (1980)

25. S. F. Biagi, et.al.,EPS Conf. on High Energy Phys., Lisbon, Portugal (1981)

26. T. Devlin, private communication. This result has also been predicted by more specific arguments, i.e. Reference 8.

27. C. Wilkinson, et.al., Phys. Rev. Lett. 46, 803 (1981)

28. O. E. Overseth and S. Pakvasa, Phys. Rev. Vol. 184, No. 5 (1969)

29. J. Finjord and M. K. Gaillard, Phys. Rev. D22, 778 (1980)

30. R. Handler, et. al., to be published, Phys. Rev. D (1982)

31. T. Devlin and G. Barshay, Phys. Rev. Lett. 19, 881 (1967)

32. T. Devlin and J. Dickey, Rev. Mod. Phys. 51, 237 (1979)

33. D. Geffen and W. Wilson, Phys. Rev. Lett. 44, 370 (1980)

34. N. Isgur and G. Karl, Phys. Rev. D21, 3175 (1981)

35. Y. Tomozawa, Phys. Rev. D19, 1626 (1979)

36. J. Franklin, Phys. Rev. Lett. 45, 1607 (1980)

37. M. Bohm, et. al., paper no. 819, XX International Conference on High Energy Physics, Madison, Wisconsin (1980)

38. S. Oneda, et. al., paper no. 772, XX International Conference on High Energy Physics, Madison, Wisconsin (1980)

39. A fairly complete review of the present status of theoretical models for predicting magnetic moments is given by J. L. Rosner, XX International Conference, AIP Conference Proceedings, No. 68, pp. 540-545, (1980). References 37 and 38 have been taken from this source.

40. R. B. Teese and R. Settles, Phys. Lett. 87B, 111 (1979)

41. H. J. Lipkin, Phys. Lett. 89B, 358 (1980)

42. R. B. Teese, Phys. Rev. D24, 1413 (1981)

43. T. Barnes, Nucl. Phys. B96, 353 (1975)

44. The description of the kinematic fit is based on an internal memo by R. Handler.

45. A fairly extensive description of the Hybrid Monte Carlo is given in Reference 9.

# CURRICULUM VITAE

Regina Abby Rameika

| | |
|---|---|
| 1954 | Born July 29 in Red Bank, New Jersey. |
| 1972 | Graduated from Ewing High School, Trenton, New Jersey. |
| 1972-1976 | Physics major, Rutgers University, New Brunswick, New Jersey. |
| 1974-1976 | Worked on an R & D project for controlled fusion. |
| 1975 | Senior Honors Project--"A Survey Report on Controlled Nuclear Fusion." |
| 1976 | B.A., Rutgers College. |
| 1976-1981 | Teaching Assistant for undergraduate Physics recitations and advanced laboratories. |
| 1978-1981 | Graduate Assistant in High Energy Experimental Physics. Worked with the Neutral Hyperon group at Fermi National Lab, Batavia, Illinois. Active participation in E495, E361, and, E620. |
| 1979 | Worked on conversion of the Neutral Hyperon beam at FNAL to a charged hyperon beam designed to detect and measure polarizations and magnetic moments for the $\Sigma^+$, $\Sigma^-$, and $\Xi^-$. |
| 1980-1981 | Thesis Experiment--Completed data taking and analysis of the $\Xi^-$ polarization, alpha parameter and magnetic moment. |
| | "Polarization of $\Sigma^+$ Hyperons Produced by 400 GeV Protons", Physical Review Letters, Vol.46, No.13, March 1981. |
| | "Precise Measurement of the $\Xi^0$ Magnetic Moment", Physical Review Letters, Vol.46, No.14, April 1981. |